M ELiSS A

Technical Note

Memorandum of Understanding 19071/05/NL/CP

MELiSSA Food Characterization: phase1

Technical Note: 98.3.22

Review of modelling issues related to the plant production unit, identification of critical point and proposed method

prepared by/préparé par	Matteo Nobili and Lorenzo Bucchieri
reference/réference	Contract number 22070/08/NL/JC
issue/édition	1
revision/révision	1
date of issue/date d'édition	30.04.2010
status/état	Final
Document type/type dedocument	Technical Note
Distribution/distribution	

CONFIDENTIAL DOCUMENT

A P P R O V A L

Title *titre*	Chamber hardware modeling	*issue* *issue* 1	*revision* *revision* 1

author *auteur*	Matteo Nobili	*date* *date*

Reviewed by *(UGent)*	Martin Weihreter	*date* *date* 19.04.2010
approved by *(UGent)*	Dominique Van Der Straeten	20.04.2010
approuvé by		

C H A N G E L O G

reason for change /raison du changement	*issue/issue*	*revision/revision*	*date/date*

C H A N G E R E C O R D

Issue: 1 Revision: 1

reason for change/raison du changement	*page(s)/page(s)*	*paragraph(s)/paragraph(s)*

TABLE OF CONTENTS

(List **OF** Tables)

Table OF Figures

Extended summary

The global final objective of the Melissa food characterization project is to provide nutritionally balanced and palatable menus partially based on on-board cultivated plant foods. With this aim the chamber hardware, which is the plant growing environment, is a key factor in order to guarantee satisfactory conditions for food production. Typically, plant growth chambers used for plant physiology research suffer from a degree of environmental parameter heterogeneity which could affect the yield in quality and quantity. Indeed, depending on light intensity, temperature or air mixing rate, individual crops will display different growth rates and composition at a given sampling time.

The modeling of the chamber hardware has the potential to give an insight into the phenomena leading to non-homogenous growing condition and to provide suggestions on how to mitigate it. The aim of the task which Enginsoft is in charge of (WP 3220) is to define the needs and the approach to build the numerical model.

Within this task, the following steps were identified:

Step 1

- Dry model characterization

Step 2

- Set up and test of the Basic Wet Model
- Development of the Advanced Canopy Sub Model

The first step is intended to reproduce the performance of the chamber without plants in order to check the efficiency of the system from a fluid dynamic point of view. With this aim, the maps of the environmental factors are used to detect problematic regions of the flow which are likely to generate stress for the plants once the plants are put in place. The effect of design changes on the environmental factors are also highlighted.

Next, within step 2, the plant evaporative load is added into the chamber model.

A straight approach is followed at first. The basic wet model integrates evapotranspiration, carbon dioxide assimilation and oxygen production by the use of empirically fitted figures derived from an experimental data scenario supplied by U_Cesame and approved by U_Gent and ESA. So the flow rate data acquired during the experimental campaign is directly imposed as boundary condition to the CFD simulation.

Further with the Canopy Sub model, plant modeling is moved to a more complex stage. The interaction of plants with the environment is established. A mathematical law based on biochemical reactions (output to be verified with WP3210 UCL-CESAME) guarantees the link between mass balances and environmental factors such as radiation intensity and gas concentrations. Analysis are conducted on a reduced local model for different environmental conditions.

Moving from the proof of concept model (either with or without plants), realistic models can be parameterized depending on the choice of the proposed hardware. The experience gathered in the WP3220 will provide an important foundation of knowledge in order to define the requirements for model development in the food characterization unit (WP 7000).

1. Dry model (Step1)

The present part of the document provides a detailed description of the approach and the assumption made for the construction of the HPC dry model. The dry model, as mentioned in the extended summary, represents the first step in the modeling of chamber hardware.

The workflow in the dry model definition is the following:

- Assessment of the HPC data provided by ESA (HPC1 data package)
- Construction of the 3D geometry of the chamber by means of its technical drawings and of the measurements made on the prototype.
- Generation of the computational grid.
- Set up of the physics of the problem

The results of the numerical simulations allowed the assessment of the air flow distributions inside the chamber and to generate maps of environmental factors such as velocity, temperature and light. Accordingly it was possible to characterize the heterogeneity of the environmental factors that induces undesirable non-homogenous plant growth and composition.

1.1. Acquired data

The geometrical model, the HPC physical properties and the boundary conditions for the fluid-dynamic analysis were derived from the data supplied by ESA.

Document	Date	Origin	Type of data
DVD	30/01/2009	UGent, Ghent UoGuelph, Guelph	Technical drawings (.pdf) Parts specifications (.pdf .xls) Technical notes (.pdf) Chamber images (.jpeg)
CD	09/03/2009	Sherpa, Paris	Papers (.pdf) Chamber images (.jpeg)
jpeg /pdf	02/04/2009	UAB, Barcelona UoGuelph, Guelph	Measurements made on the chamber Chamber Images (.jpeg) Lamps specifications (.pdf)

Further details about the geometry, the CFD model and the variation of the boundaries condition were directly discussed with Laury Chaerle and Dominique Van Der Straeten from Gent University.

1.2. Geometry

The geometry of the chamber was modeled according to the technical drawing provided by the European space agency (ESA) and on the basis of the measurements made onsite during the visit to the chamber prototype hosted in the Chemical Engineering Department of the Escola Tècnica Superior d'Enginyeria (ETSE) of the Universitat Autònoma de Barcelona (UAB).
The schematic exterior view of the prototype is shown in Figure 1.

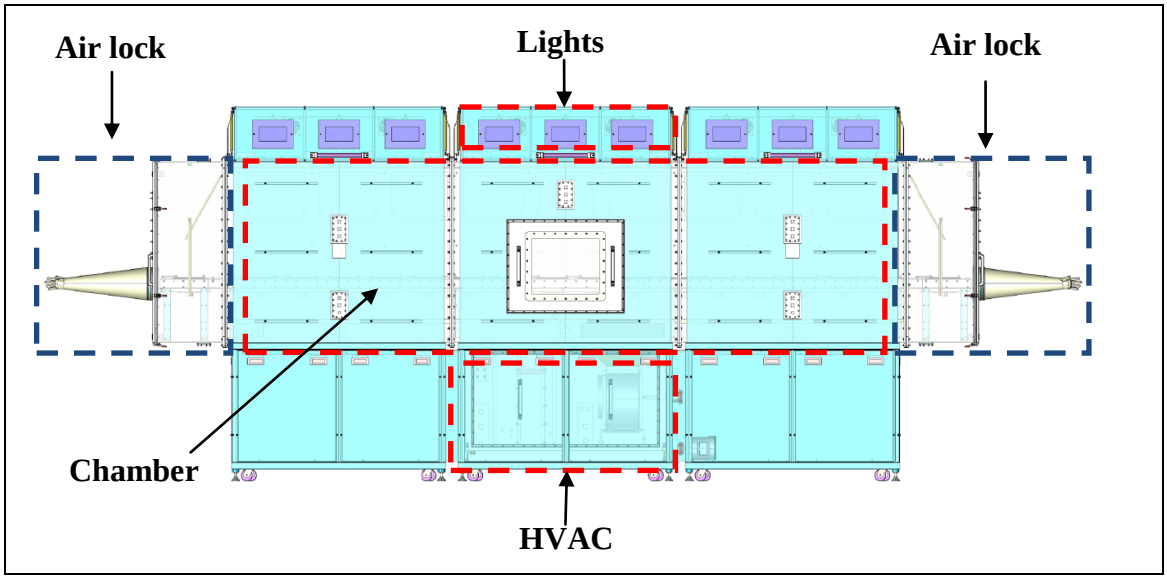

Figure 1 Exterior view diagram of the higher plant chamber

The blue highlighted air locks located at the end of the chamber are neglected in the present investigation. The Teflon fabric doors placed on their interior side assure a good airtightness and can be assumed as closed walls.

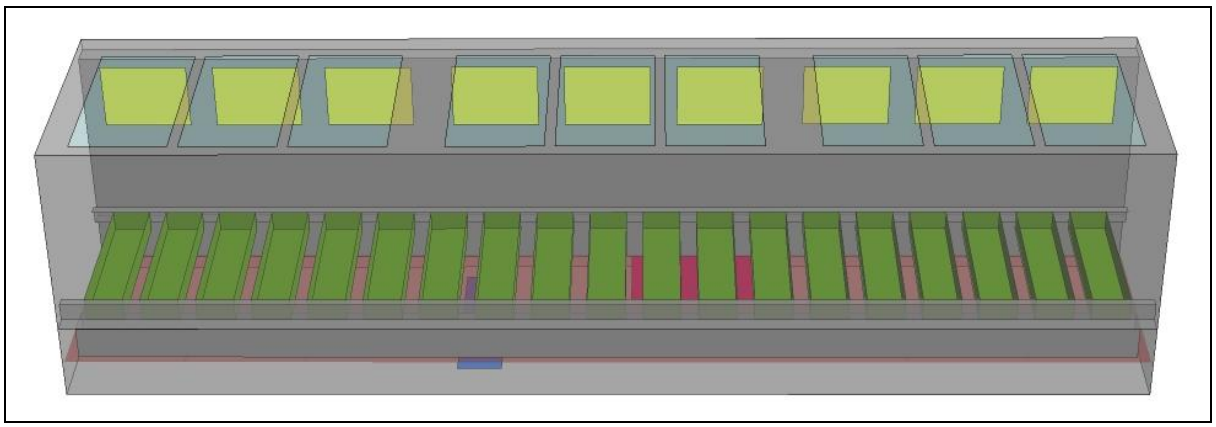

Figure 2 Chamber geometry

Without the air locks, the remaining geometry was divided into three functional subdomains:

- Chamber
- HVAC
- Lights

The general layout of the chamber sub domain is shown in Figure 2. The air flow enters from the inlet placed at the bottom of the chamber (Figure 3 D) and is directed by a connection duct (Figure 3 C) into the plenum located on one of the side walls. Then the air moves through the grilles positioned on the upper side of the plenum and flows into the growing volume. Finally it reaches the outlet placed below the tray support (Figure 3 D).

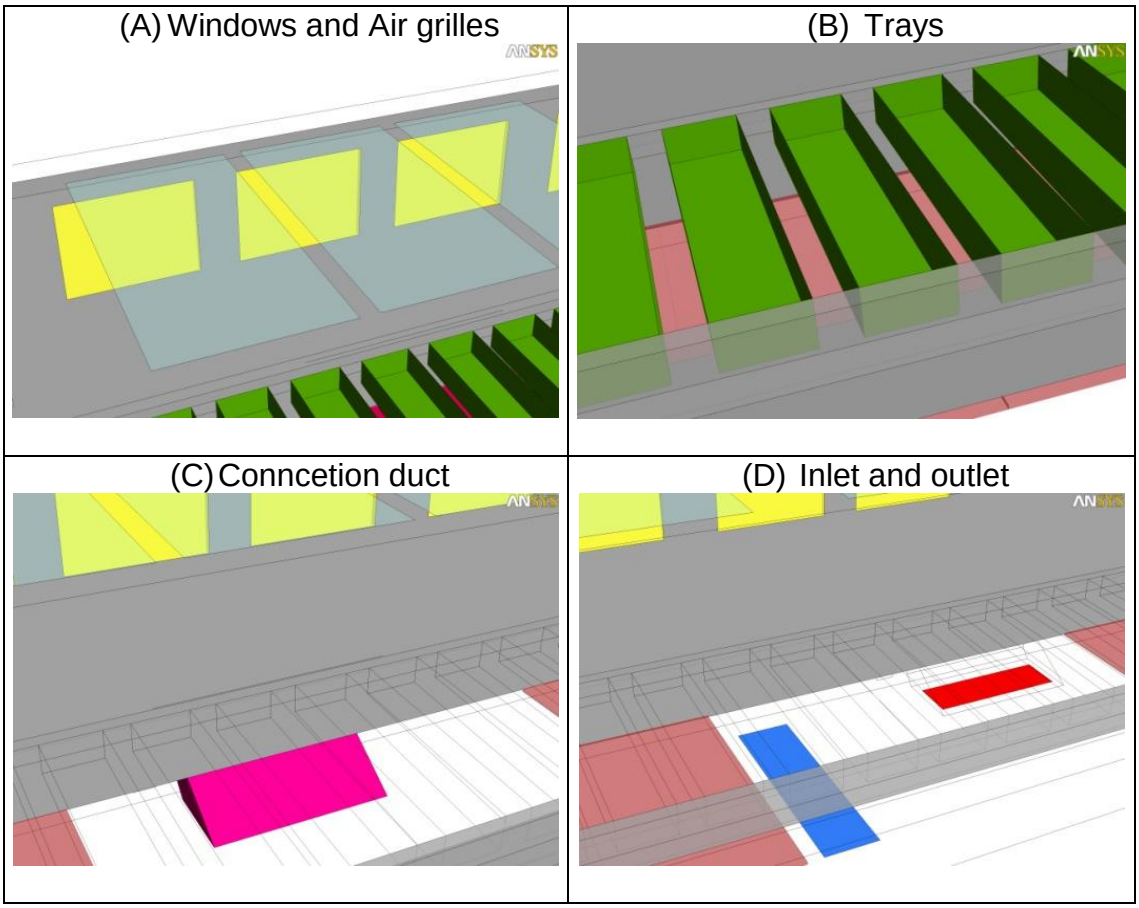

Figure 3 Detailed view of the chamber geometry

Directly connected to the chamber is the HVAC sub domain where air is conditioned for temperature and humidity and is re-circulated inside the plant growing volume. The general layout of the HVAC is shown in Figure 4.

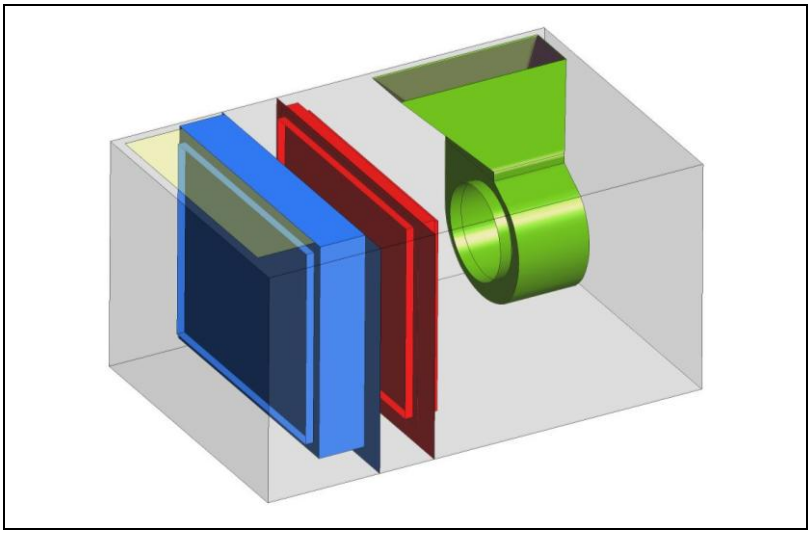

Figure 4 HVAC geometry

The components mounted inside the HVAC are highlighted in Figure 5. The blower with the diffuser placed in proximity of the outlet region and two bulkheads which isolate the heat (cold and hot) exchange coils are visible.

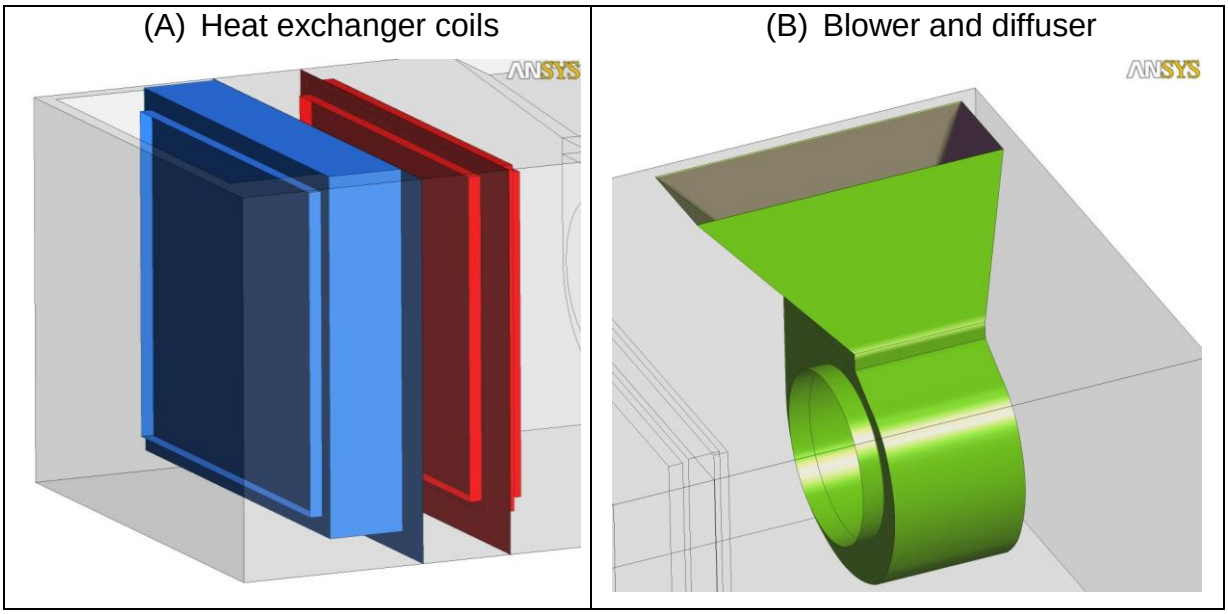

Figure 5 Detailed view of the HVAC domain

Finally at the top of the chamber the lights sub domain made up of a lamp loft with two fans for temperature control (see Figure 6) is located. Three lamps are placed inside the loft and provide illumination to the plants through a tempered glass roof.

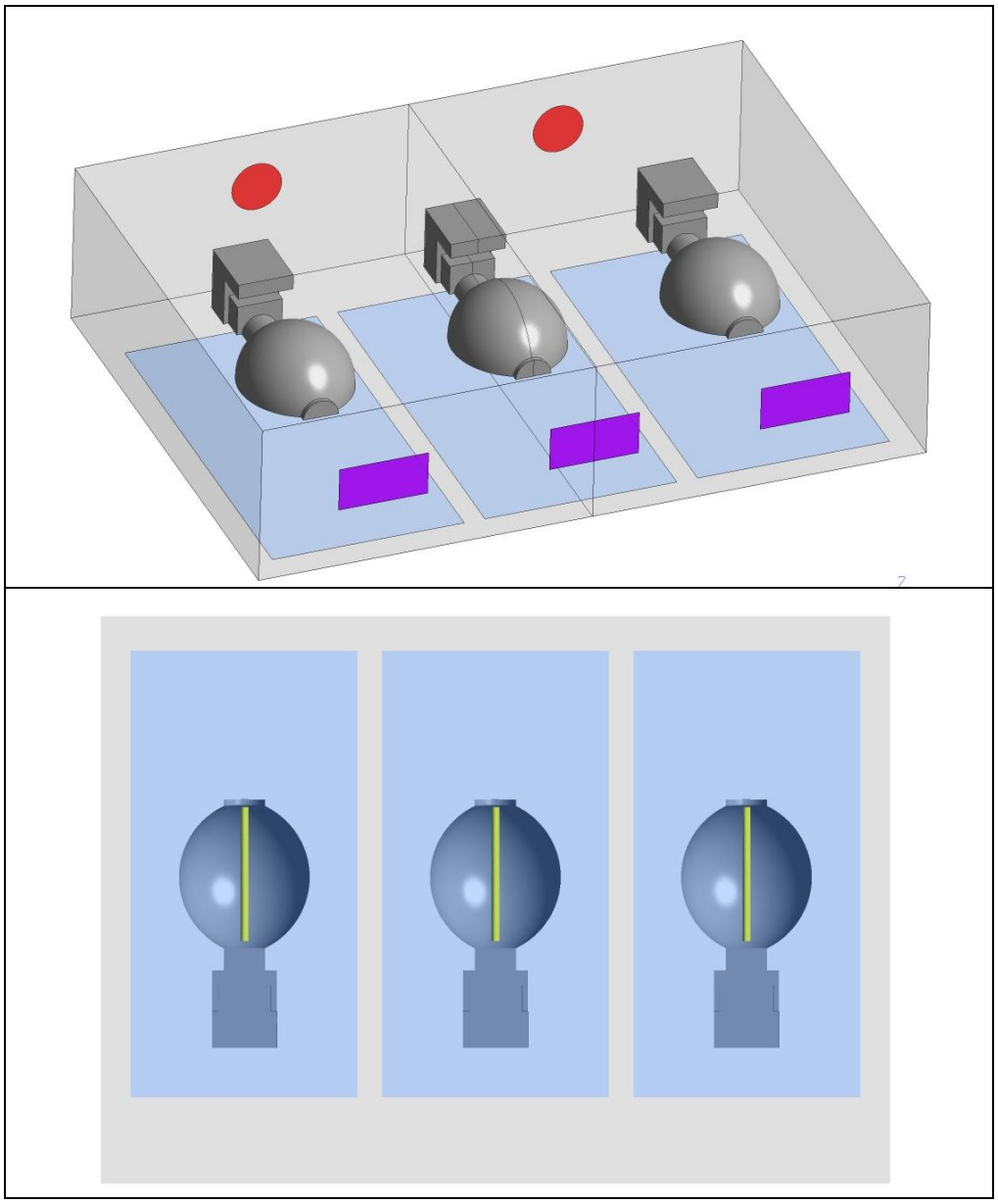

Figure 6 Light domain geometry

1.3. Computational grid

The grids of the computational domain were generated with the HEXA module of the meshing code ANSYS ICEM. The following table resumes the mesh features for each sub domain:

	N. Elements	*Minimum angle*	*Aspect ratio*
Chamber	1 847 676	29.7	69
HVAC	1 617 355	11.2	46
Lights	598 745	16.1	108
Total	4 063 776		

Table 1 Mesh features

See below for some details of the mesh

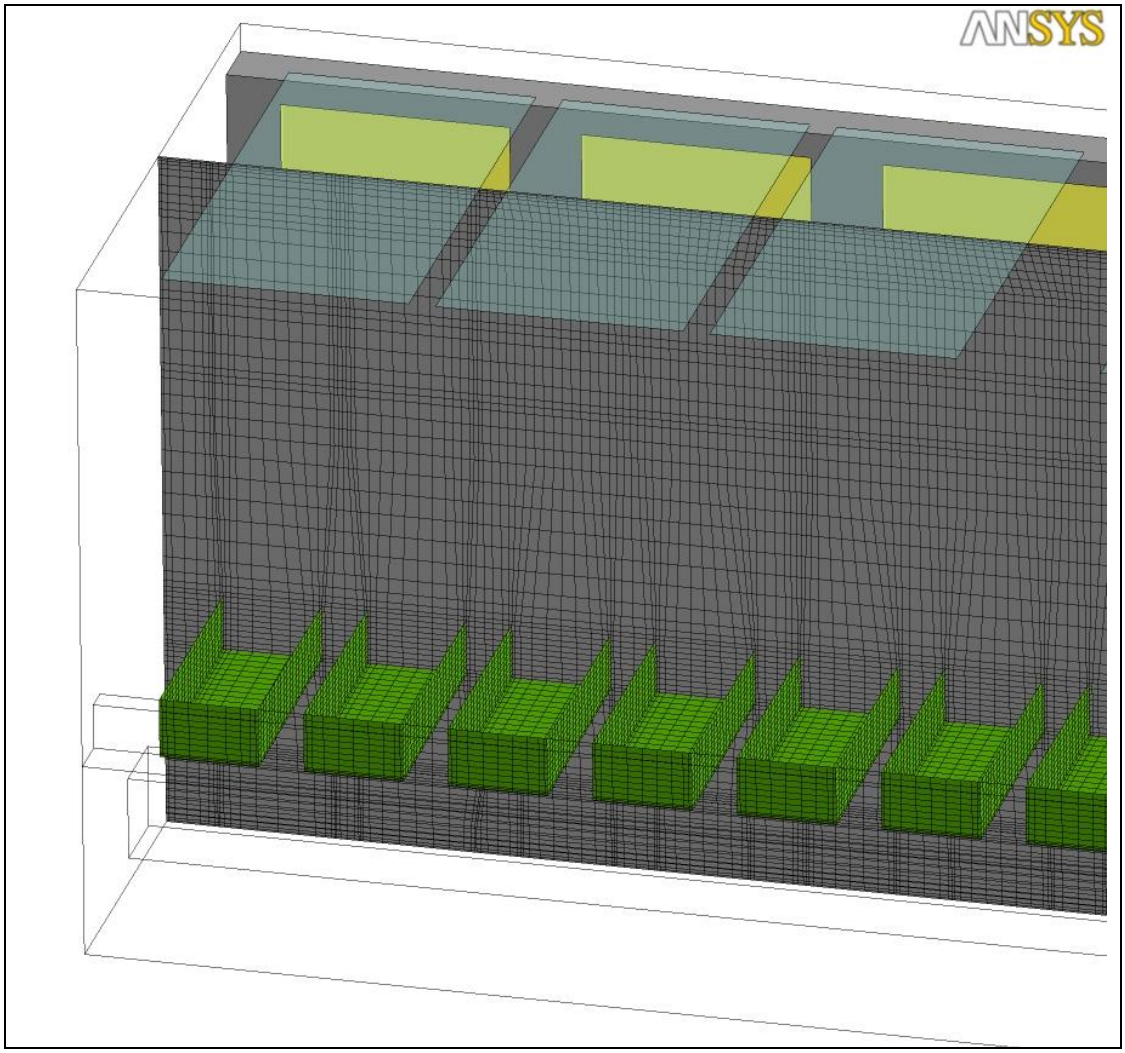

Figure 7 Chamber mesh: longitudinal section

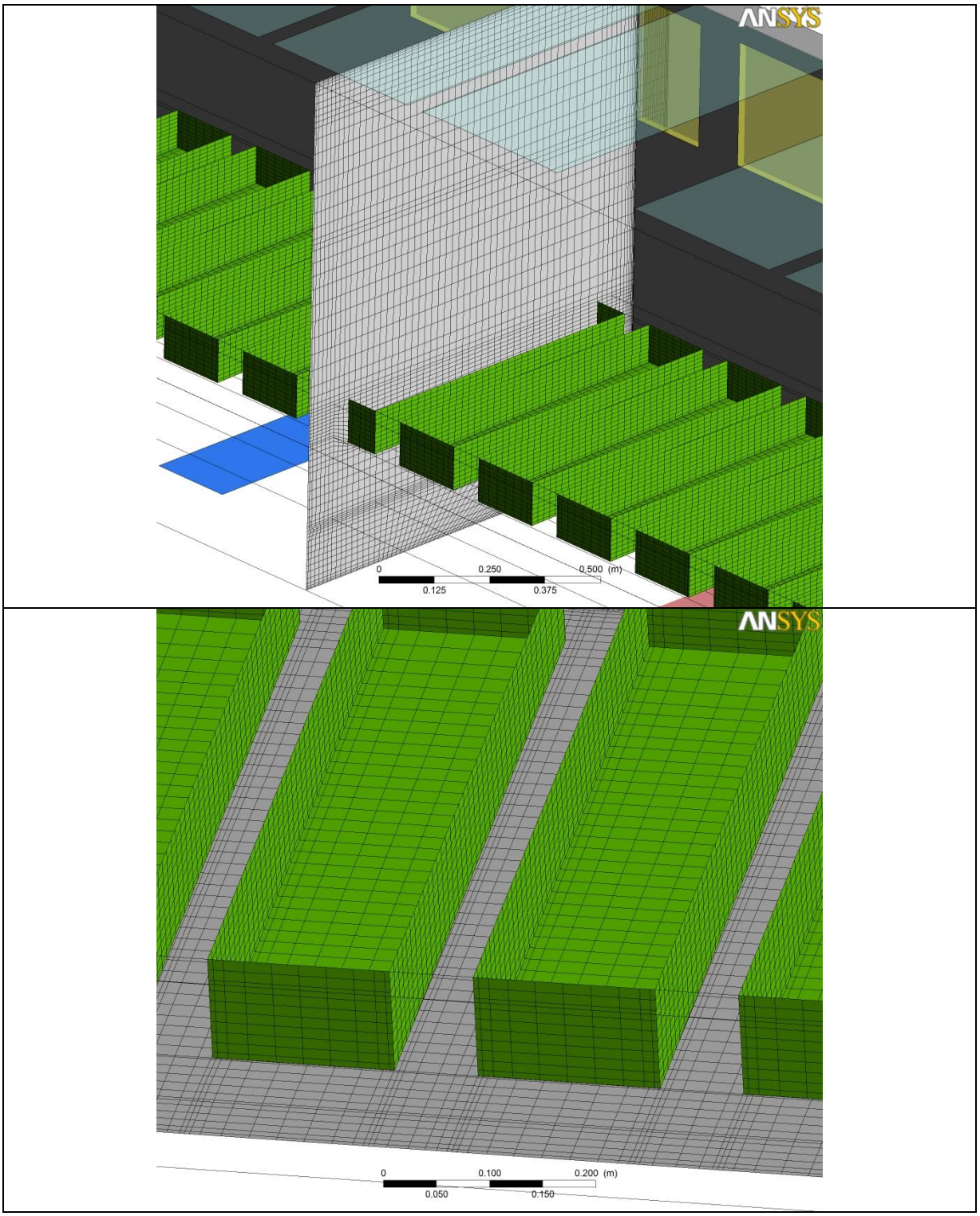

Figure 8 Chamber mesh: two orthogonal sections

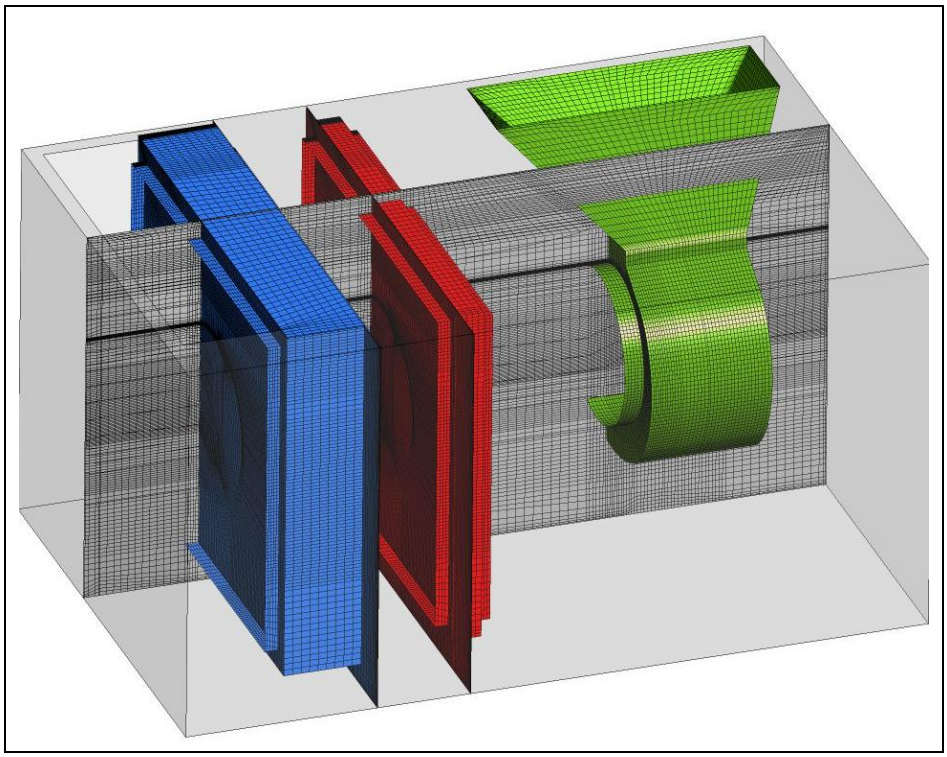

Figure 9 HVAC mesh: longitudinal section

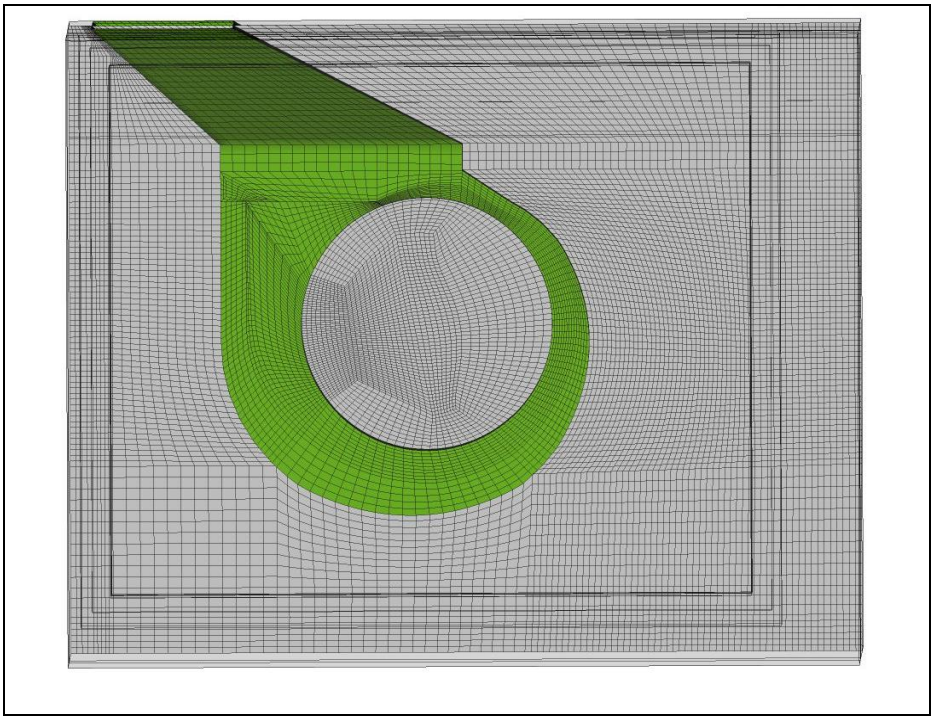

Figure 10 HVAC mesh: blower region

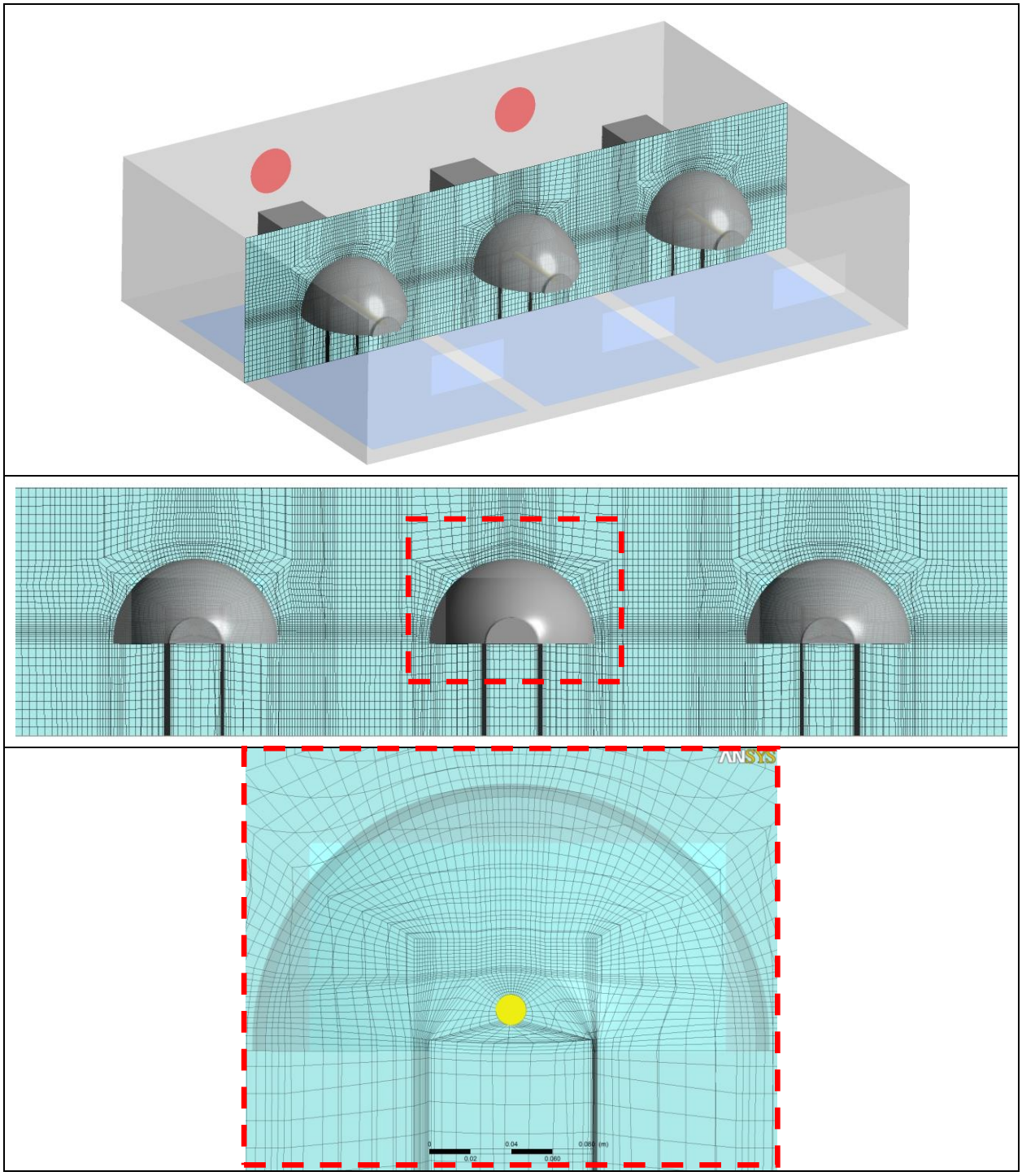

Figure 11 Lights mesh: longitudinal section

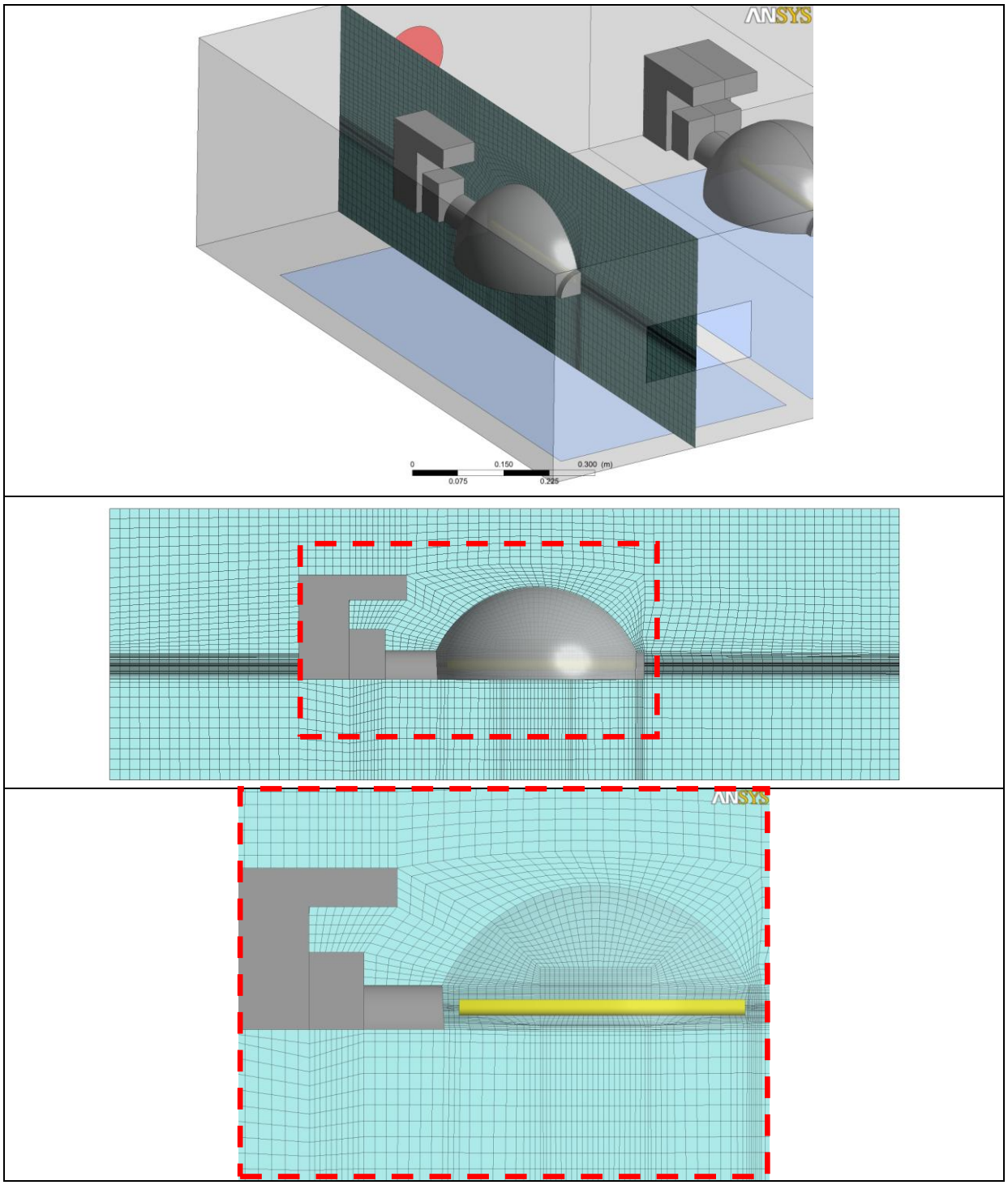

Figure 12 Lights mesh: transversal section

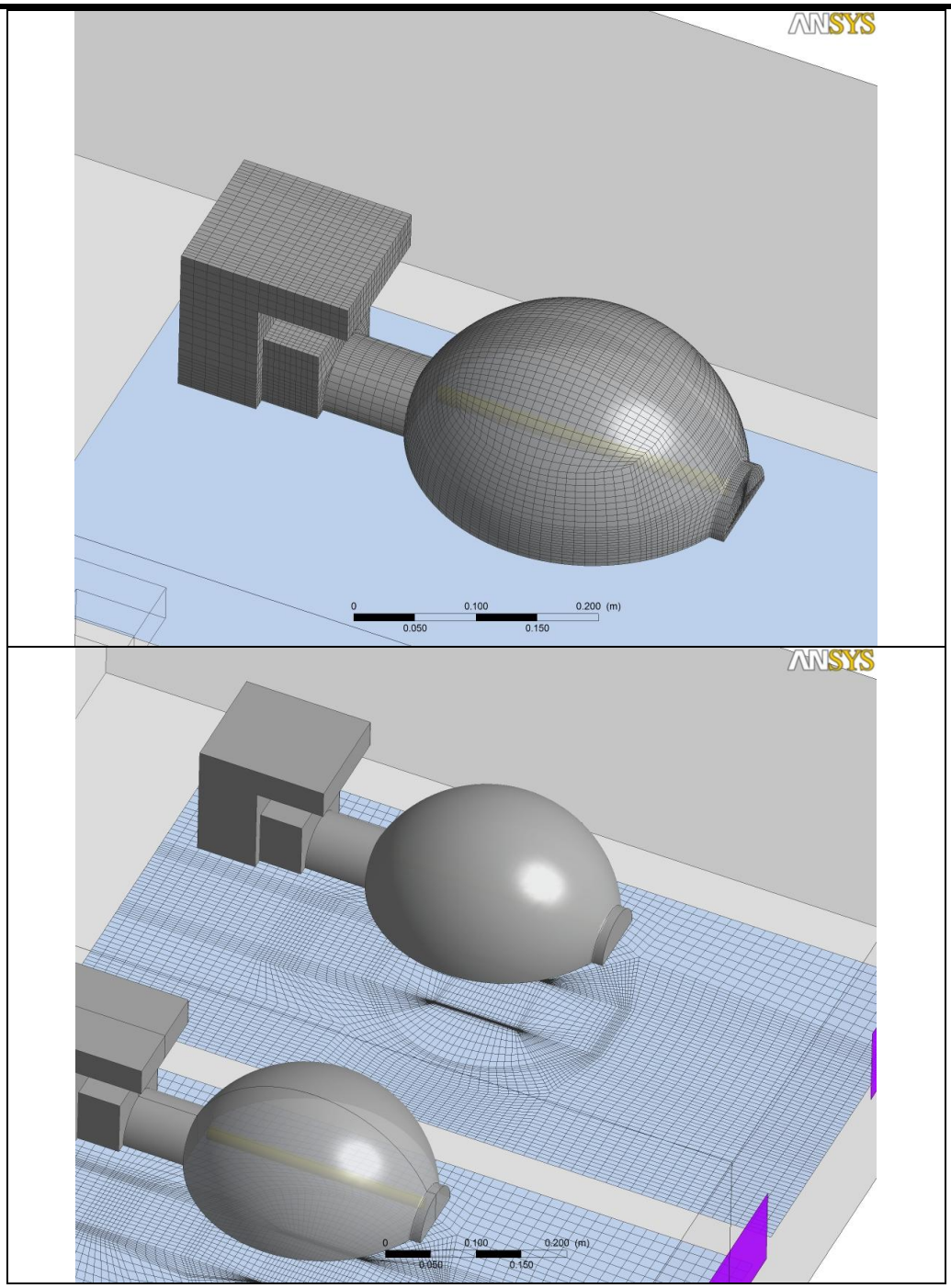

Figure 13 Lights mesh details

1.4. Physical properties and boundary conditions

Three local models corresponding to the three functional sub domains were implemented. The physical assumption common to all the sub domains are summarized below:

Fluid model	Air ideal gas
Flow	Steady
	Subsonic
	Compressible
	Turbulent
Turbulence model	k-ε

Table 2 Numerical procedure

In the following the specific physical details and boundary conditions of each sub domain are given.

1.4.1. Chamber

Two configurations have been analyzed. One with a deflector placed downstream of the connection duct and one without deflector. The real hardware does not include a deflector. All the experimental tests were conducted in the configuration without the deflector. The figure below shows the two configurations.

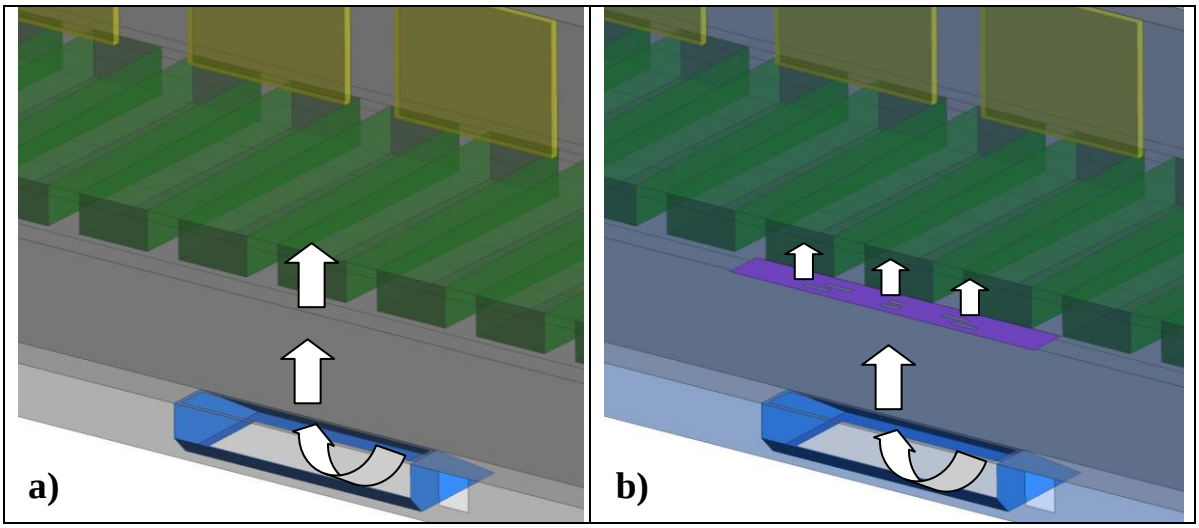

Figure 14 Analyzed configurations: a) No deflector; b) Deflector installed.

For both configurations the chamber is supposed to be in stable thermal condition at 25°C with the lights turned off. The energy equation is not solved.
All the internal and external walls of the domain have been treated as smooth with a no slip condition applied.

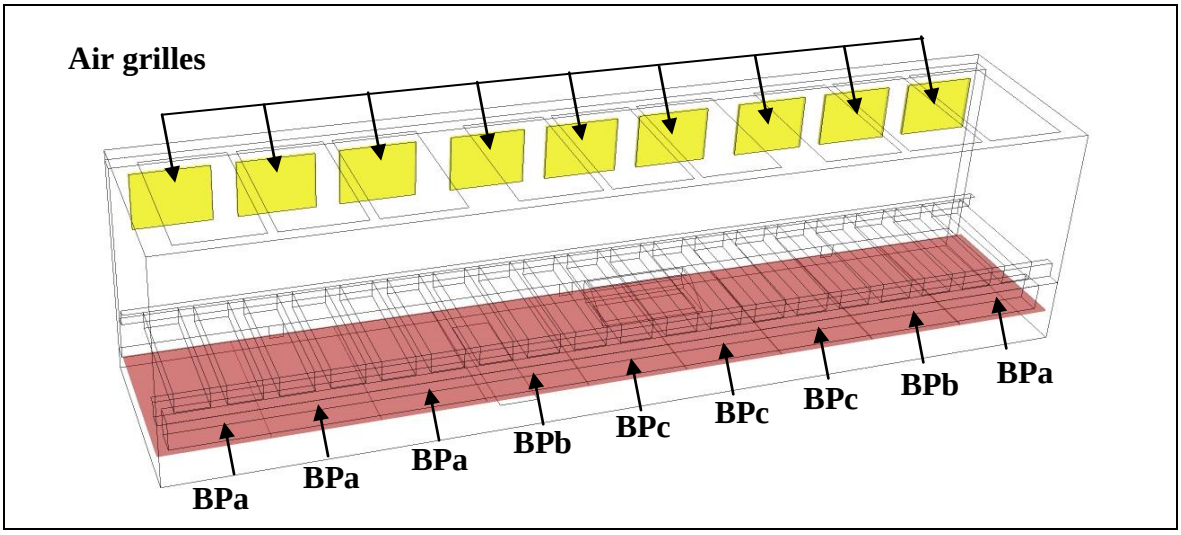

Figure 15 Porous regions: air grilles and balancing panels (BP)

The balancing panels and the air grilles shown in Figure 15 have been modeled as 3D porous regions assigning a Resistance Loss Coefficient K_{loss} which produces a localized pressure gradient according to the relation:

$$\frac{\Delta P}{L} = -\frac{\rho}{2} V^2 K_{loss}$$

where V is the gas velocity, ρ is the gas density and L is the thickness of the resistant region. The K_{loss} coefficient has been estimated using an empirical law, which links the porosity σ to the resistance loss coefficient.

$$K_{loss} = \frac{f}{L} \quad ; \quad f = \left(\frac{1}{\sigma \cdot c} - 1 \right)^2 \quad ; \quad c = \frac{0.6125 - 0.5148\sqrt{\sigma}}{1 - 0.9023\sqrt{\sigma}}$$

The following table resumes the k_{loss} calculated for the three types of balancing panels and for the air grille:

	K_{loss} [m^{-1}]
Air grille	1000
BP A	26000
BP B	142000
BP C	224000

Table 3 K_{loss} coefficients for the air grille and for the balancing panels

The flow rate imposed at the inlet of the chamber (see Figure 16 – Domain In) is the stable working condition of the blower mounted in the HVAC domain. The performance curve of the blower is shown in Figure 17.

The Teflon bags managing the atmospheric pressure in the chamber are modeled as openings where the atmospheric pressure is imposed (see Figure 16 – Atmospheric control (AC)). At the openings, when the pressure level is lower than the atmospheric one, the flow enters the domain. Otherwise the flow is directed out of the chamber. This behavior of the openings represents the reality.

Table 4 and Figure 16 summarize the type and the locations of boundary condition applied to the chamber.

Location	Boundary Type	Boundary details
Domain in	Inlet	Mass flow rate 0.84 [kg/s]
Domain out	Outlet	Average static pressure 101325 [Pa]
Atmospheric control (AC)	Opening	Static pressure 101325 [Pa]

Table 4 Types of chamber boundary conditions

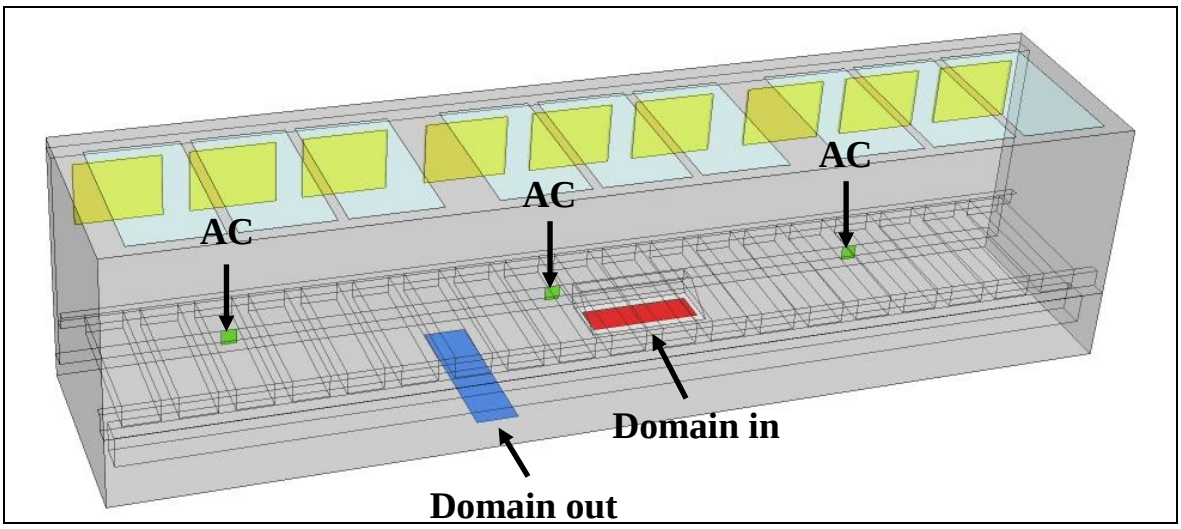

Figure 16 Locations of chamber boundary conditions

1.4.2. HVAC

As for the chamber domain, the HVAC domain is supposed to be in stable thermal condition at 25°C and the energy equation is not solved.

All the internal and external walls of the domain are treated as smooth with a no slip condition applied.

The blower is modeled by the addition of a momentum source term to the standard fluid flow equations (see **Figure 18**.c for the source location). The operating conditions are directly worked out by the CFD code where the geometrical dimension and the performance data of the blower are applied (max pressure drop 2.8 [In.wg], max flow rate 3000 [cfm]).

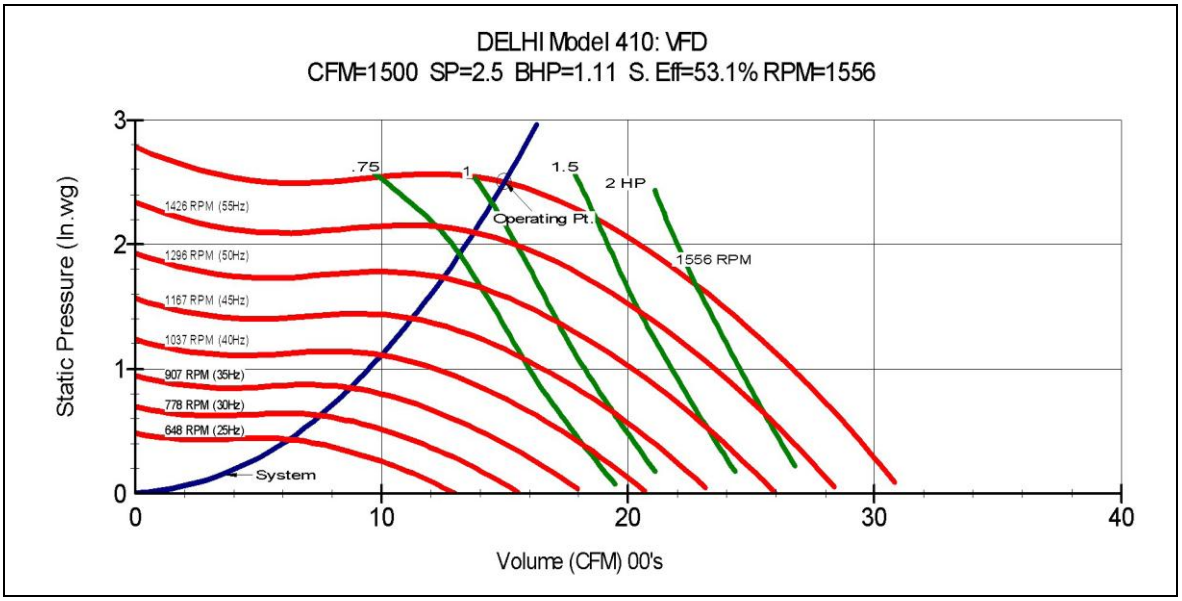

Figure 17 Blower performance curve

The water coils (chiller and heater) are modeled by the addition of a momentum sink in the governing momentum equations. The momentum loss in the stream wise direction is calculated as:

$$\frac{\partial p}{\partial x_i} = -aU_i - b|U|U_i$$

where a is the linear loss coefficient, b is the quadratic loss coefficient, U_i is the local velocity in the stream wise direction and $\partial p/\partial x_i$ is the pressure drop gradient in the stream wise direction.

Experimental data available in the form of pressure drop against velocity through the porous component were used to determine the value of the quadratic loss coefficients (112.52 [kg m^{-4}] for the cooler and 168.28 [kg m^{-4}] for the heater) while the linear loss coefficient was neglected for both the water coils.

Table 5 and Figure 18 summarize the type and the locations of boundary condition applied to the HVAC.

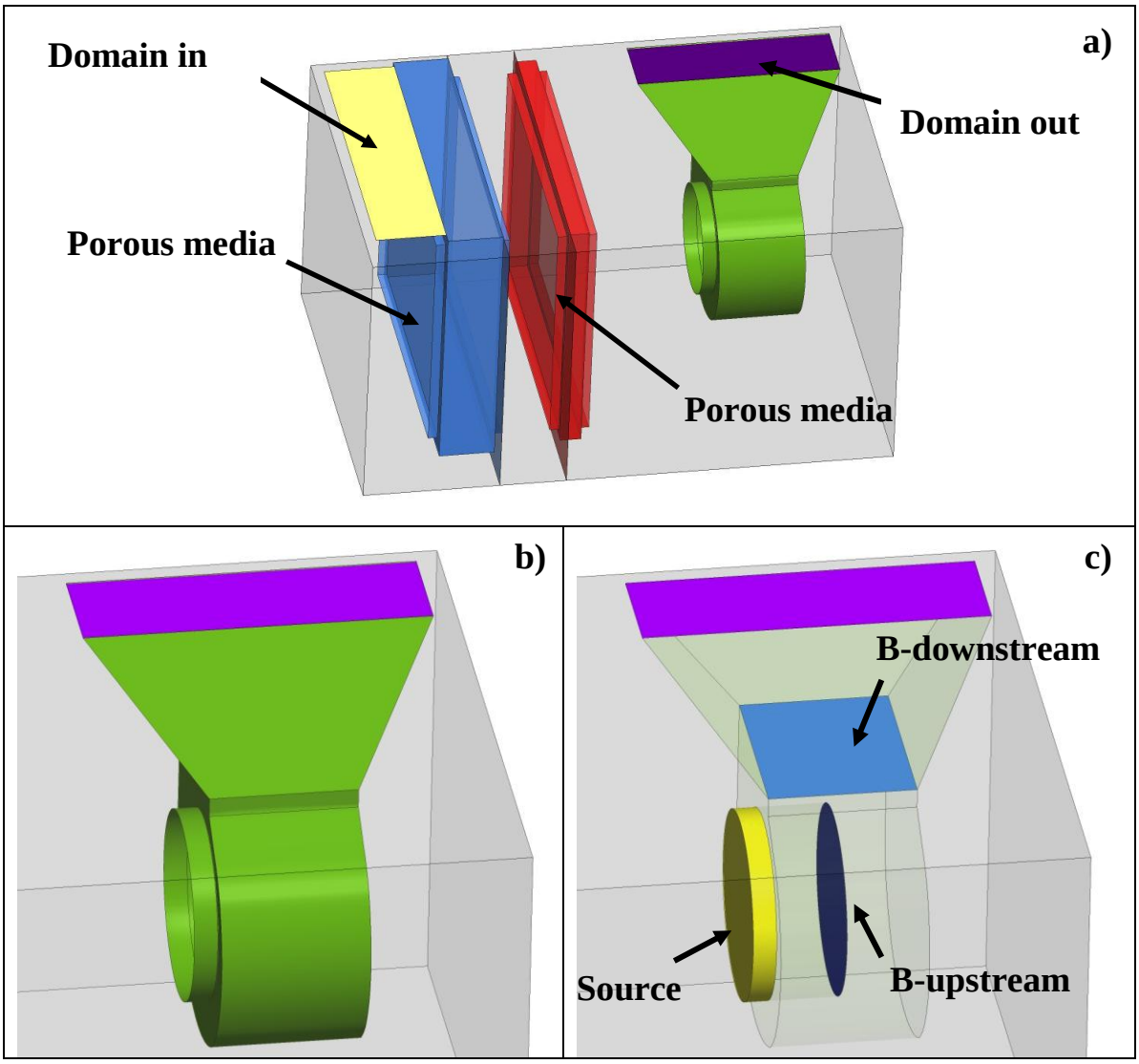

Figure 18 Locations of HVAC boundary conditions

Location	Boundary Type	Boundary details
Domain in	opening	Relative static pressure 0 [Pa]
B-upstream	outlet	Static pressure at B-downstream
B-downstream	inlet	Mass flow at B-upstream
Domain out	outlet	Relative static pressure 194 [Pa]

Table 5 HVAC boundary conditions types and values

1.4.3. Lights

The energy equation (thermal energy) has been taken into account, as well as the radiation following the Montecarlo model. The radiation model will be analyzed more in detail in the next paragraph.

The buoyancy effect is not negligible and was simulated with the full buoyancy model.

Figure 19 shows the location of all the boundary conditions applied to the lights domain.

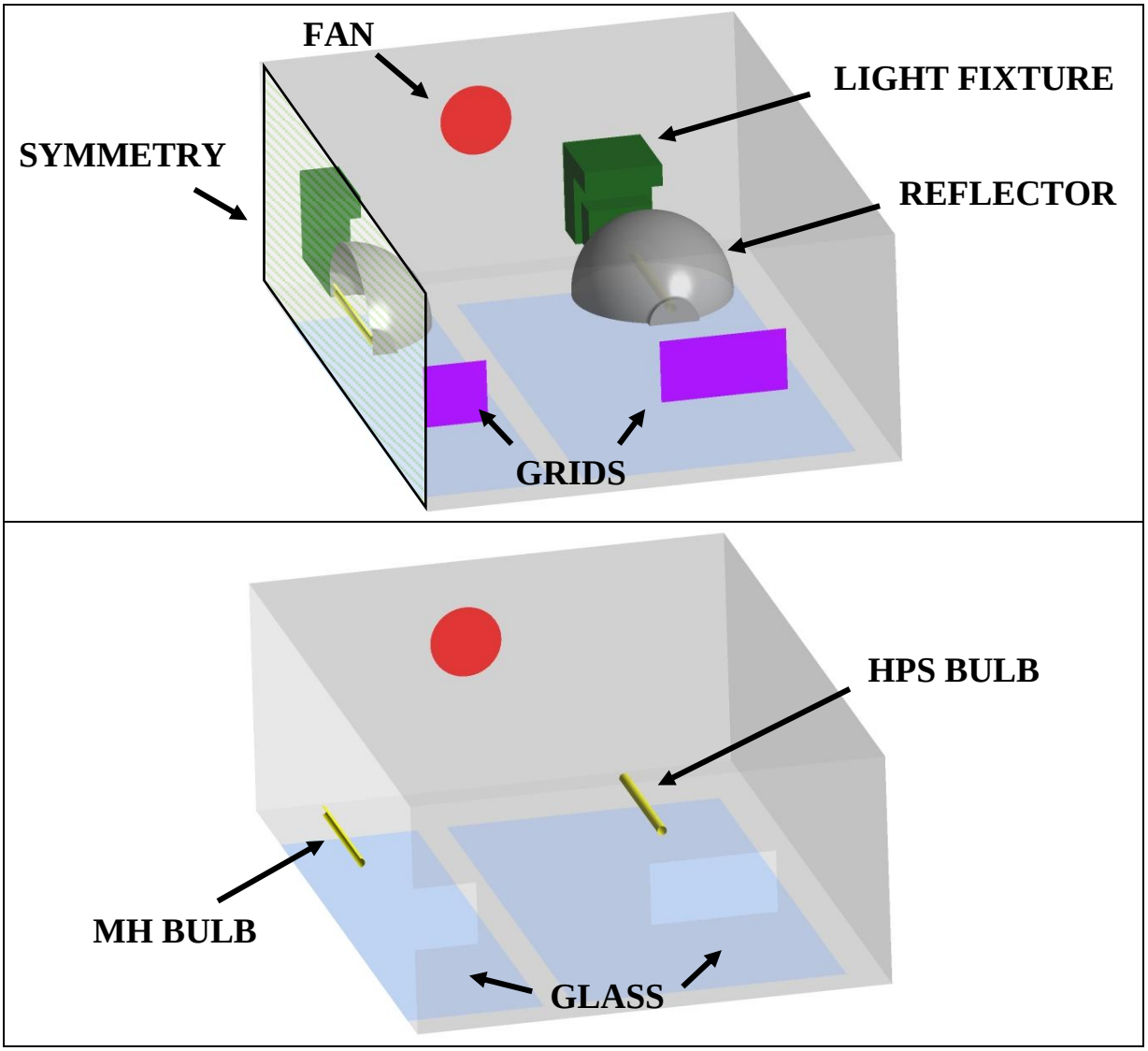

Figure 19 Lights boundary conditions locations

In the following the set of conditions specified for the solution of the light domain are summarized:

SYMMETRY: A symmetry boundary conditions has been placed on the middle plane of the lamp loft model (see Figure 19) since the geometry and the expected pattern of the flow/thermal solution are identical on either side of a dividing plane. The symmetry assumption results in a reduction of the computational costs.

HPS BULB: The HPS bulb has been considered as a black body at a uniform temperature of 375[C]. This temperature was set according to the technical datasheet of the lamp (minimum bulb temperature 350[C], Maximum bulb temperature 400[C]) (Philips, 2007).
The convective heat flux transmitted from the lamp to the surroundings is represented by applying the constant surface temperature. The amount of convective heat was found to be 10% of the supplied power which is in agreement with general values for HPS lamps. The share of radiative heat is then calculated as the difference between total supplied power (600[W]) and the power transmitted by convection.
The amount of visible light emitted from the bulb is assumed to be 30% of the supplied electrical power (600[W]) (University of Guelph CESRF, 2006). The emissivity values of the bulb for each spectral band in the visible range are shown in the table below:

Bands (nm)		Emissivity
From	to	
380	510	0.14
510	650	0.8
650	780	0.06

Table 6 HPS emissivity in the visible spectrum

The share of the radiation emitted from the bulb in the ultra violet (UV) and in the infrared (IR) spectrum has been included in the thermal radiation calculation with two additional bands. The UV band ranges from 100 to 380 [nm] with an emissivity value on the bulb of 0.1 .The IR band ranges from 780 to 100000 [nm] with an emissivity of 0.9.

MH BULB: as for the HPS lamps, the MH bulb has been considered as black body with the same temperature uniformly applied at the surface.
The amount of visible light emitted from the bulb is assumed to be 55% of the supplied electrical power (400[W]) (University of Guelph CESRF, 2006). The emissivity values of the bulb for each spectral bands in the visible range are shown in the table below:

Bands (nm)		Emissivity
From	to	
380	510	0.27
510	650	0.66

650	780	0.07

Table 7 MH emissivity in the visible spectrum

The share of radiation emitted from the MH bulb in the UV and in the IR bands has been treated in the same manner as for the HPS bulb.

FAN: An inlet condition has been set at the fan mounted on the back wall of the loft. To be conservative the fan was supposed to work under high impedance condition (see Figure 20). A flow rate of 0.02123 [kg s^{-1}] has been imposed normal to the boundary with a static temperature of 25[C].

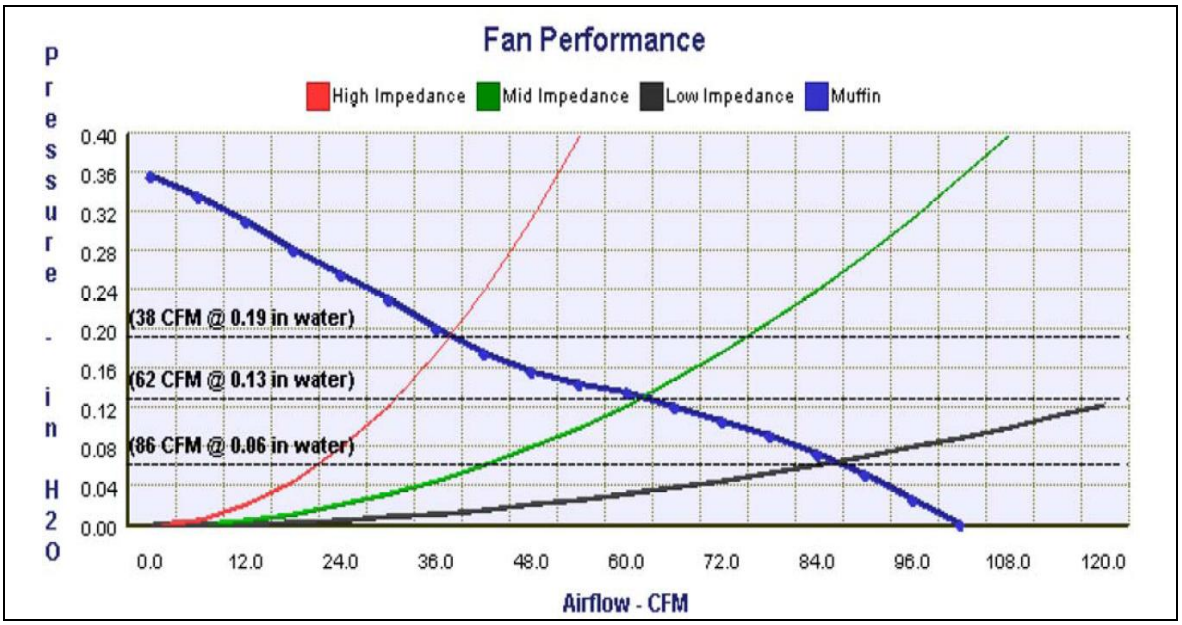

Figure 20 Fan Performance curve

GRIDS: on the wall opposite to the fan location, three grids are present open to the external air. On these boundaries an "opening" condition has been set thus allowing the fluid to freely enter and exit the computational domain.
The entering conditions have been set as:
Relative pressure = 0 [Pa]
Temperature = 25[C]

LOFT, LIGHT FIXTURE: a wall boundary condition has been imposed on the loft and on the light fixture. For both of them, a no slip option has been used for modeling the influence of the wall boundary on mass and momentum. Moreover both, the loft and the reflector base are assumed to be opaque to thermal radiation. The convective heat transfer assumptions to the outside are different. The heat flux from the loft has been implicitly specified using an external

heat transfer coefficient HTC (20 W m^{-2} K^{-1}) and an outside or external boundary temperature, T_{amb} (25[C]) while the light fixture has been treated as adiabatic.

REFLECTORS: the reflectors have been modeled using a thin surface which has been assigned with a wall boundary condition on each side of the 2D region. The thin surface has been considered as adiabatic and opaque to thermal radiation. The same diffusive fraction has been applied on both sides (diffusive fraction 1) while different emissivity were specified for the internal and the external side (internal emissivity 0.1, external emissivity 0.9) where the internal side is the one facing the lamp bulb.

GLASS: a wall boundary condition has been set on the glass. A no slip option has been used for modeling the influence of the wall boundary on mass and momentum. The permeation of heat through the glass has been modeled implicitly by imposing an external heat transfer coefficient HTC (20 W m^{-2} K^{-1}) and an outside or external boundary temperature, T_{amb} (25[C]). The spectral radiative properties of the boundary has been set according to the technical datasheet of a common glass (see Figure 21, Nicolau V. P., 2001). So the emissivity of the glass was calculated from one minus the experimental data of reflectivity and transmissivity. Finally a diffuse fraction value of 0.9 was imposed at the glass.

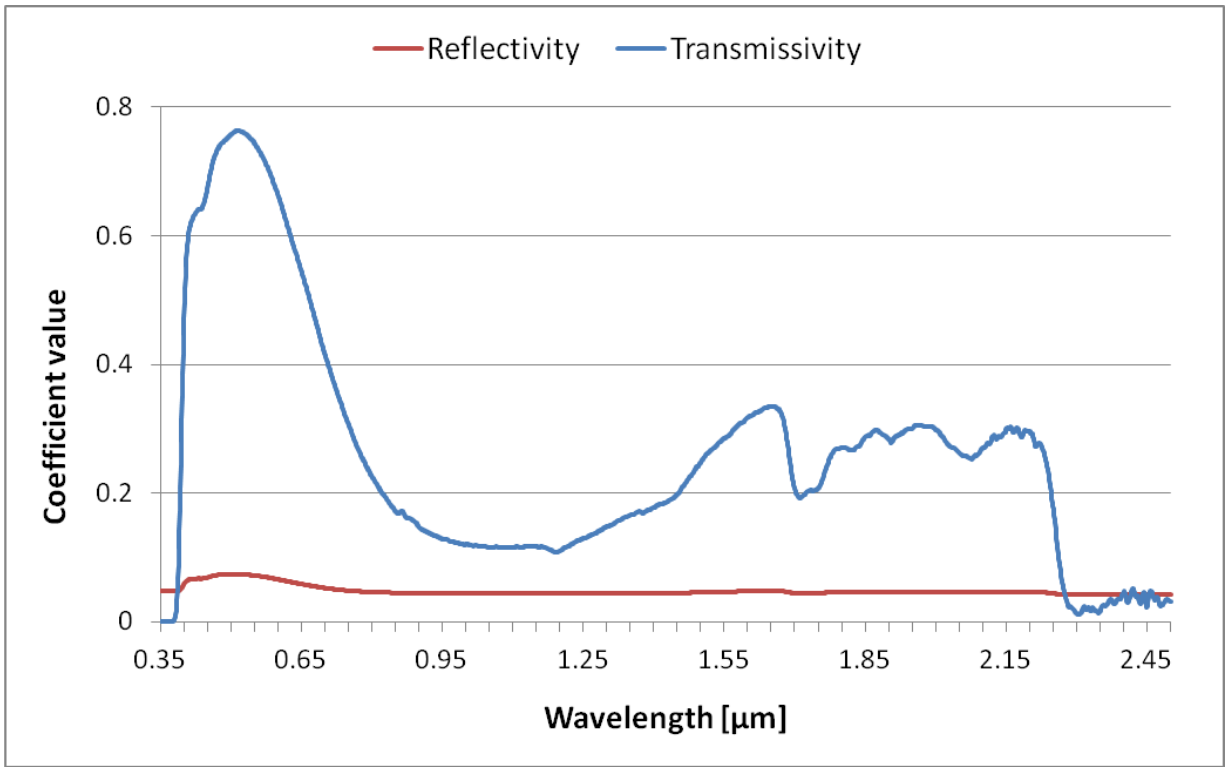

Figure 21 Common Glass data: reflectivity and transmissivity

1.4.3.1. Radiation model

The goal of radiation modeling is to solve the radiation transport equation in order to calculate the source term to be introduced in the energy equation and the radiative heat flux at walls. The spectral radiative transfer equation can be written as:

$$\frac{dI_\upsilon(\mathbf{r},\mathbf{s})}{ds} = -(K_{a\upsilon} + K_{s\upsilon})I_\upsilon(\mathbf{r},\mathbf{s}) + K_{a\upsilon}I_b(\upsilon,T) + \frac{K_{s\upsilon}}{4\pi}\int_{4\pi} dI_\upsilon(\mathbf{r},\mathbf{s}')\Phi(\mathbf{s}\bullet\mathbf{s}')d\Omega', \qquad (3.1)$$

where ν is the frequency, **r** and **s** the position and direction vectors respectively, K_a and K_s the absorption and scattering coefficient respectively, I_b the blackbody emission intensity, I_ν the spectral radiation intensity which depends on position and direction, T the local absolute temperature, **Ω** the solid angle, **Φ** the in-scattering phase function. Equation (3.1) is written for frequency **ν** and all quantities indexed **ν** are, in general, frequency dependant. The first term on the right hand side represents the energy gained by absorption by a travelling beam of radiation, the second the energy lost by emission and the third the energy redistributed by scattering.

Due to the dependence on 3 spatial coordinates, 2 local direction coordinates, and frequency, the formal solution of the radiative transfer equation is very time consuming and both directional and spectral approximations are usually adopted in the framework of numerical codes. In the present work the Montecarlo model is used for the directional approximation and the Multiband model is used for the spectral approximation.

The Monte Carlo model assumes that the radiation intensity is proportional to the differential angular flux of photons and you can think of the radiation field as a photon gas. For this gas, K_a is the probability per unit length that a photon is absorbed at a given frequency. Therefore, the mean radiation intensity, I is proportional to the distance traveled by a photon in unit volume at r, in unit time. Similarly the spectral radiative heat flux is proportional to the rate of incidence of photons on the surface at r, since volumetric absorption is proportional to the rate of absorption of photons. Hence:

- By following a typical selection of photons and tallying in each volume element the distance traveled, the mean total intensity is obtained.
- By following a typical selection of photons and tallying in each volume element the distance times the absorption coefficient, the mean total absorbed intensity is obtained.

- By following a typical selection of photons and tallying in each volume element the distance times the scattering coefficient, the mean total scattered intensity is obtained.
- By also tallying the number of photons incident on a surface and this number times the emissivity, the mean total radiative flux and the mean absorbed flux are obtained.

Concerning the spectral approximation, the multiband model discretizes the spectrum into bands of finite width and assumes that radiation quantities are uniform within the band. Then, the total radiative heat flux is computed by adding the results within each band. Five bands were used: three bands in the visible range, one in the Ultra Violet (UV) and one in the Infra Red (IR).

1.5. Numerical procedure

The analyses of the three domains have been set up following the same numerical:

- Analysis type
  - Steady state
- Advection Scheme
  - High Resolution (2^{nd} order accurate)
- Turbulence Numerics
  - First Order
- Fluid False Timescale Control
  - Time scale control: Autotimescale
  - Length scale option: Conservative
  - Timescale factor: 1.0
- Convergence Criteria:
  - Residual Target: 1.0E-6

This set up method is a good compromise between result quality and analysis speed, without interfering with its robustness.

1.6. Results

1.6.1. Chamber

The fluid dynamic fields of the two configurations of the chamber described in paragraph 1.4.1 are herein shown and investigated.
Figure 22 shows how the presence of the deflector influence the velocity field in the plenum region. Without the deflector, the air flows to the top of the plenum and then moves in the lateral directions. With the deflector (perforated plate) installed, the main part of the flow is forced to move laterally.

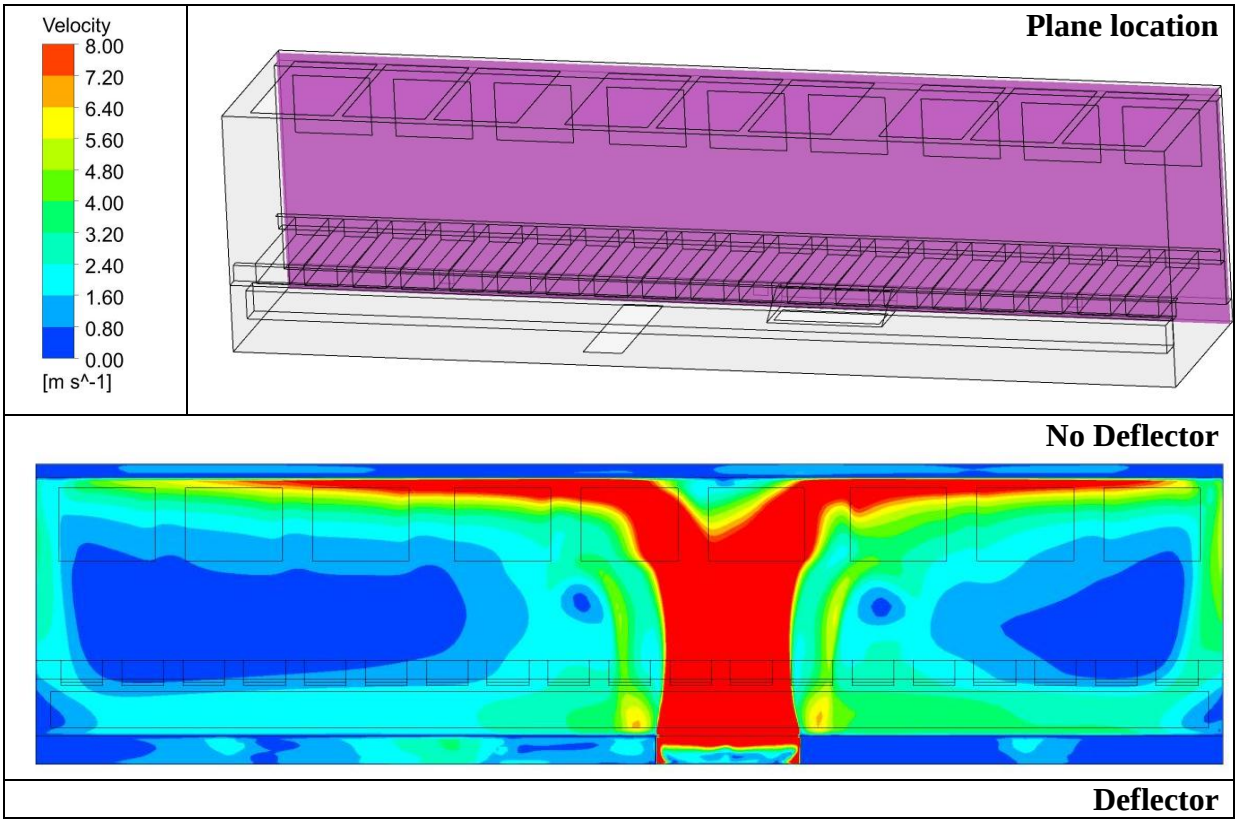

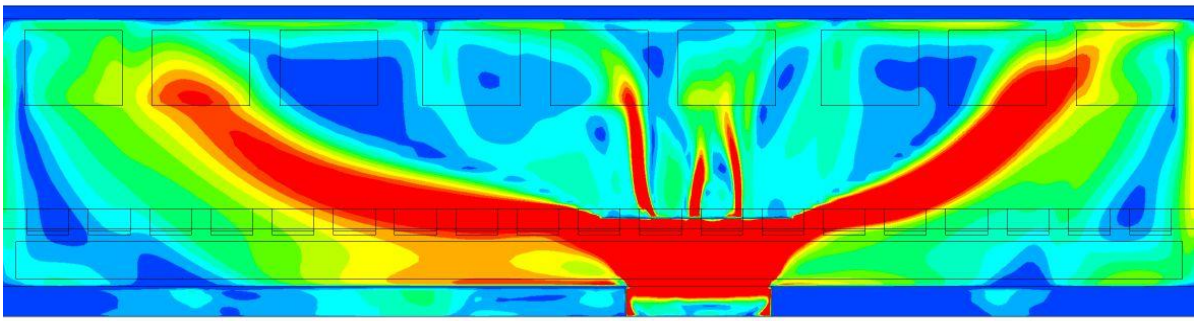

Figure 22 Chamber: velocity contours in the plenum region

The behavior of the velocity field seen in the previous figure is supported by the pressure field shown in Figure 23: pressure gradients correspond to velocity variation in module and directions.

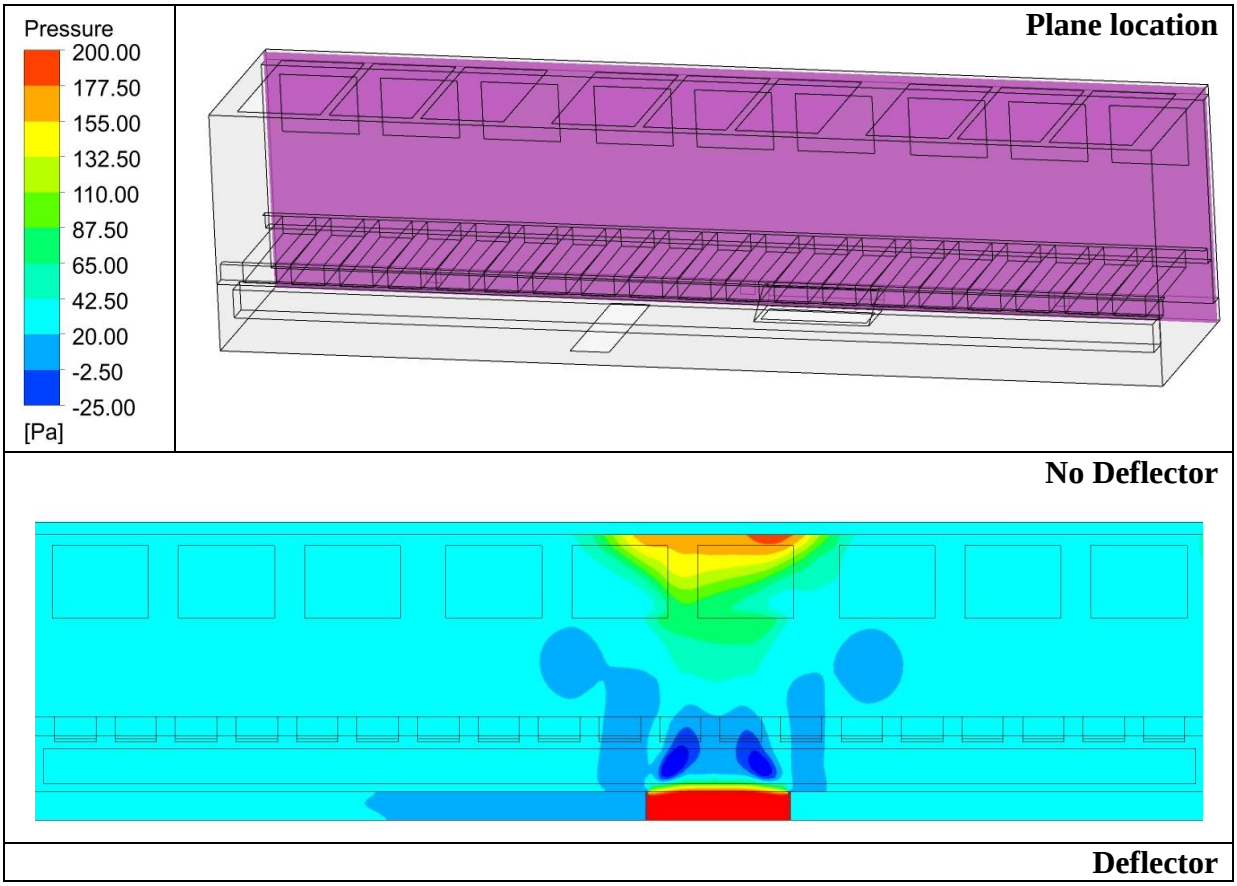

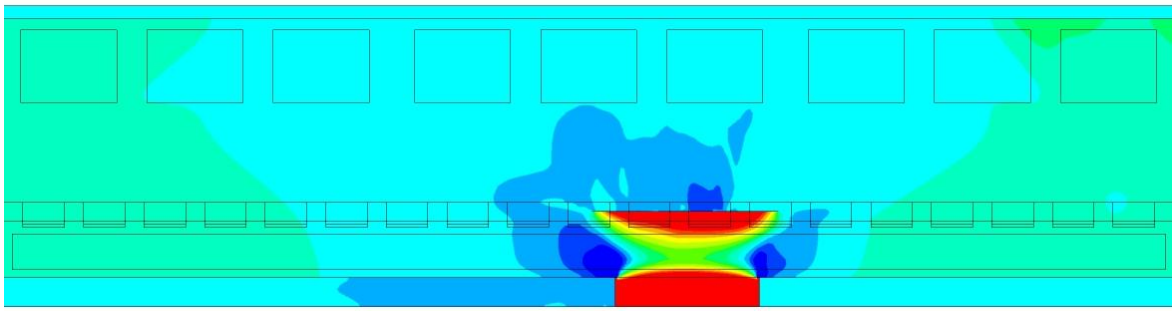

Figure 23 Chamber: pressure contours in the plenum region

With the purpose of understanding how the velocity field in the plenum region affects the fluid dynamic in chamber growing volume, the streamlines colored by velocity coming out from the air grilles are plotted.

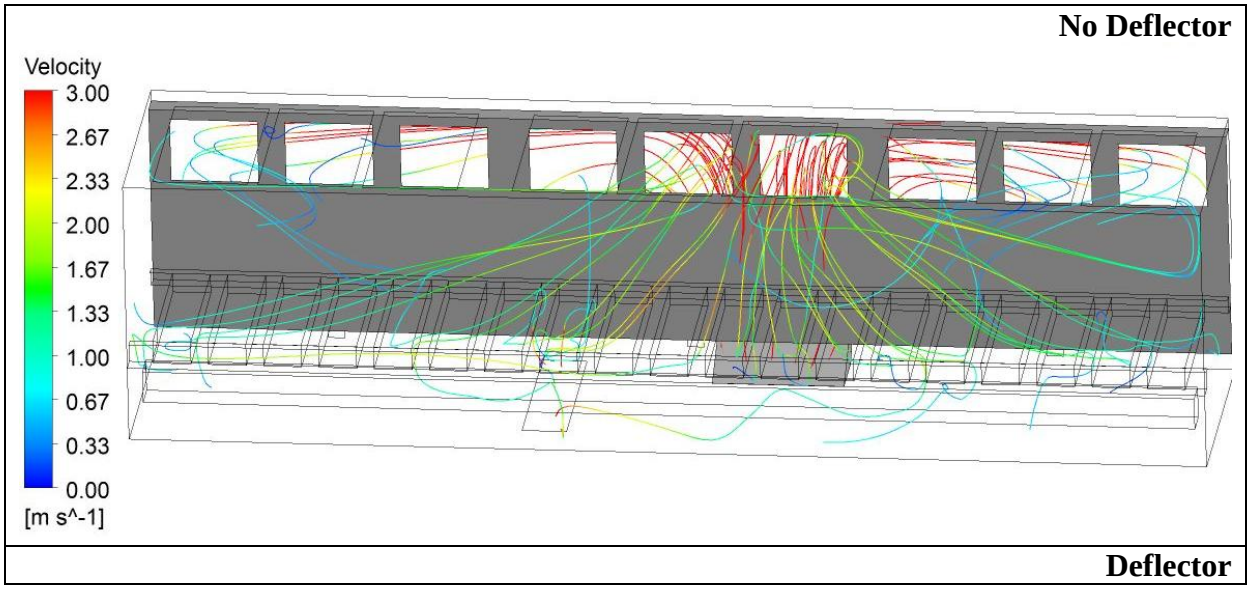

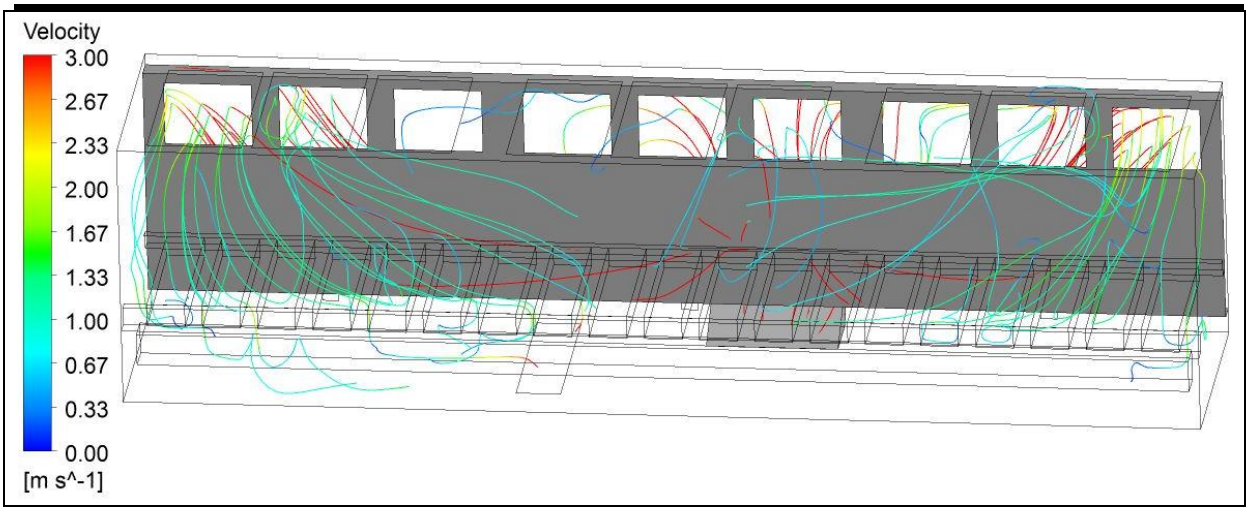

Figure 24 Chamber: streamlines

In Figure 25 and Figure 26, the velocity field in the chamber growing volume (and the plenum) is shown. At the air grille level the flow field distribution is completely different for both setups. In the vicinity of the trays, the flow pattern is more similar.

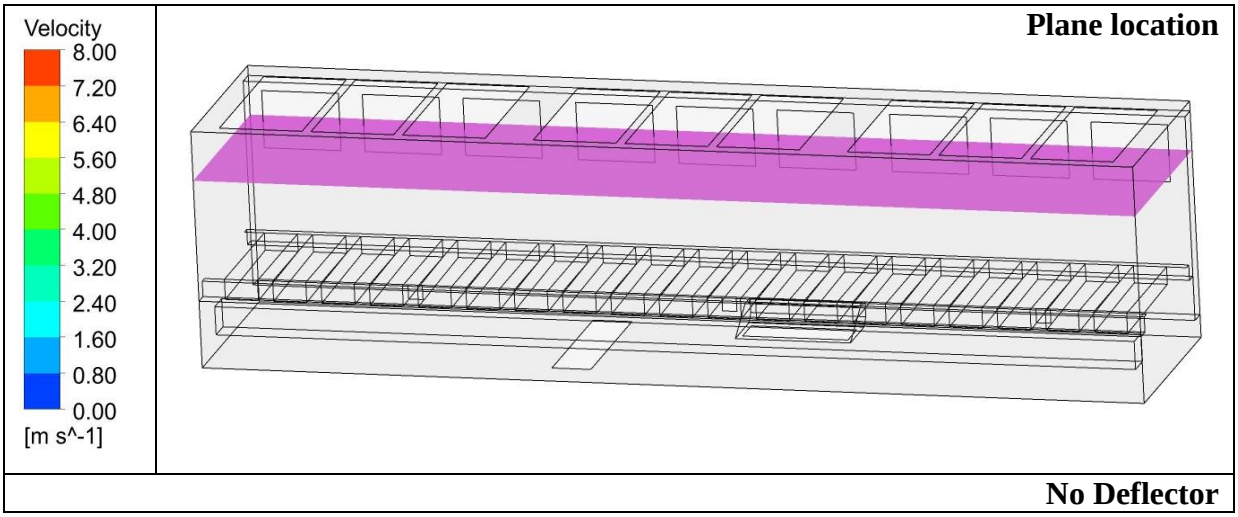

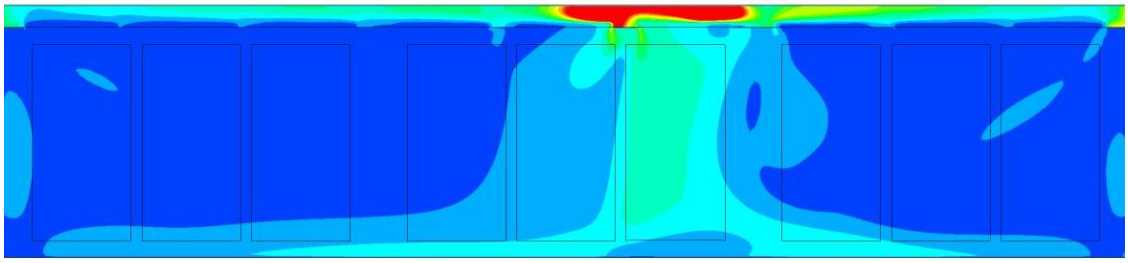

Deflector

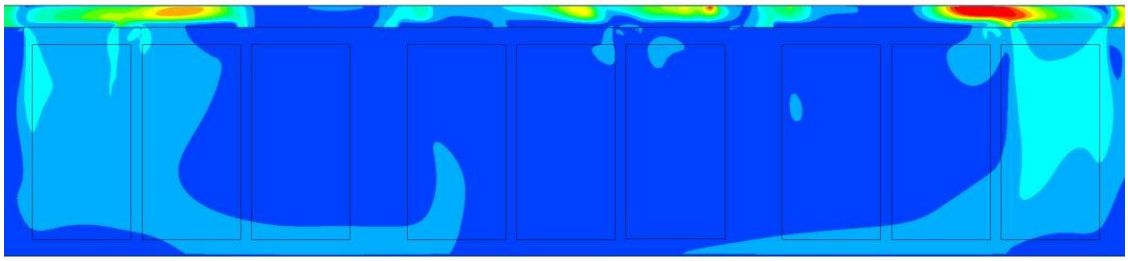

Figure 25 Chamber: velocity contour on a plane located 56cm above the top of the trays

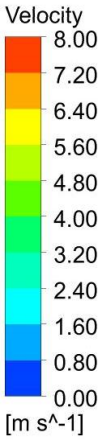

Plane location

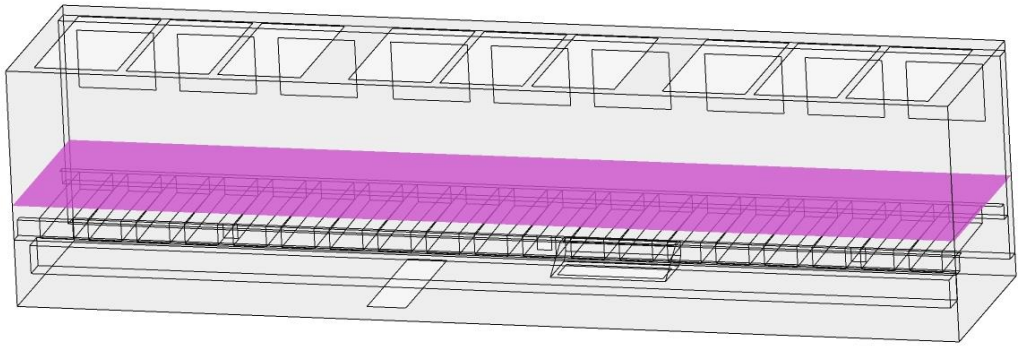

No Deflector

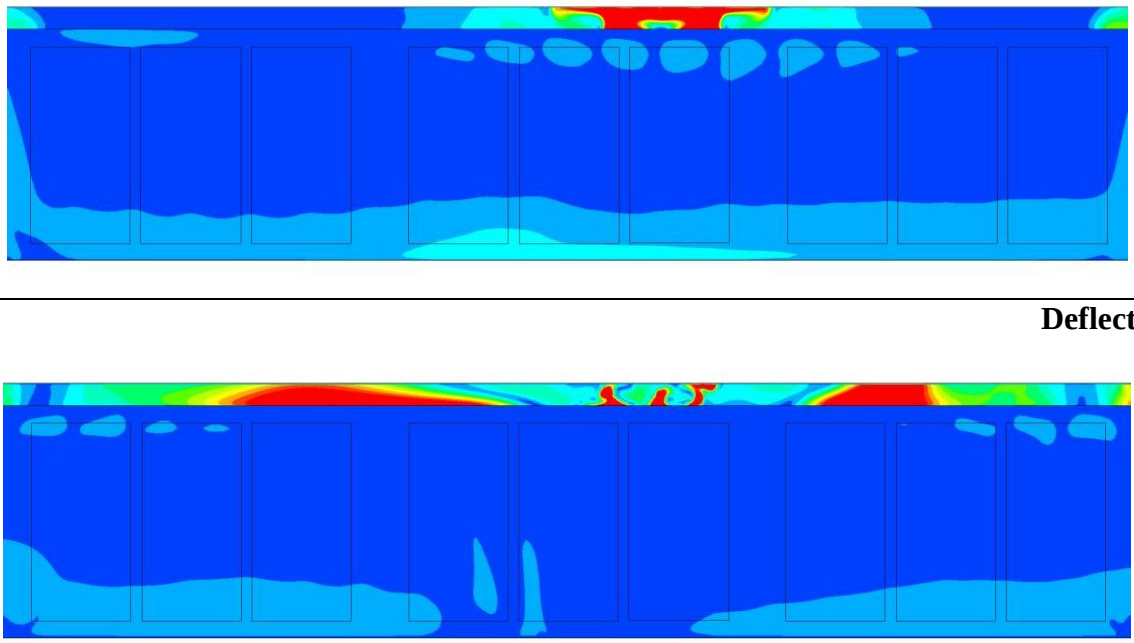

Figure 26 Chamber: velocity contour on a plane located 10cm above the top of the trays

In the following, the fluid dynamic performance of the chamber is analyzed in terms of flow rate distribution. Assuming that in the optimal scenario each air grille is responsible of feeding $1/9^{th}$ of air to the correspondent sub-region of the chamber, the objective should be balancing the flow distribution on the air grilles. A balanced air distribution results in an homogeneous air flow on the plants.

Figure 27 shows the name and the correspondent location of the air grilles.

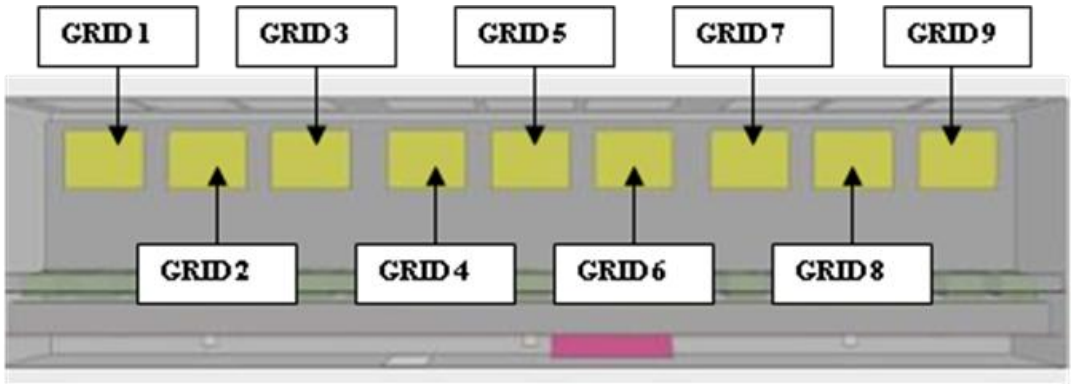

Figure 27 Chamber: location of the air grilles

Table 8 reports the flow rate and the percentage of air flow for each grille for both chamber configurations. Concerning the configuration without the deflector, it is evident that almost half of the total flow passes by GRID6. Together with GRID 5, 71% of the air flow is circulated.
The installation of the deflector mitigates this problem and even shifts the main flow towards both ends. Now the lateral grids (GRID1 and 9) are responsible for 60% of the total flow rate and there is no flow through GRID 3.

	GRID1	GRID2	GRID3	GRID4	GRID5	GRID6	GRID7	GRID8	GRID9
NO deflector									
Flow rate [Kg/s]	0.05	0.02	0.01	-0.01	0.17	0.34	0.04	0.02	0.07
Flow distribution %	6%	3%	2%	-1%	24%	**47%**	5%	3%	9%
Delta %	-5%	-8%	-9%	-12%	13%	**36%**	-6%	-9%	-2%
Deflector installed									
Flow rate [Kg/s]	0.22	0.14	0.00	0.02	0.02	0.05	0.00	0.06	0.23
Flow distribution %	**29%**	18%	0%	3%	3%	6%	-1%	9%	**31%**
Delta %	**18%**	7%	-11%	-9%	-8%	-5%	-12%	-2%	**20%**

Table 8 Flow rates comparison

An additional term called delta is included in Table 8. This term represents the difference between the calculated percentage and the target percentage which is about 11% (balanced flow). As expected the maximum delta is shown by GRID 6 in the configuration without the deflector.

In order to have a reliable index for the evaluation of the performance of the chamber in terms of flow balancing, the relative standard deviation (RSD) of the mass flow rate in the air grilles is calculated (see Table 9).

Mass Flow rate [Kg/s]	Mean	SD	RSD
No deflector	0.08	0.11	**139%**
Deflector	0.08	0.09	**110%**

Table 9 Relative standard deviation of Mass Flow rate in the air grilles

A lower RSD indicates a more uniform flow distribution which actually should induce a more homogeneous growth condition for the plants. With a relative standard deviation of 110% the configuration with the deflector installed shows a better performance.

By using the same approach applied to the flow rates, the velocity field in proximity of the trays is evaluated. Nine planes have been placed 0.11 m above the top of the trays in correspondence of each air grille. The planes locations are shown in the figure below.

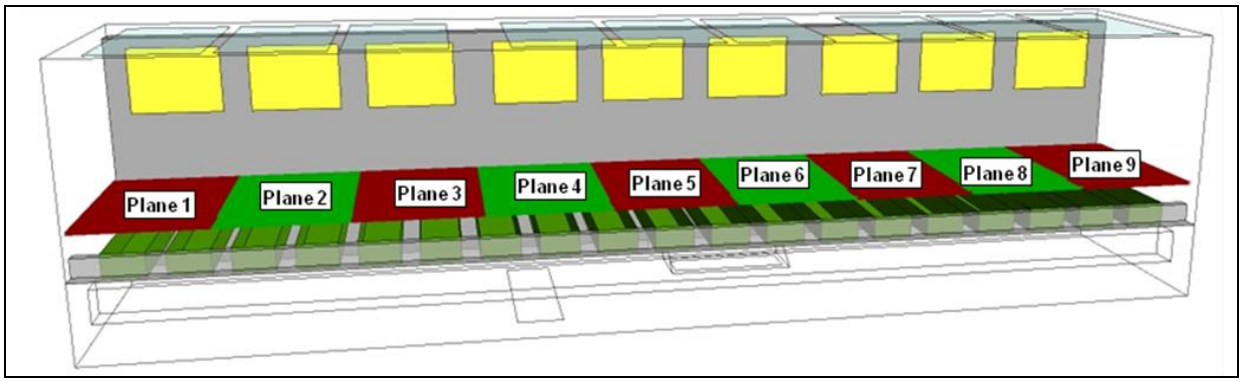

Figure 28 Chamber: location of the reference planes

As shown in Table 10, higher mean velocities are present on plane 6 and 7 of the configuration without the deflector. For this configuration, the mean velocity over all the planes is 11% higher if compared to the one with the deflector installed.
These indications are in agreement with the ones given by the flow rate distribution. The RSD calculated for the configuration without the deflector is two times the one with a deflector.

	PLANES									Mean	*Mean Difference*	*SD*	*RSD*
Velocity [m/s]	**1**	**2**	**3**	**4**	**5**	**6**	**7**	**8**	**9**				
No Deflector	0.587	0.510	0.459	0.489	0.585	**0.754**	**0.746**	0.546	0.560	*0.582*	*+11%*	*0.104*	***18%***
Deflector	0.538	0.501	0.522	0.563	0.491	0.442	0.476	0.589	0.526	*0.516*	*-11%*	*0.045*	***9%***

Table 10 Velocities and RSDs comparisons

Velocity results confirm that the flow distribution is more uniform in the configuration with the deflector installed. However, the deflector design could be further improved/optimized. As clearly shown in Figure 23, the pressure drop induced by the deflector is too high as well as the deflection of the flow in the direction of the lateral grids 1 and 9 (see Table 8). In order to

downsize the flow rates in the lateral grids and minimize the downstream shadow zone, the constriction of the flow area due to the presence of the deflector should be reduced.

1.6.2. HVAC

The flow field characteristics in the HVAC domain are herein assessed via CFD simulation.

Figure 29 and Figure 30 show the pressure and the velocity contours on two orthogonal planes. The pressure drop in the water coils is clearly visible as well as the influence of the blower.

Figure 31 displays the streamlines colored by pressure and velocity. Recirculation regions are located upstream of the cooler and in proximity of the blower.

Figure 32 highlights the critical region of the flow field located at the entrance of the HVAC. The presence of a strict elbow forces the flow to turn abruptly before passing through the water coils and generates a shadow area close to the topside of the cooler. High pressure values are present above the blower where the flow runs into the cooler and the air stagnates in the upper part of the cooler.

Observing Figure 33 and Table 11 it can be stated that:

- As a consequence of the phenomenon illustrated in Figure 32, the velocity profiles at the entrance and at the exit of the cooler are not uniform.
- The relative standard deviations (RSDs) of the velocities at the entrance of the cooler is high (17%).
- The uneven flow distribution is mitigated passing through the cooler. The RSD shifts from 17% to 11%.
- The flow distribution is almost uniform in the heater region. The RSD is close to 4% both at the entrance and at the exit of this device.

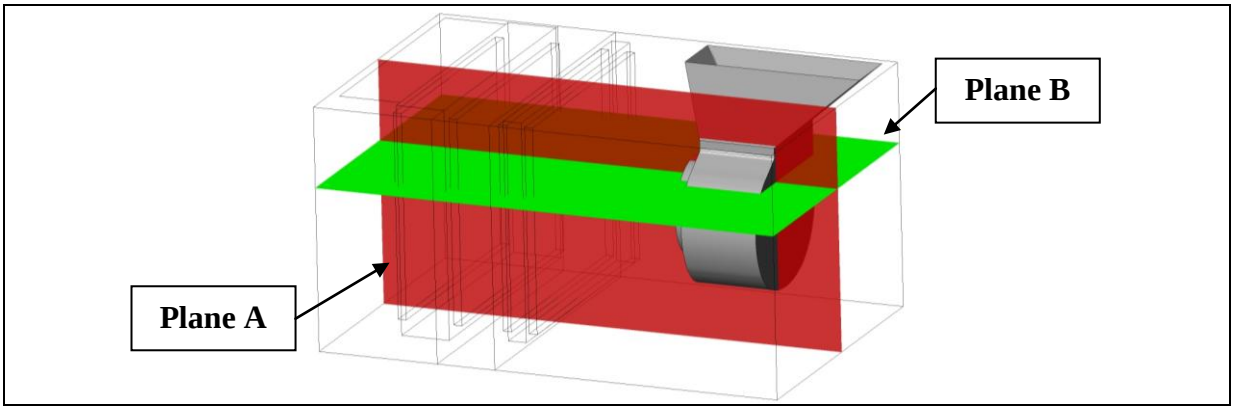

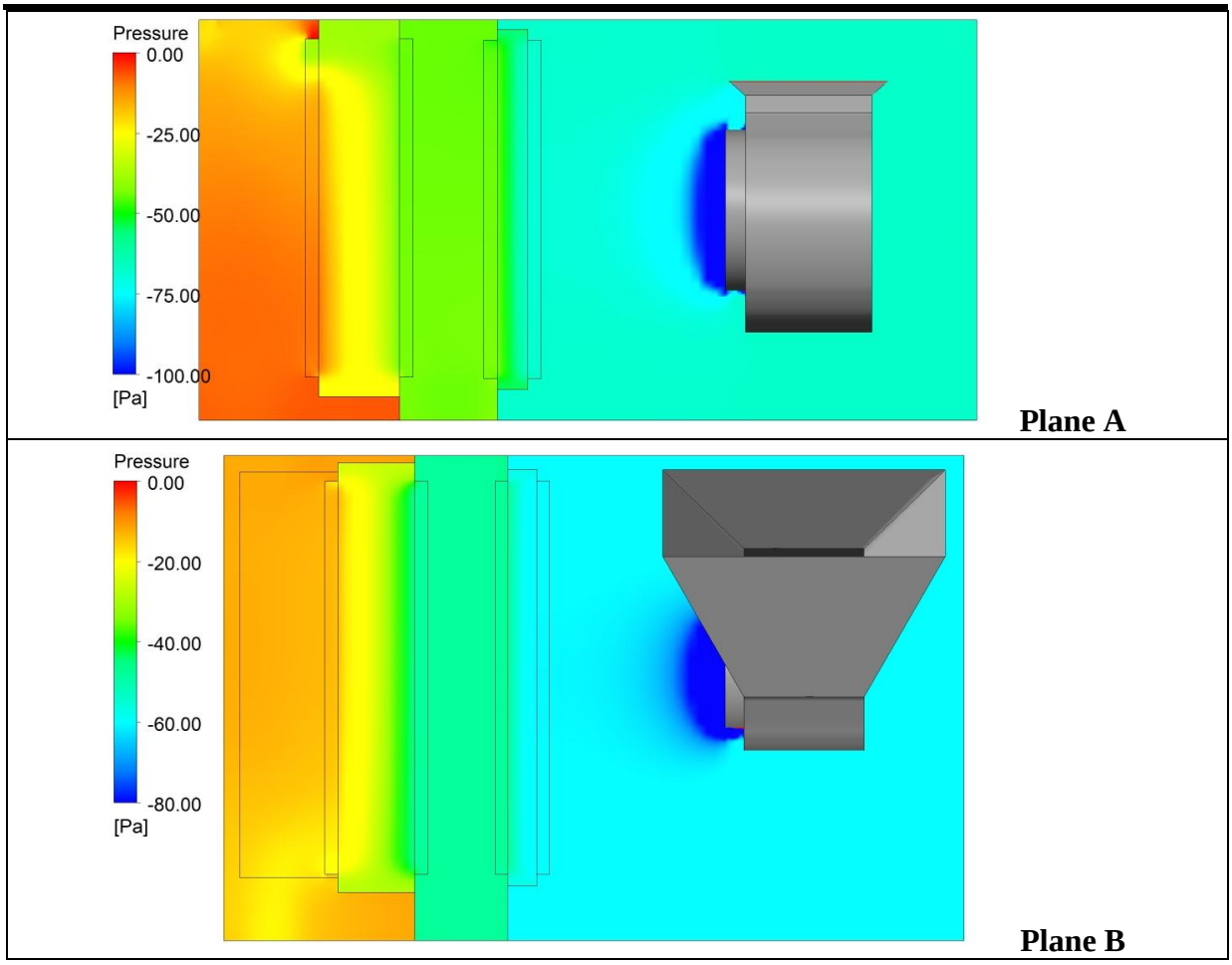

Figure 29 HVAC: pressure distribution

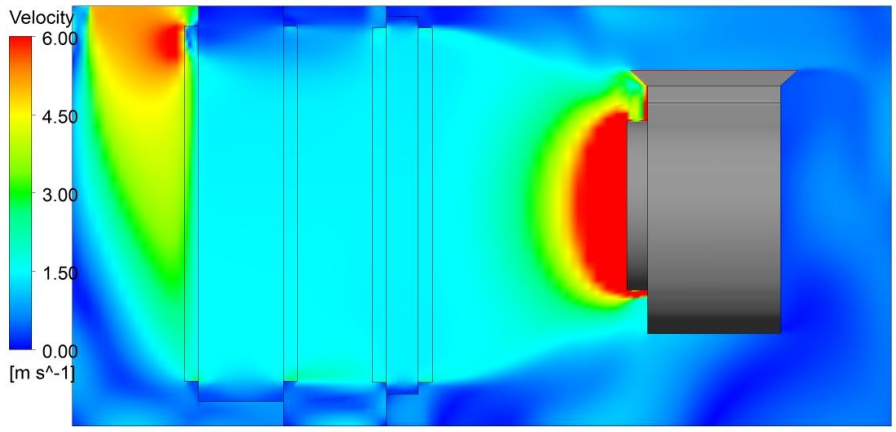

Plane A

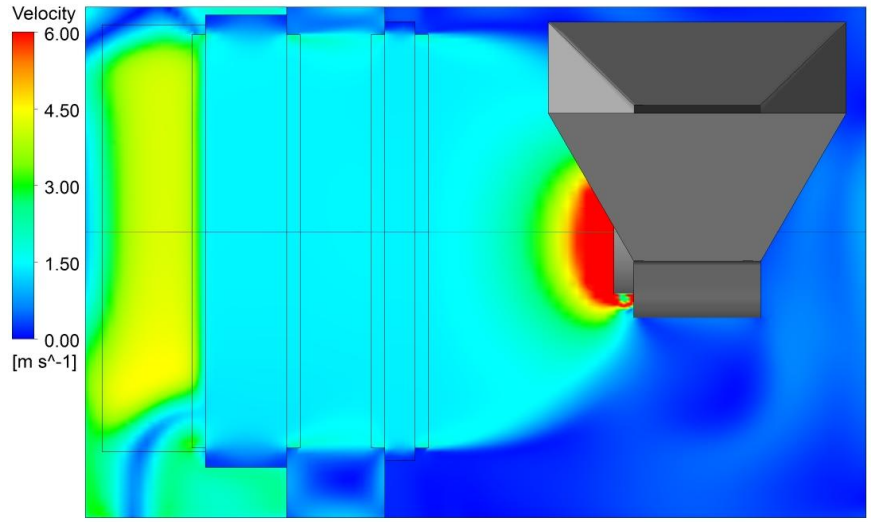

Plane B

Figure 30 HVAC: velocity distribution

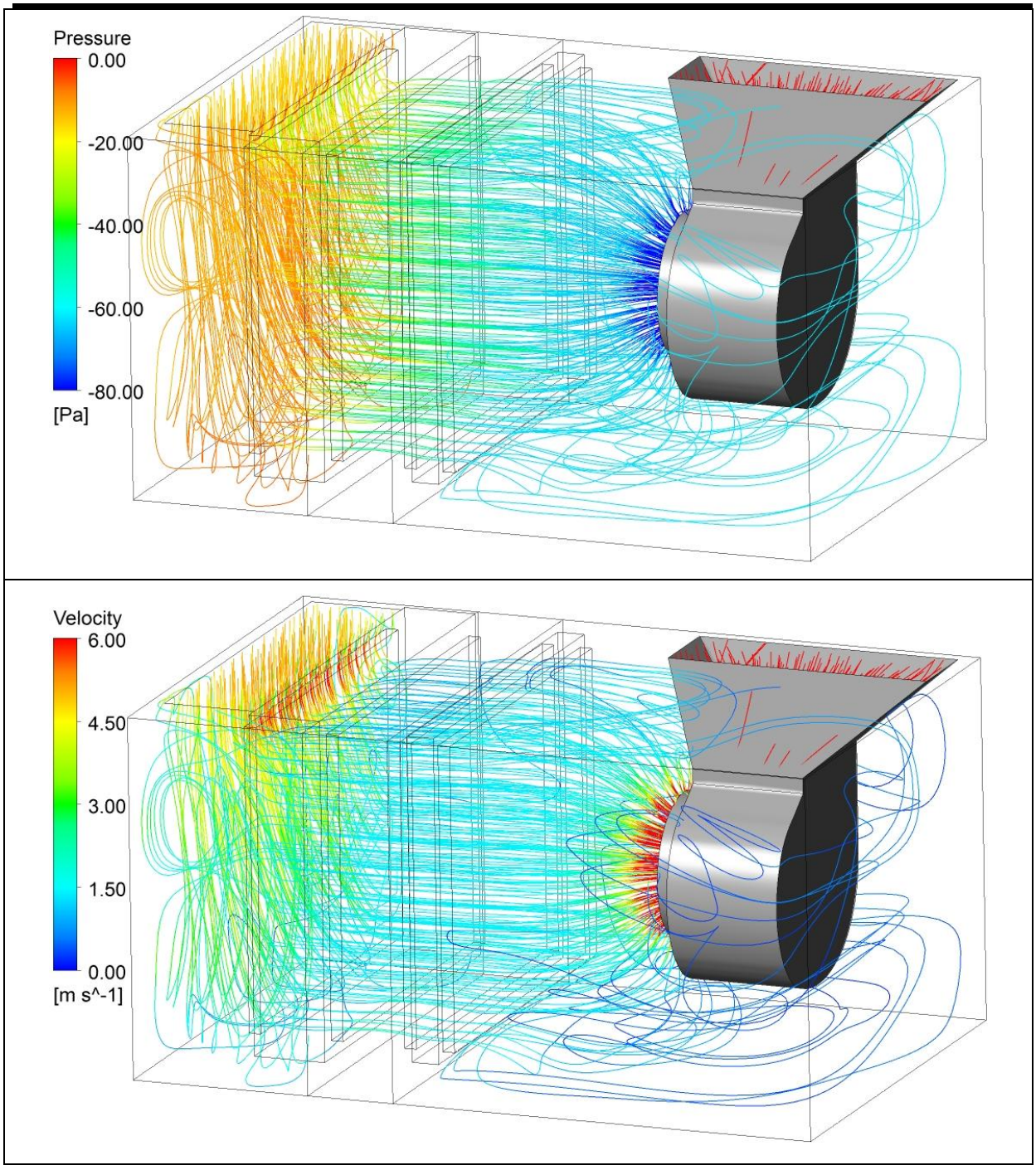

Figure 31 HVAC: streamlines

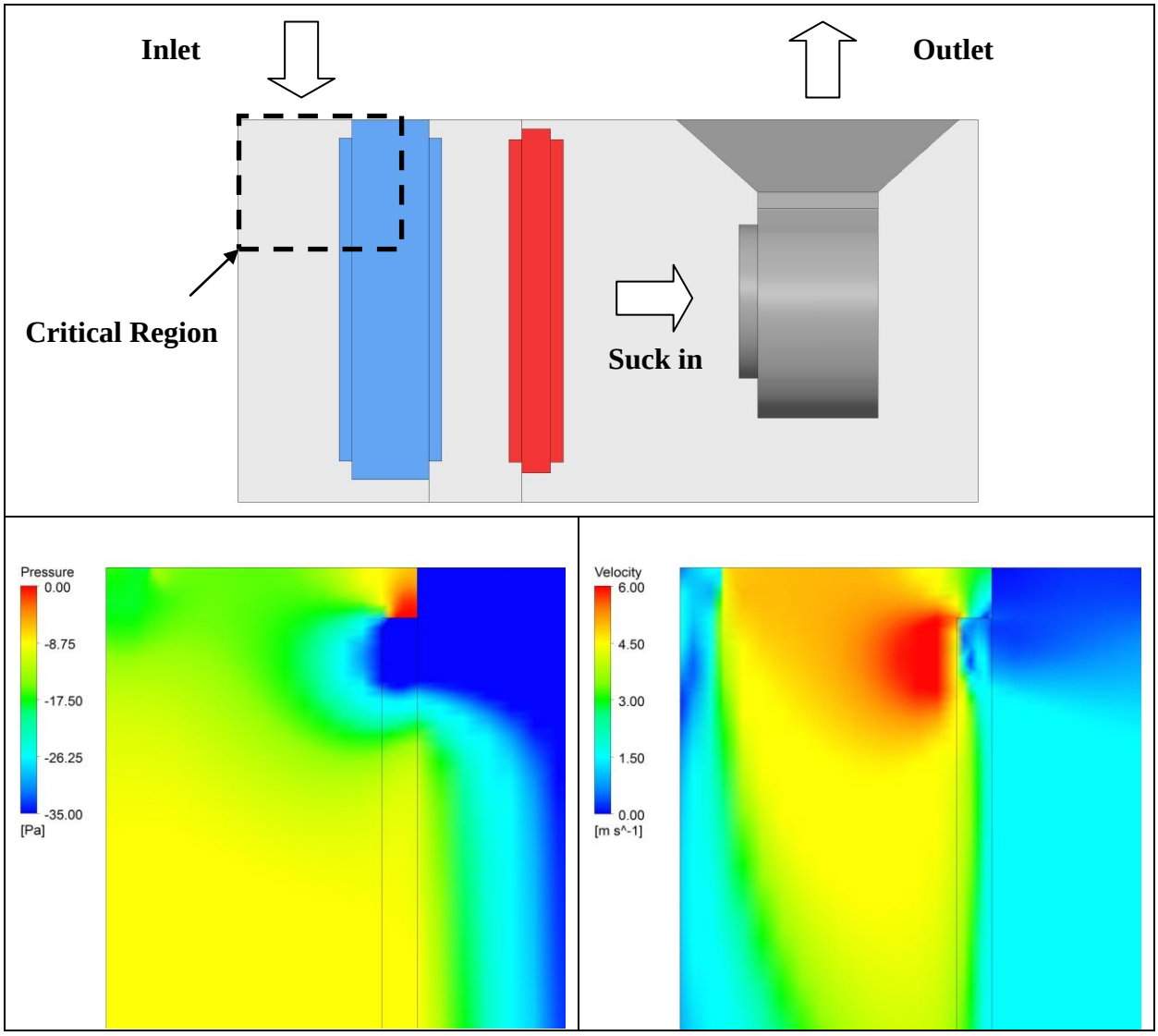

Figure 32 HVAC Critical Region: pressure and velocity magnitude

Velocity	DEV.ST	MEAN	RSD
Cooler IN	0.246	1.456	17%
Cooler OUT	0.156	1.380	11%
Hot IN	0.058	1.403	4%
Hot OUT	0.053	1.384	4%

Table 11 Mean and RSD of the velocities at the entrance and the exit of the heating coils

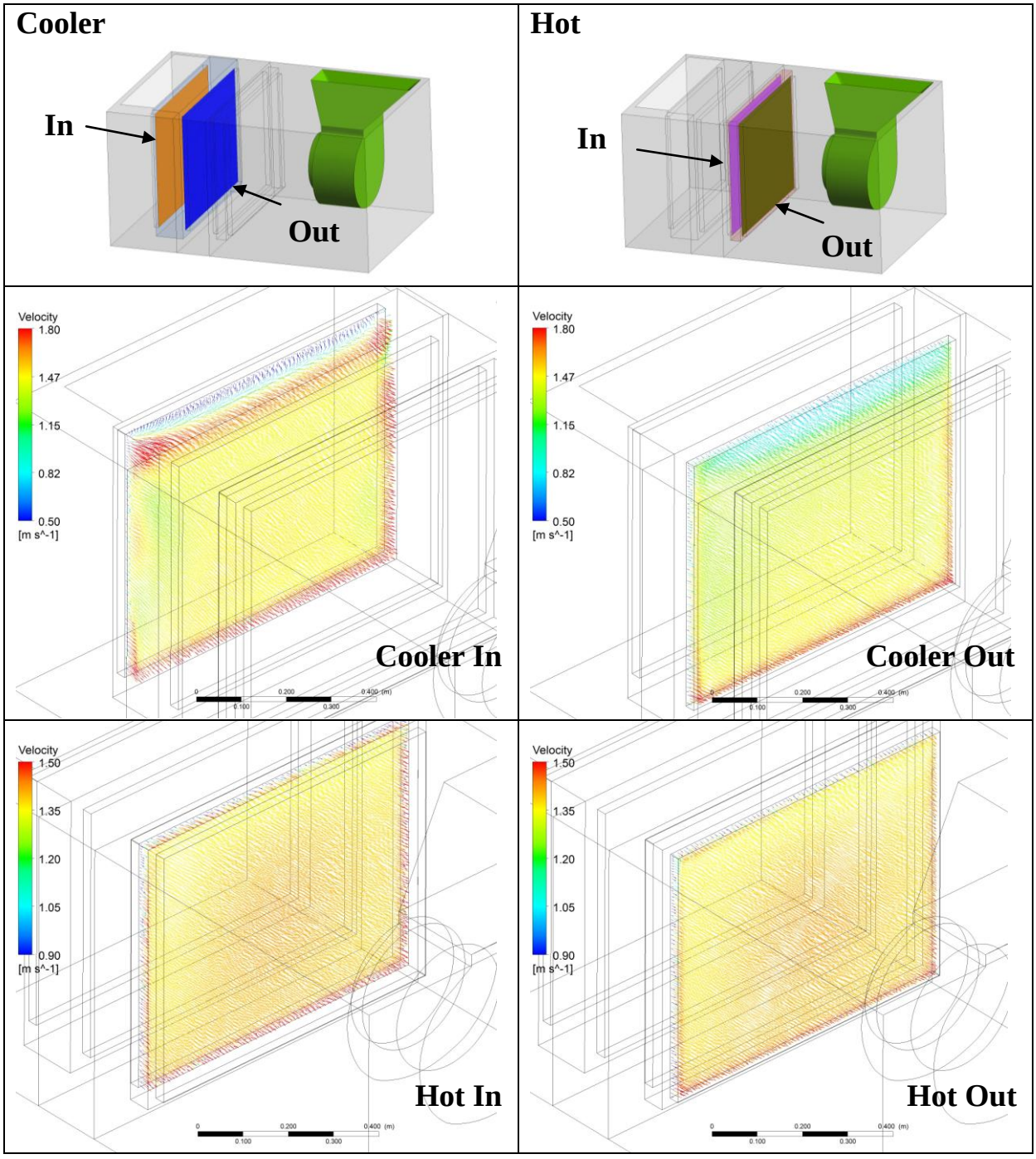

Figure 33 HVAC: velocity vectors

1.6.3. Lights

Computational fluid dynamics coupled with the radiant transport equation was used to assess the airflow circulation, to evaluate the temperature distribution in the loft and to obtain the light incident radiative flux at the boundaries in the glass regions.

Figure 34 reveals the details of the flow field within the loft by means of the velocity streamlines. In reason of the geometrical (inlet and outlet mutual position) and the physical parameters (mass flow at the inlet), recirculation areas are inevitably present in the light loft.

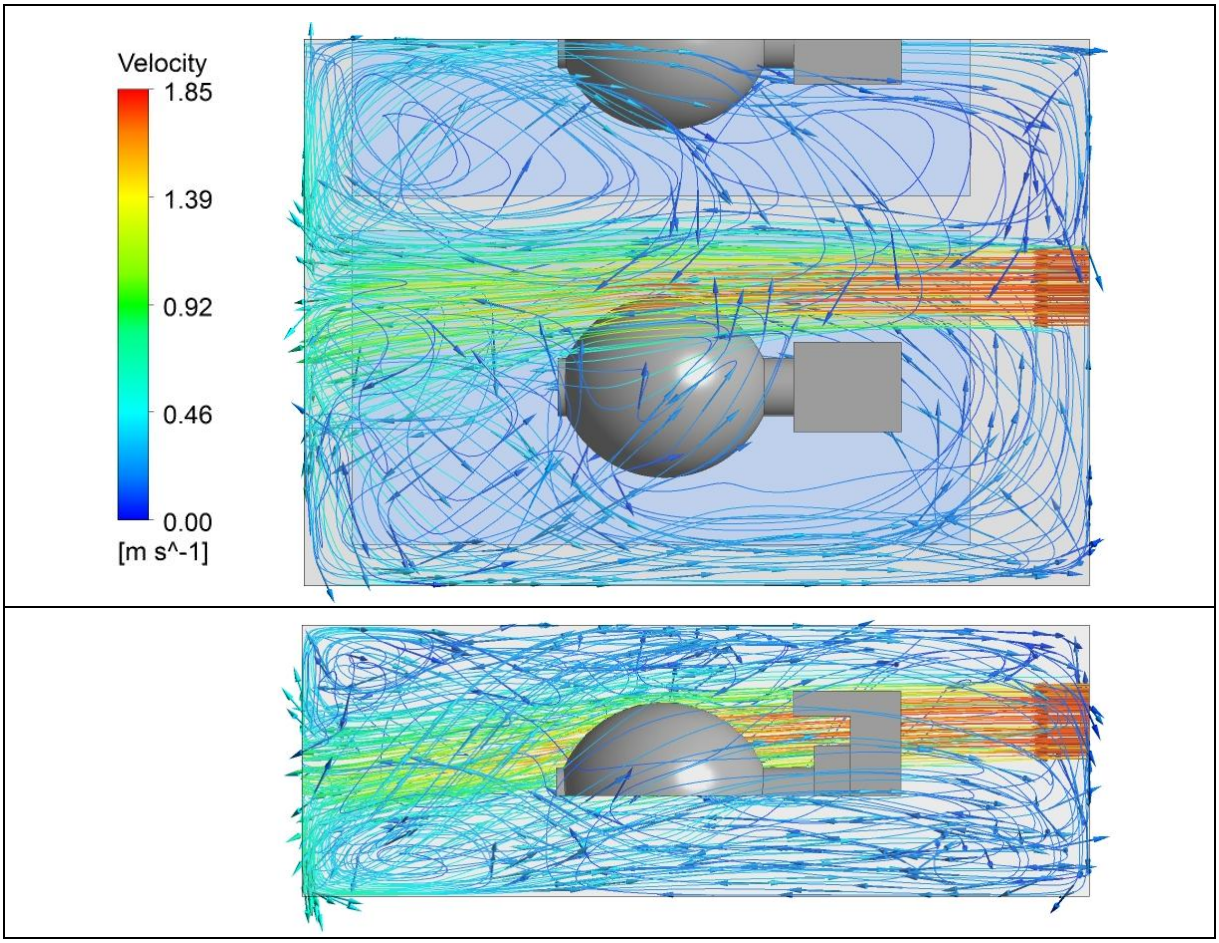

Figure 34 Lights: streamlines

Figure 35 and Figure 36 illustrates the temperature field. It is evident, that:

- The heat released from the bulbs is responsible for the air temperature rise
- The maximum temperature regions are located close to the reflectors
- The temperature rise is higher for the HPS lamp
- The recirculation areas highlighted in Figure 34 greatly influence the temperature field in the loft. Higher air temperature are noticed in back of the loft where air velocities are

close to zero

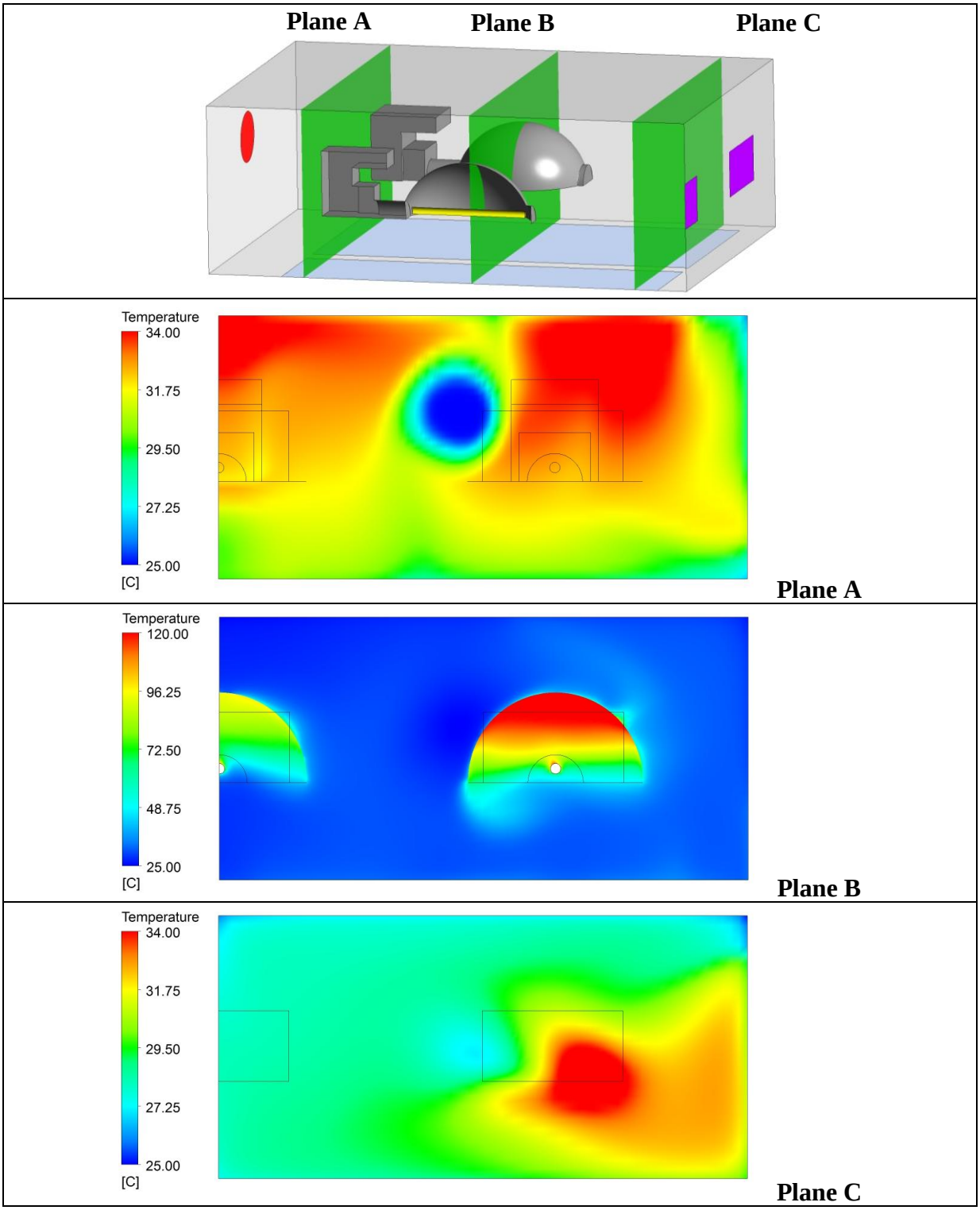

Figure 35 Lights: temperature distribution on longitudinal planes

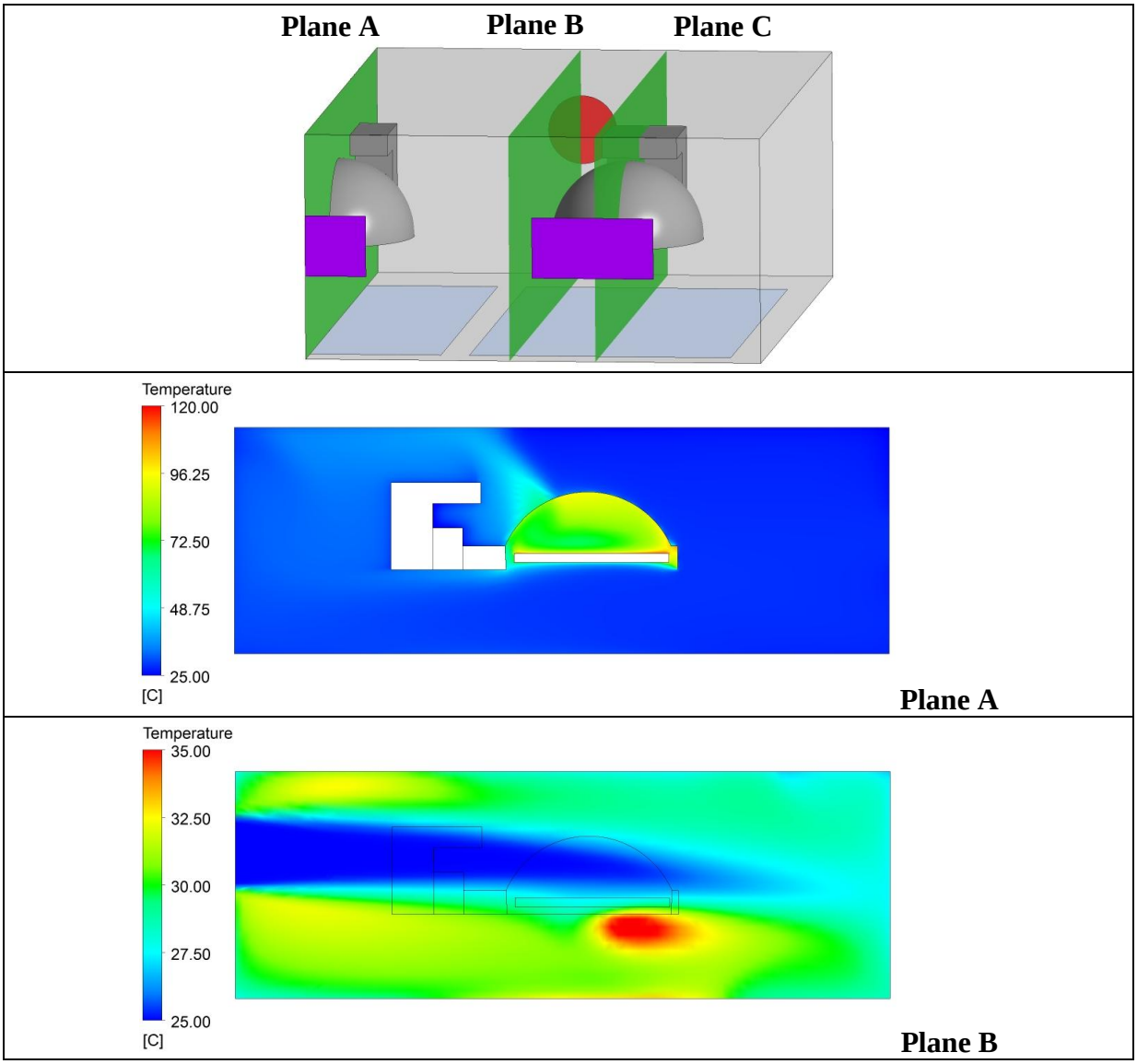

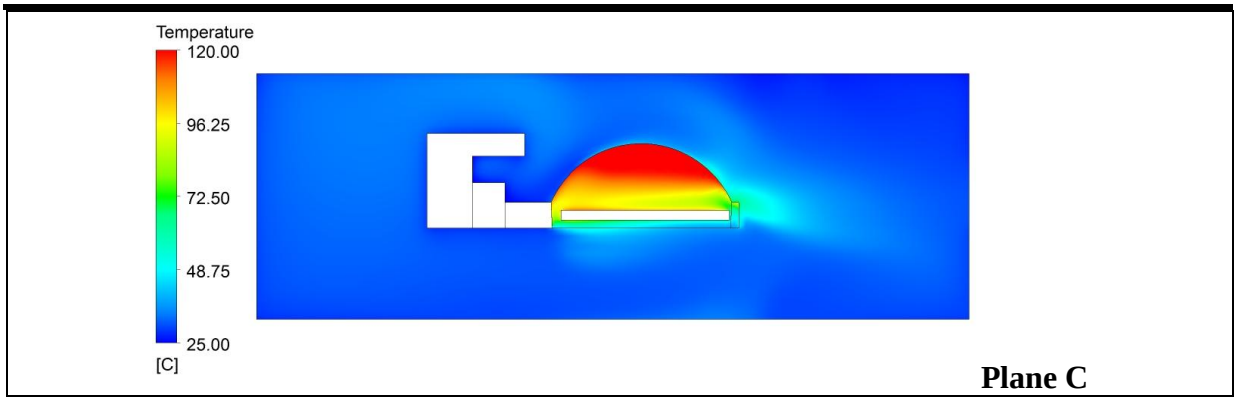

Figure 36 Lights: temperature distribution on transversal planes

The electromagnetic radiation in the visible range is a key factor for plant life since visible light allows photosynthesis to take place. Hence the importance of characterizing this spectral region which, as mentioned in paragraph 1.4.3, was discretized by using three bands.

Figure 37 shows the distribution of the irradiation flux at the glass surface for each band.

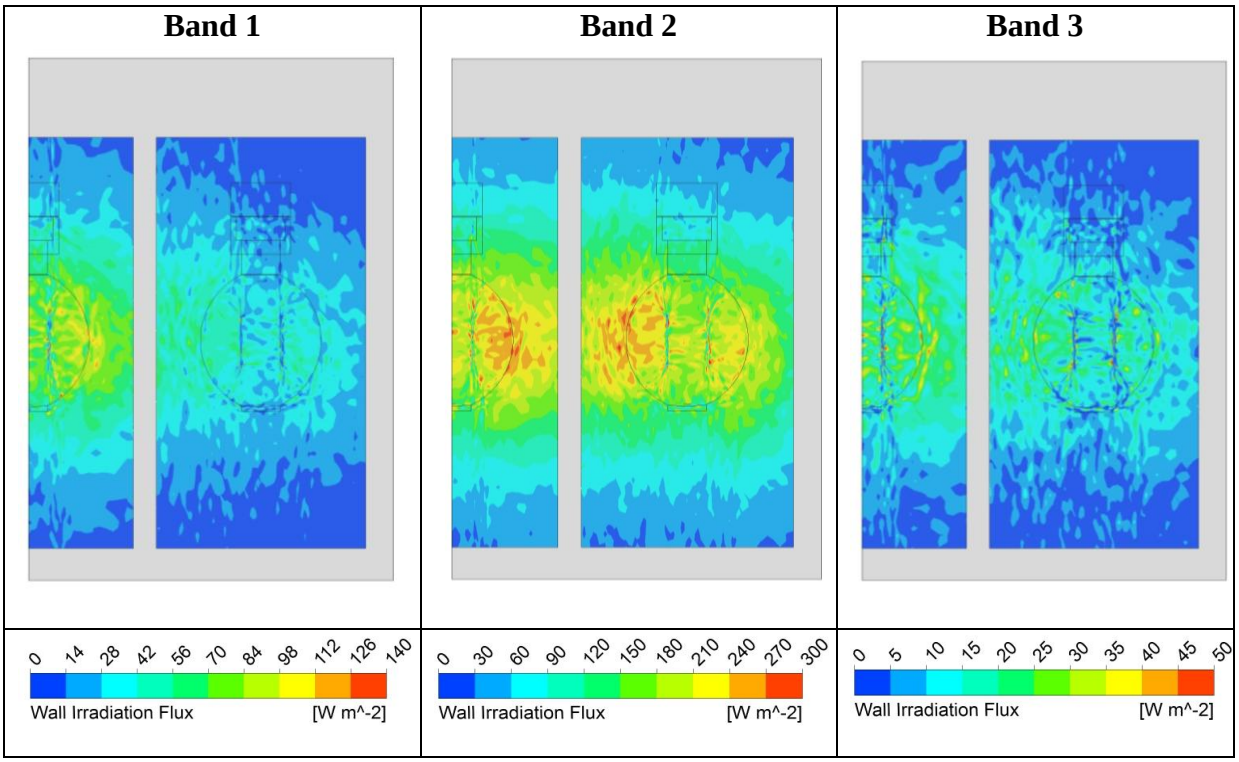

Figure 37 Lights: wall irradiation fluxes at the glass surface

From the distributions highlighted in the figure above, the following considerations can be made:

Band 1 (from 380 to 510 nm): The contribution to this band is higher for the MH lamp than for the HPS lamp

Band 2 (from 510 to 650 nm): It is the most energetic band in the visible range. The central region of the glasses reach values of up to 300 [W m^{-2}] for both the types of lamps.

Band 3 (from 650 to 780 nm): This is a low energy band. The wall irradiation flux distribution is almost the same for both types of lamps.

Figure 38 shows the trend of the wall irradiation flux for measurement points placed on the diagonal of the glasses. As previously pointed out, the energetic contribution to Band 1 is sensibly different for the two types of lamps.

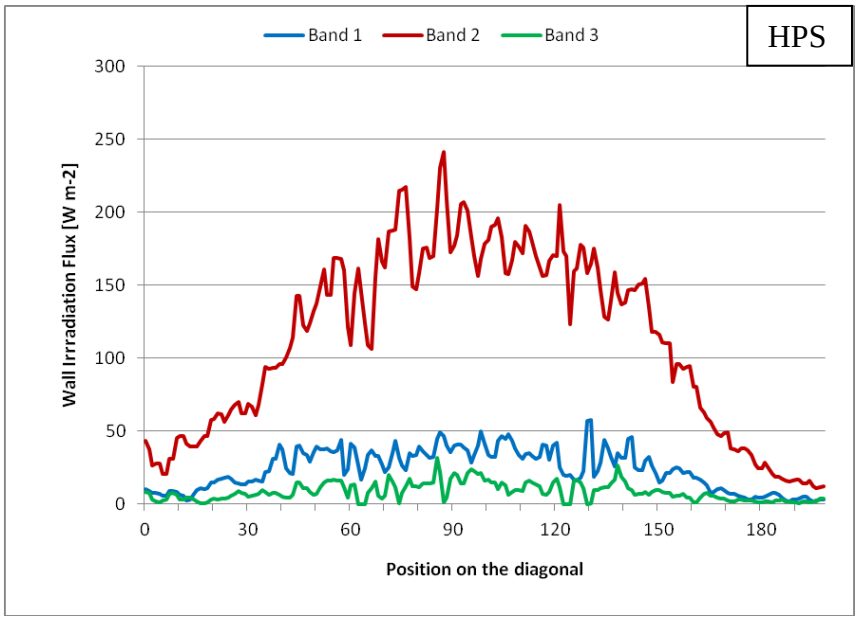

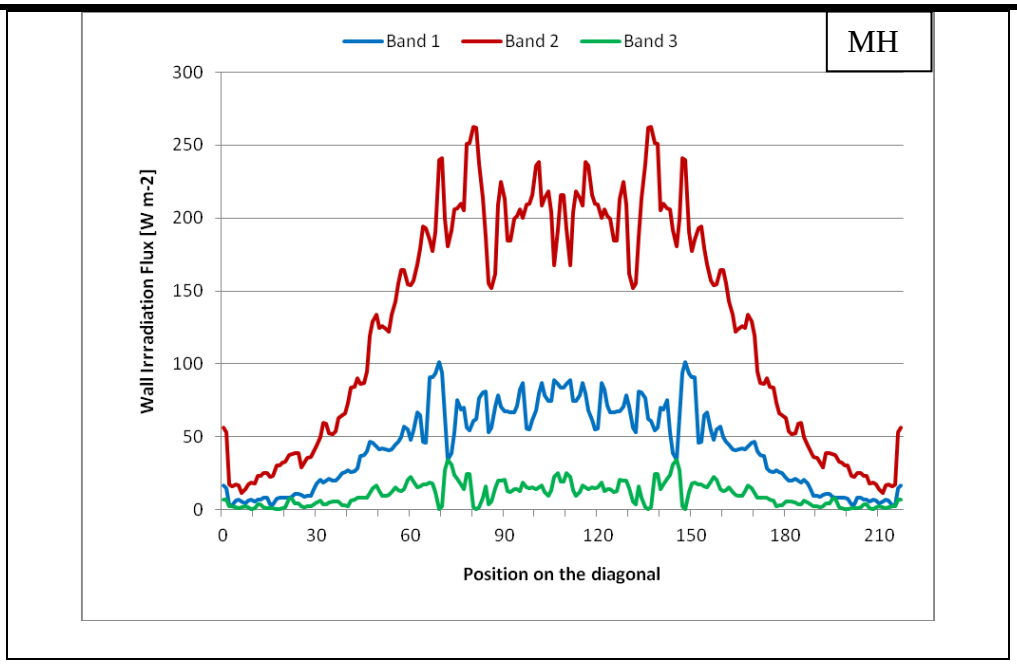

Figure 38 Lights: wall irradiation flux on the diagonal of the glasses

1.7. Conclusions

The CFD simulations carried out on the High Plant Compartment allowed the investigation of the fluid dynamic performance of the system in the absence of the plants.

The analysis of the results shows that:

Chamber

- The flow distribution in the chamber is highly unbalanced for both the configurations under investigation
- As a consequence of the unbalanced flow distribution, the chamber suffers of a degree of environmental parameters heterogeneity
- Since the variation in concentration of oxygen and carbon dioxide introduced by the plant metabolism are very small, the convective flow is the dominant physical aspect. A balanced air flow should result in a homogeneous distribution of the gas concentrations. Hence an unbalanced flow field is also expected with the plant introduction.
- Adding a deflector in the plenum region positively affects the flow rate distribution and results in more uniform velocity maps in proximity of the trays.
- The design of the deflector needs to be optimized since the actual design implies a resistance to the flow which is too high.

HVAC

- The presence of the elbow at the inlet of the chilling coils is responsible for the loss in the heat transfer performance. The air cannot enter uniformly and results in a turbulent and uneven flow distribution at the face of the coils.

- In order to reduce the loss in the heat transfer performance, the connection to the inlet of the chilling coils should be properly designed to provide flow conditions more uniformity and straighter flow.

Lights

- The airflow circulation in the loft is not optimized to facilitate the heat disposal.
- The position and the number of fans with could be improved.

2. Basic wet model and Advanced canopy submodel (step2)

The analysis of the plant growth chamber fluid-dynamic behavior is an important tool to achieve a deeper understanding of the environmental factor fields and thus guide the set up of the chamber control system by indicating the suitable technical specifics of the probes and identifying the optimal position for measurements.

Plant modeling is a fundamental issue to characterize the environment. Plants interact with the environment (growth chamber) by exchanging water and energy. Within step 2 of task 3220, plant evaporative load is added into the growth chamber model. Currently two approaches are used:

The first approach, called Baseline wet model, integrates evapotranspiration, carbon dioxide assimilation and oxygen production by the use of empirically fitted figures derived from the experimental data provided by UoGuelph. It is a straight approach to the plant modeling problem where plants act as sources of water vapor and O_2 and sinks of CO_2. The goal is to generate maps of the environmental factors and thus characterize parameter heterogeneity that induces undesirable non–homogenous plant growth and composition. All hypotheses made for modeling are presented and explained in this document.

The second approach, named Advanced Canopy sub model, is based on mechanistic laws. Unlike the baseline model where the exchange of the physical parameters is imposed as a fixed

boundary condition to the problem, the Advanced model establish the interaction between the plant and the environment. The link is guarantee by a mathematical law which has the form of the Penman-Monteith equation and which is implemented via CFD code syntax.

The software ICEM-CFD and ANSYS-CFX have been used to construct the geometry of the growth chamber and to execute the CFD analyses.

2.1. Acquired data

The evapotranspiration model and the boundary conditions for the fluid-dynamic analysis were derived from data supplied by UCL.

Document	Date	Origin	Type of data
email	15/07/2009	UCL, Louvain	Effect Wind on Transpiration Young trees.pdf Workingdoc_08jul09_transpiration.doc
email	31/07/2009	UCL, Louvain	Evapotranspiration Data.xls
email	13/08/2009	UCL, Louvain	Evapotranspiration Data Update.xls

Table 12 Acquired data

Further details about the transpiration model were directly discussed with Laury Chaerle from UGent and Heather Maclean from UCL.

2.2. Basic wet model

2.2.1. Geometry and computational grid

The geometry and the computational grid used for the present simulation are the same described for the dry model (step1).

2.2.2. Physical properties and boundary conditions

The fluid domain has been set as follows:

- Fluid: gas mixture
- Energy: thermal energy
- Buoyancy: enabled
- Turbulence: k ε model with scalable functions at walls

In the fluid domain the following boundary conditions have been set:

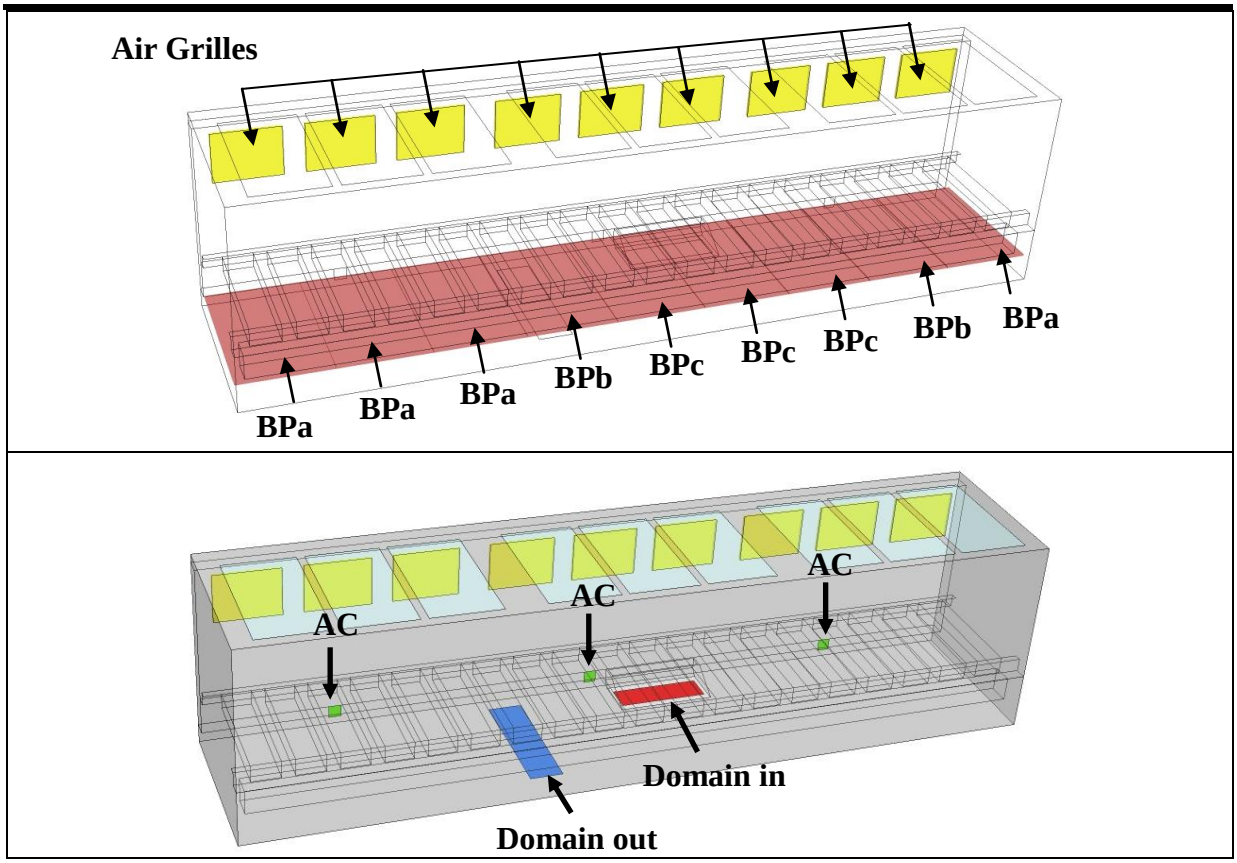

Figure 39 Chamber boundary condition locations

Domain In: A flow rate of 0.84[Kg s^{-1}] has been set at the entrance of the chamber. Since the HVAC is supposed to supply air in optimal and constant conditions, the target value of temperature (25[°C]) and mass fraction are imposed to the gas mixture directed into the chamber. Table 13 shows the target values of mass fraction for the gas mixture.

Mixture component	Mass fraction
Water Vapor	0.0137 (RH 70%)
O_2	0.2289
CO_2	0.001

Table 13 Mixture target mass fractions

Domain Out: below the tray support and in proximity of the chamber mid-plane, there is a rectangular opening which allows the communication between the chamber and the HVAC domain. At this location, an outlet boundary condition has been set with an average static pressure of 0[Pa]

Atmospheric Control (AC): the Teflon bags managing the atmospheric pressure in the chamber are modeled as openings where the atmospheric pressure is imposed. At the openings, when the pressure level is lower than the atmospheric one, the flow enter the domain. Otherwise the flow is directed out of the chamber. This behavior is in agreement with the real one.

Balancing Panels (BP) and Air Grilles: for the boundary details see chapter 1.4.

HPC and Trays: a wall boundary condition has been imposed on the HPC and on the trays. For both of them a no slip option has been used for modeling the influence of the wall boundary on mass and momentum. Moreover both are treated as adiabatic.

Plant: the plant boundary is the collection of the surfaces placed at the top of the trays. As highlighted in Figure 1B, the evapotranspiration phenomena and the photosynthetic response are modeled with a source for water vapor and O_2 and a sink for CO_2.

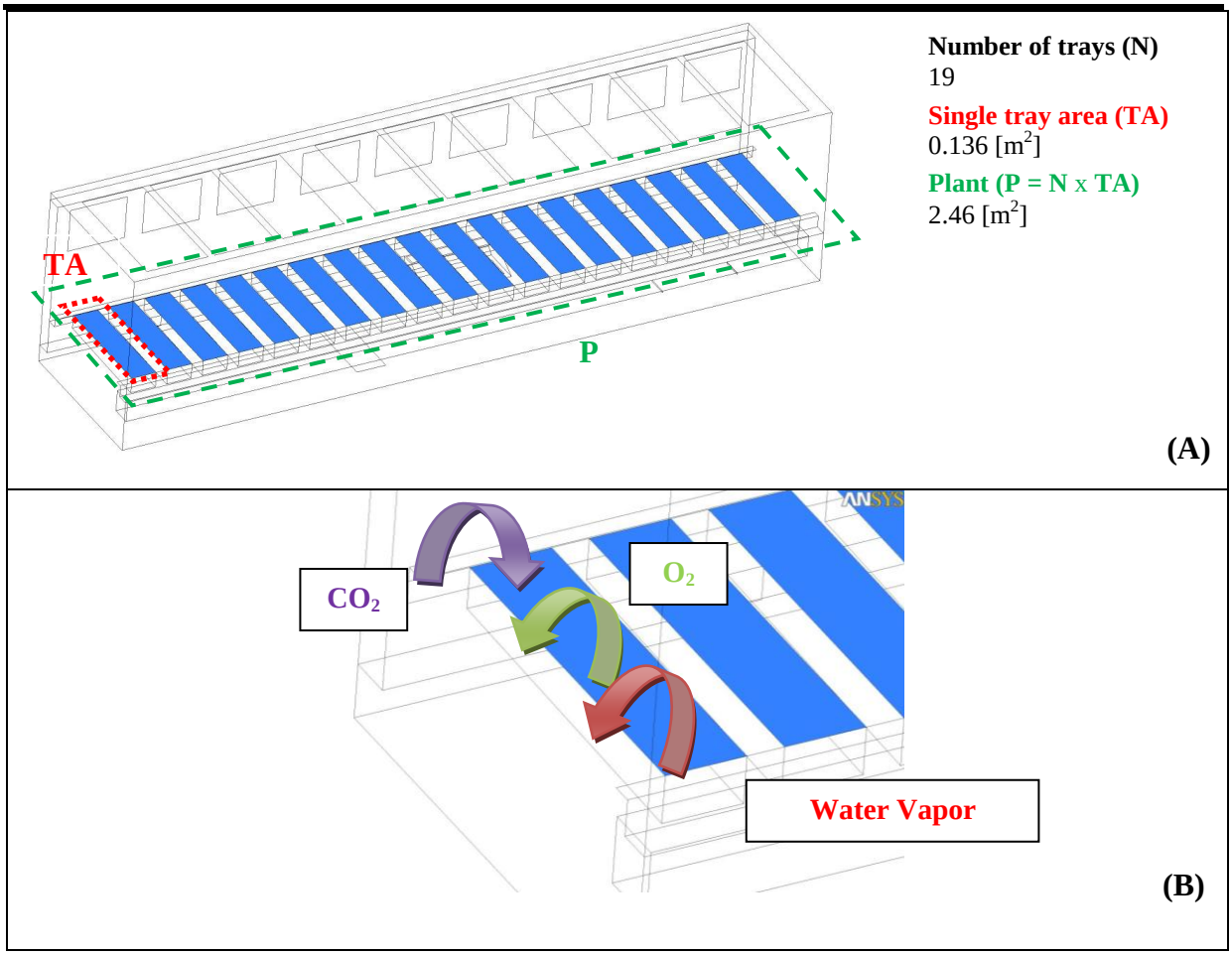

Figure 40 Schematic of the chamber geometry

The imposed daily rates are derived from the experimental data provided by UoGuelph and are uniformly distributed over the plant boundary. It is important to notice that the growth surface area is the same for the CFD model and the chamber where the experimental measurements were performed.

The values of the daily rates for the data set under investigation are shown in Table 14.

Days in Chamber	Evapotranspiration rate (kg H2O/d)	CO2 uptake rate (kgCO2/d)	O2 production rate (kg O2/d)
1	4.61041802	0.007222587	0.00146726
2	8.054206969	0.006875898	0.00139683

3	8.375793031	0.009692996	0.001969121
4	8.680526639	0.011873718	0.002412132
5	8.675786887	0.014588976	0.002963733
6	8.764346309	0.019303298	0.003921442
7	9.29368033	0.016285	0.003308278
8	10.23157992	0.028542329	0.00579834
9	**11.08671311**	**0.038110887**	**0.007742181**
10	12.40526639	0.047207306	0.009590108
11	13.09434016	0.059231194	0.012032746
12	14.9601332	0.070552381	0.014332632
13	15.345	0.064760673	0.013156053
14	15.54687089	0.100702822	0.020457658
15	18.86997542	0.109244408	0.022192871
16	19.05920697	0.101892126	0.020699264
17	19.21684016	0.129312806	0.026269742
18	18.98592008	0.142051955	0.028857685
19	17.75065984	0.11522922	0.023408679
20	20.305	0.151604641	0.030798302
21	20.85171311	0.121661768	0.024715443
22	24.79684016	0.14440501	0.029335705
23	27.98223975	0.159741783	0.032451352
24	28.51789344	0.164544593	0.033427038
25	28.90802664	0.171395373	0.034818765
26	29.61079303	0.172529006	0.035049062
27	28.35920697	0.133109773	0.027041092
28	32.23894672	0.166185303	0.033760346
29	33.48737295	0.154303094	0.031346489
30	**33.3998668**	**0.120181843**	**0.024414798**
31	34.255	0.163335567	0.033181426
32	34.79855328	0.164315001	0.033380396
33	35.6473668	0.167706474	0.03406937
34	35.27303278	0.167650803	0.034058061
35	34.55762705	0.167828875	0.034094236

Table 14 Lettuce data set (GW0704)

The conservation of the internal energy requires the introduction of an energy source due to phase change at the plants surface. The absorbed energy is equal to the product of the water vapor flow rate and the water latent heat for evaporation.

The timescale of the physical phenomena under investigation (evapotranspiration and photosynthetic response) is several orders of magnitude smaller than the time scale of the data acquisition. Due to this time scale difference, the phenomenon can be regarded as steady and the analysis can be performed at given instants. Hence two instants were examined. The first instant (day9) was chosen sufficiently far from day1 in order to have significant flow rate values. The second instant (day30) was selected so to have at least three times the evapotranspiration rate of the first instant and to avoid time border effects.

The same initial conditions are used for both steady state analyses:

- Relative humidity 70%
- Carbon dioxide mass fraction 0.0015
- Oxygen mass fraction 0.2289
- Air temperature 25[°C]

2.2.3. Numerical Procedure

The following settings have been used:

- Analysis type
  - Steady state in double precision
- Advection Scheme
  - High resolution (2nd order accurate)
- Turbulence Numerics
  - First order
- Momentum and Turbulence Fluid False Timescale Control
  - Physical timescale: 0.025[s]
- Energy and Mass Fraction Fluid False Timescale Control
  - Physical timescale: 10[s]
- Convergence Criteria:
  - Residual Target: 1.0E-12

This set up method is a good compromise between result quality and analysis speed, without interfering with its robustness. A tight convergence criteria is required in order to achieve the balance of relevant quantities such as the mass fraction of water vapor, carbon dioxide and oxygen.

2.2.4. Model hypothesis and assumptions

The major hypothesis and the assumptions made in the process of building the model are listed below:

- Plant exchange is modeled on the basis of a single experimental data set (Lettuce GW0704). There is no guarantee that the empirically fitted figures derived from the experimental data used would be adaptable to other datasets and even less to other crops.

- CO_2, O_2 and evapotranspiration rates were not calculated from experiments performed in the HPC. Anyway the chamber used for the experiments (SEC2 chamber) has the same surface area and the same capacity (same number of plants contained) of the HPC. So, we expect that the calculated data are consistent between the two chambers (SEC2 and HPC).

- The calculated Oxygen production rates are not certain and should be treated with caution.

2.2.5. Results

The plant growing environment directly influences the final crop-derived food and the waste composition. It should guarantee optimal, homogeneous and stable growth conditions for plants. Thus its characterization is an important issue.

The distribution of the environmental factors for the two selected time instants (day 9 and day 30) are herein shown and investigated.

Figure 41 shows the locations of the longitudinal and transversal planes where the distribution of the environmental factors is evaluated.

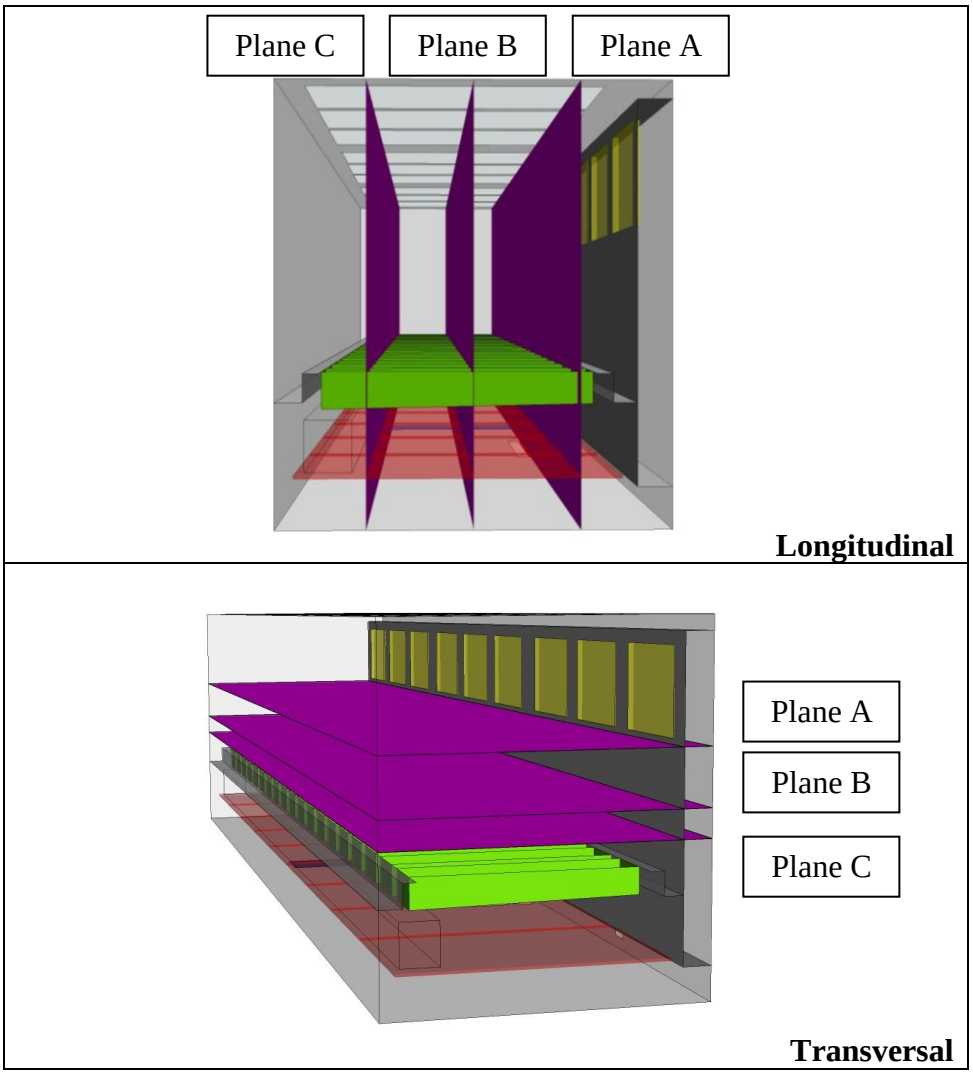

Figure 41 Reference planes

The following considerations could be made for the mass fraction distribution of water vapor and Oxygen (Figures from 42 to 53):

- The longitudinal planes show higher mass fraction values in the region below the trays and the phenomenon is particularly intense at the sides of the chamber.
- The transversal planes show higher mass fraction values in proximity of the back of the chamber.
- As a consequence of the higher flow rate imposed, the mass fraction at day 30 is locally higher in proximity of the plant boundary and globally more diffused in the chamber as compared to the mass fractions at day 9.

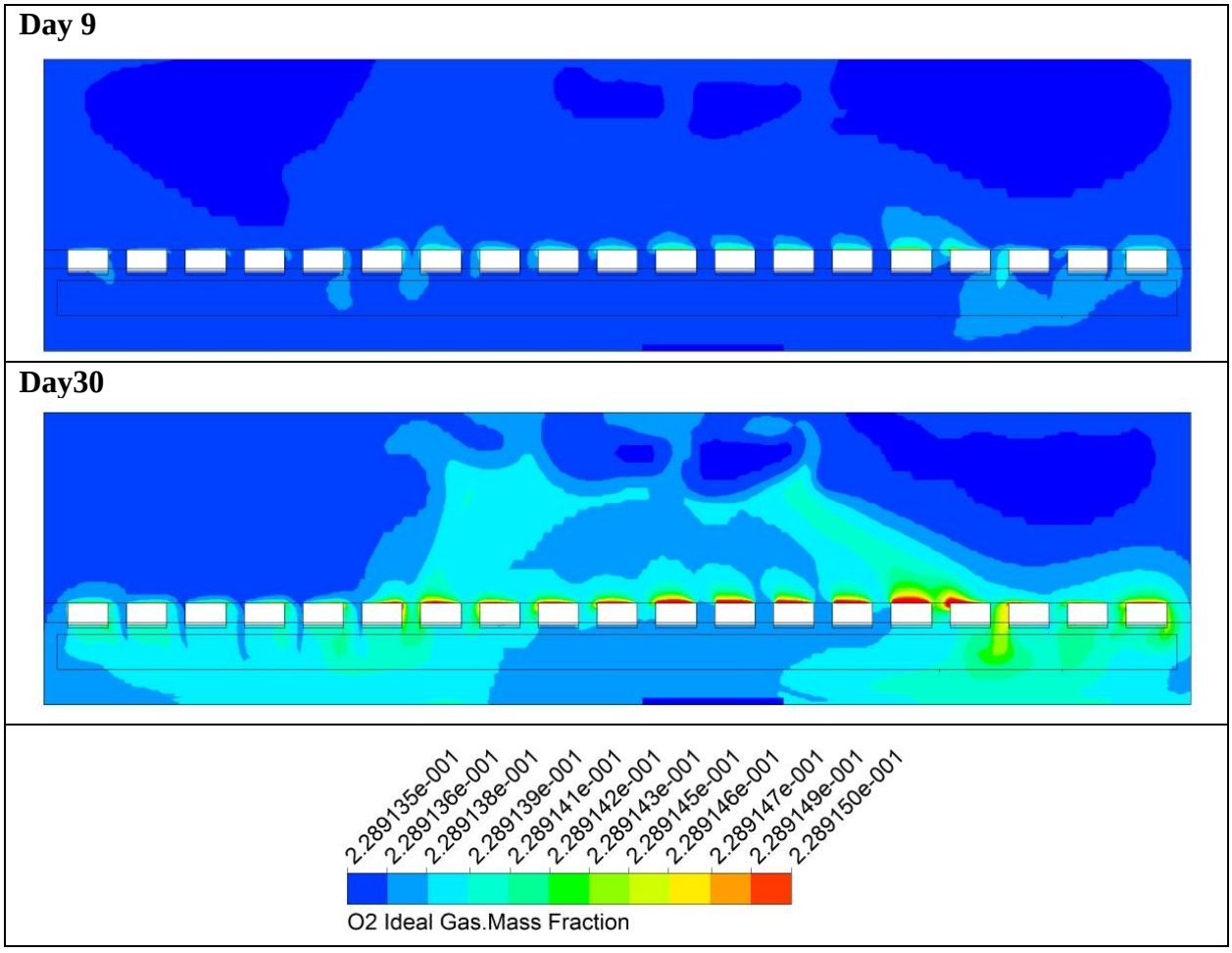

Figure 42 Longitudinal plane A: O_2 distribution

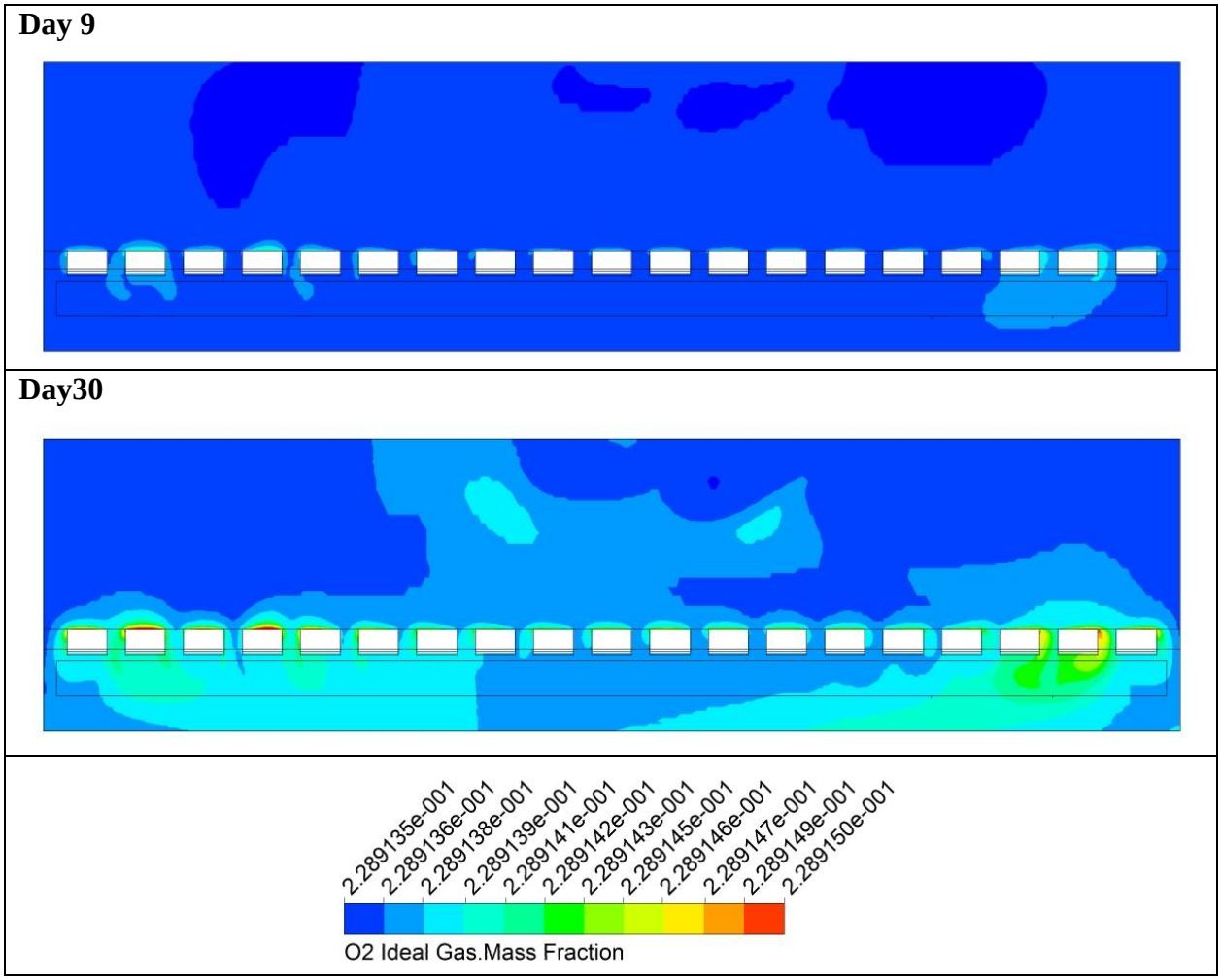

Figure 43 Longitudinal plane B: O_2 distribution

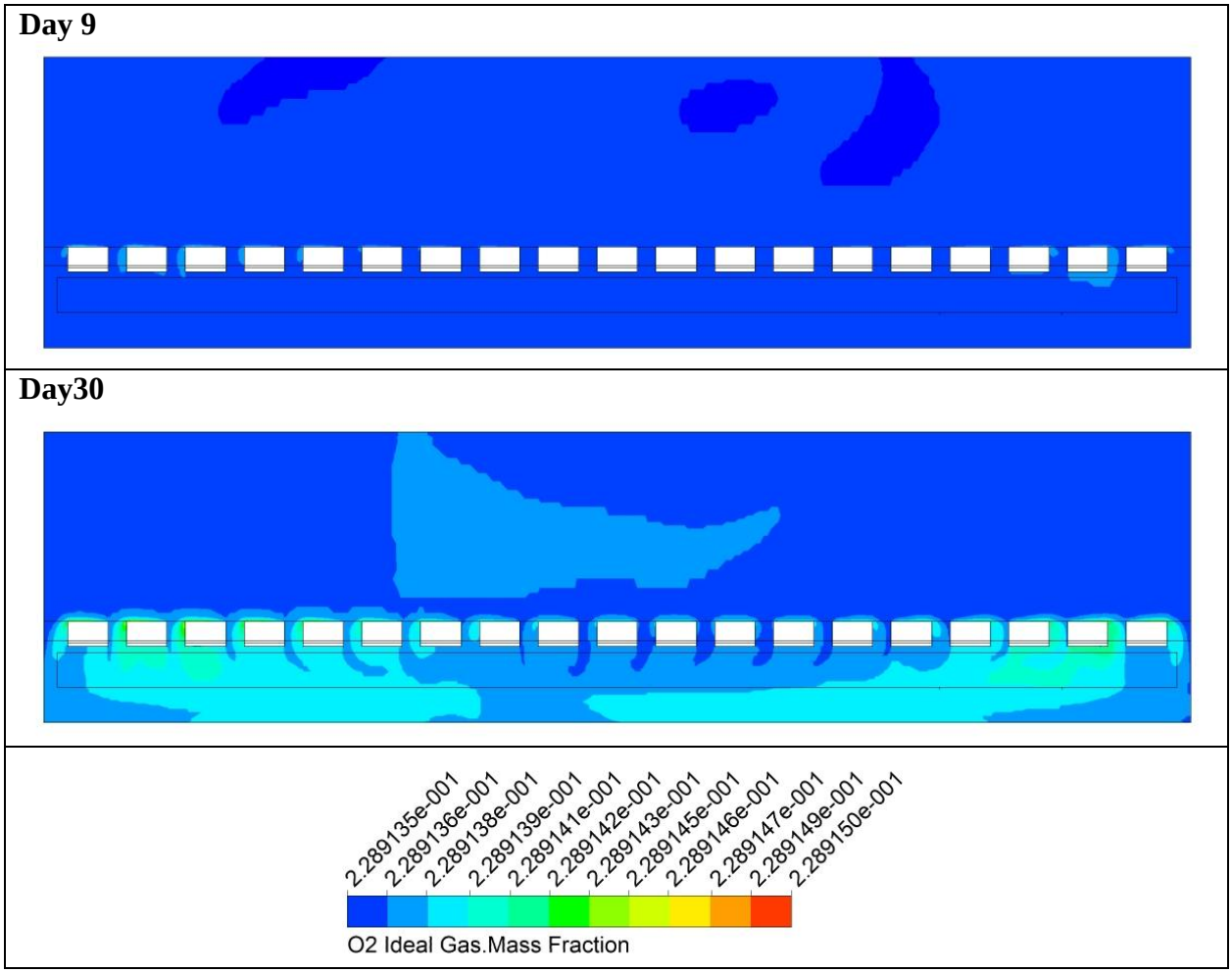

Figure 44 Longitudinal plane C: O_2 distribution

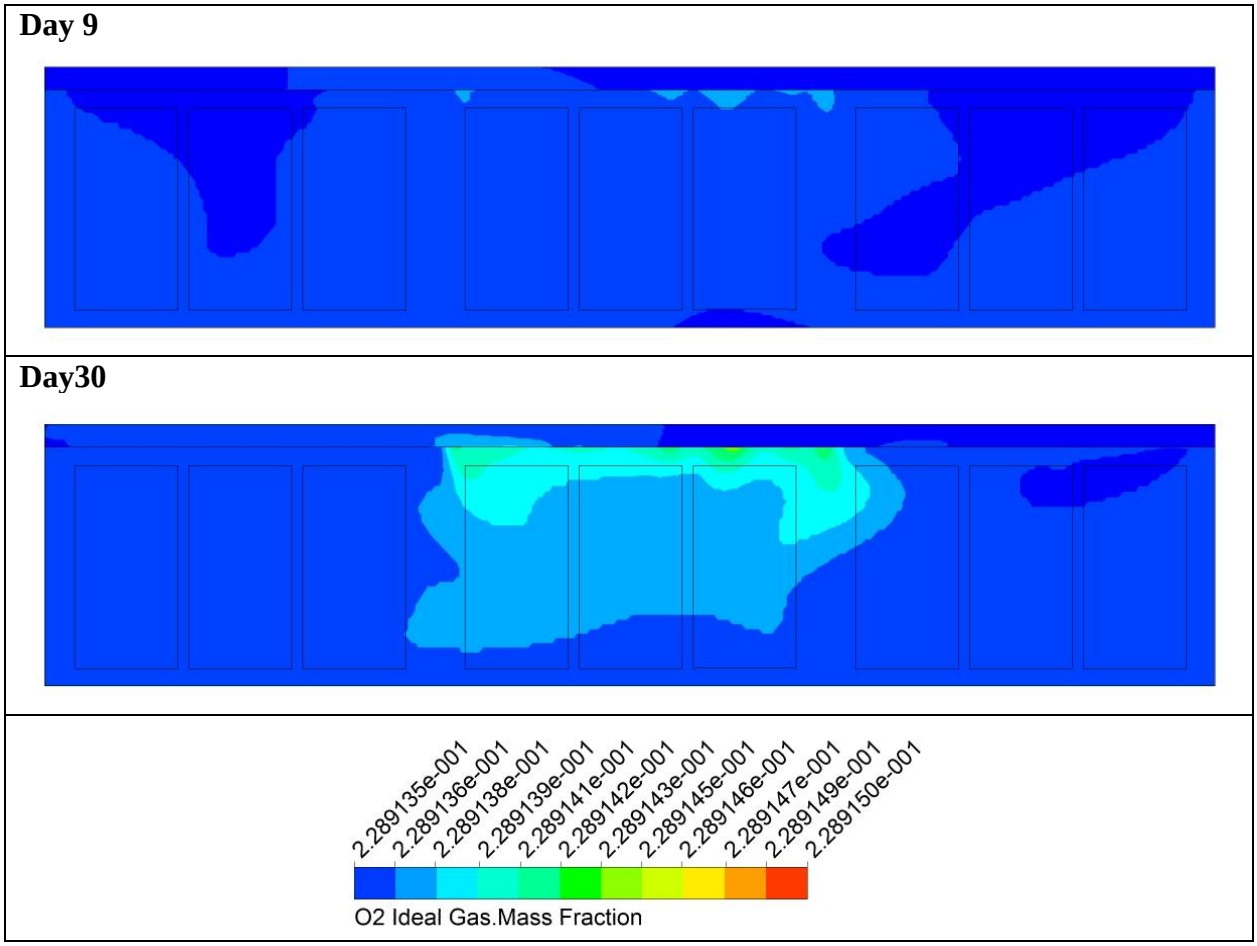

Figure 45 Transversal plane A: O_2 distribution

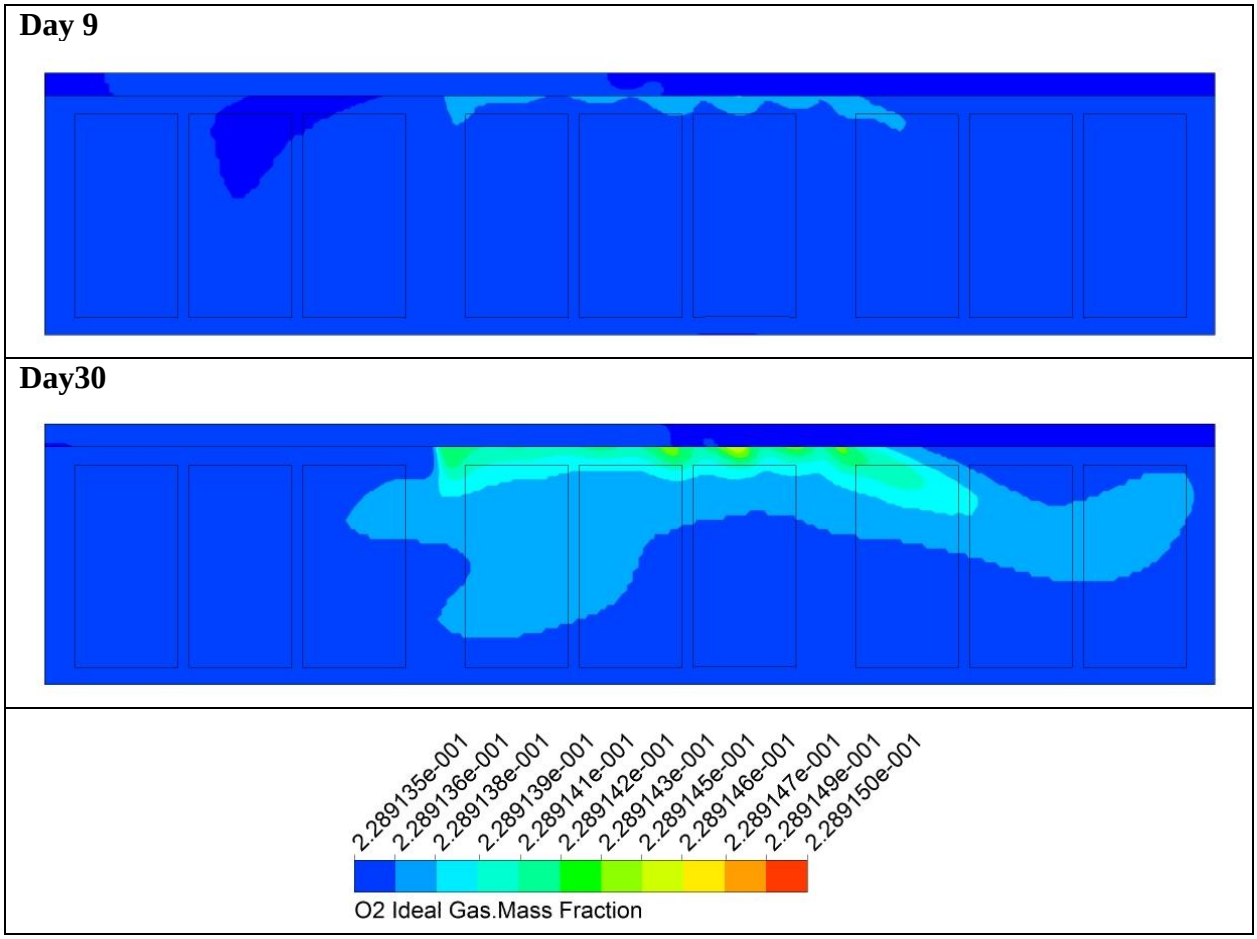

Figure 46 Transversal plane B: O_2 distribution

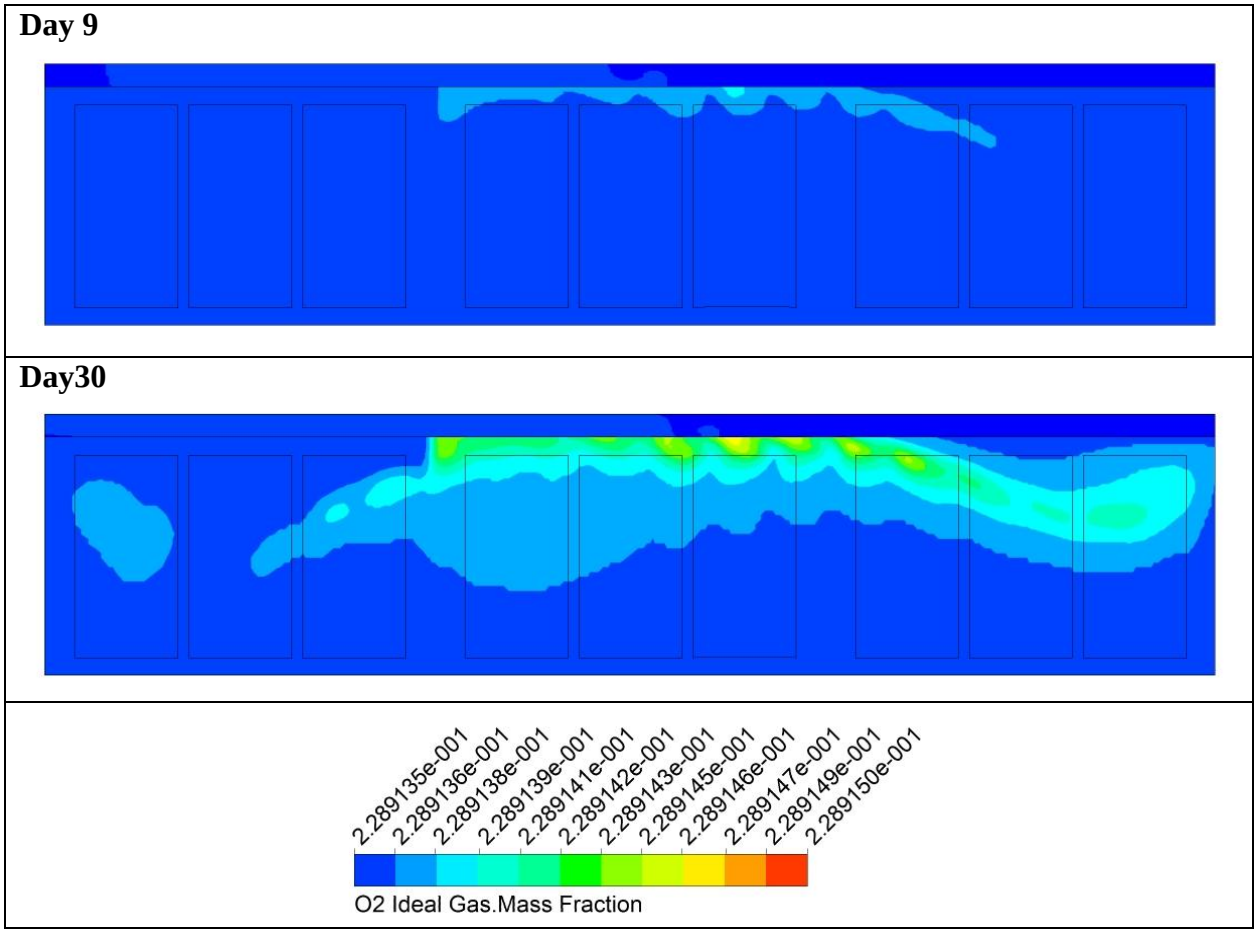

Figure 47 Transversal plane C: O_2 distribution

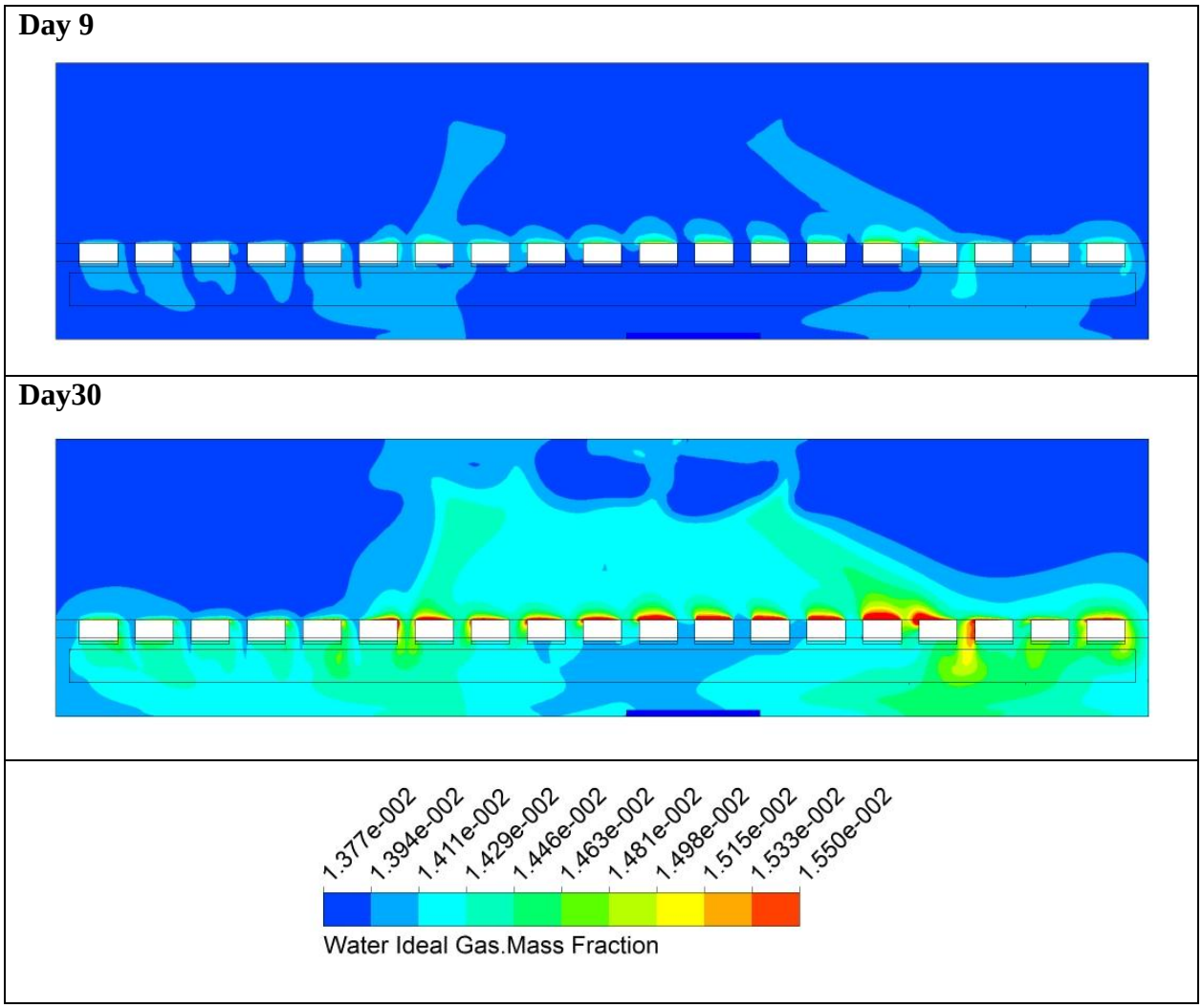

Figure 48 Longitudinal plane A: Water Vapor distribution

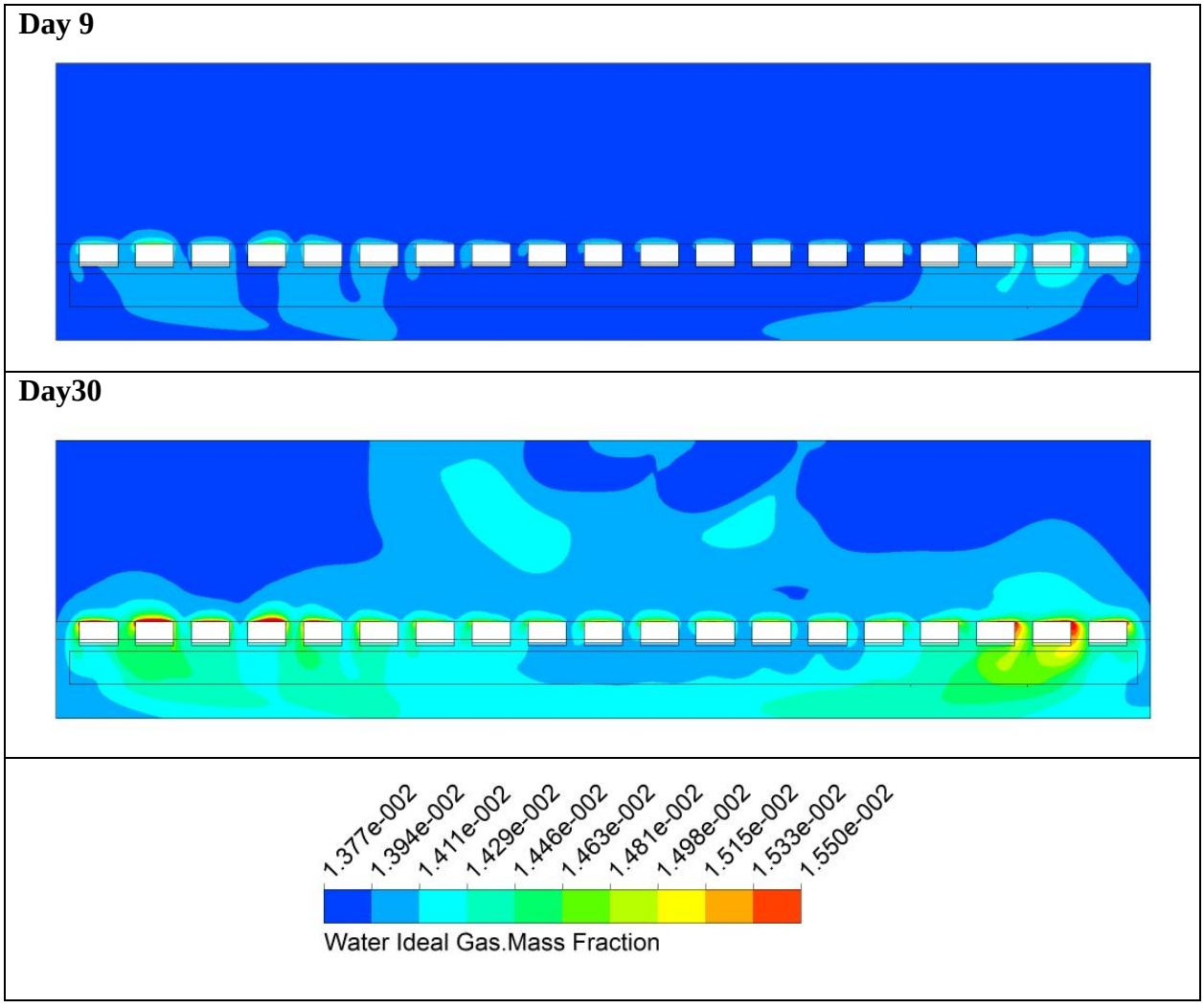

Figure 49 Longitudinal plane B: Water Vapor distribution

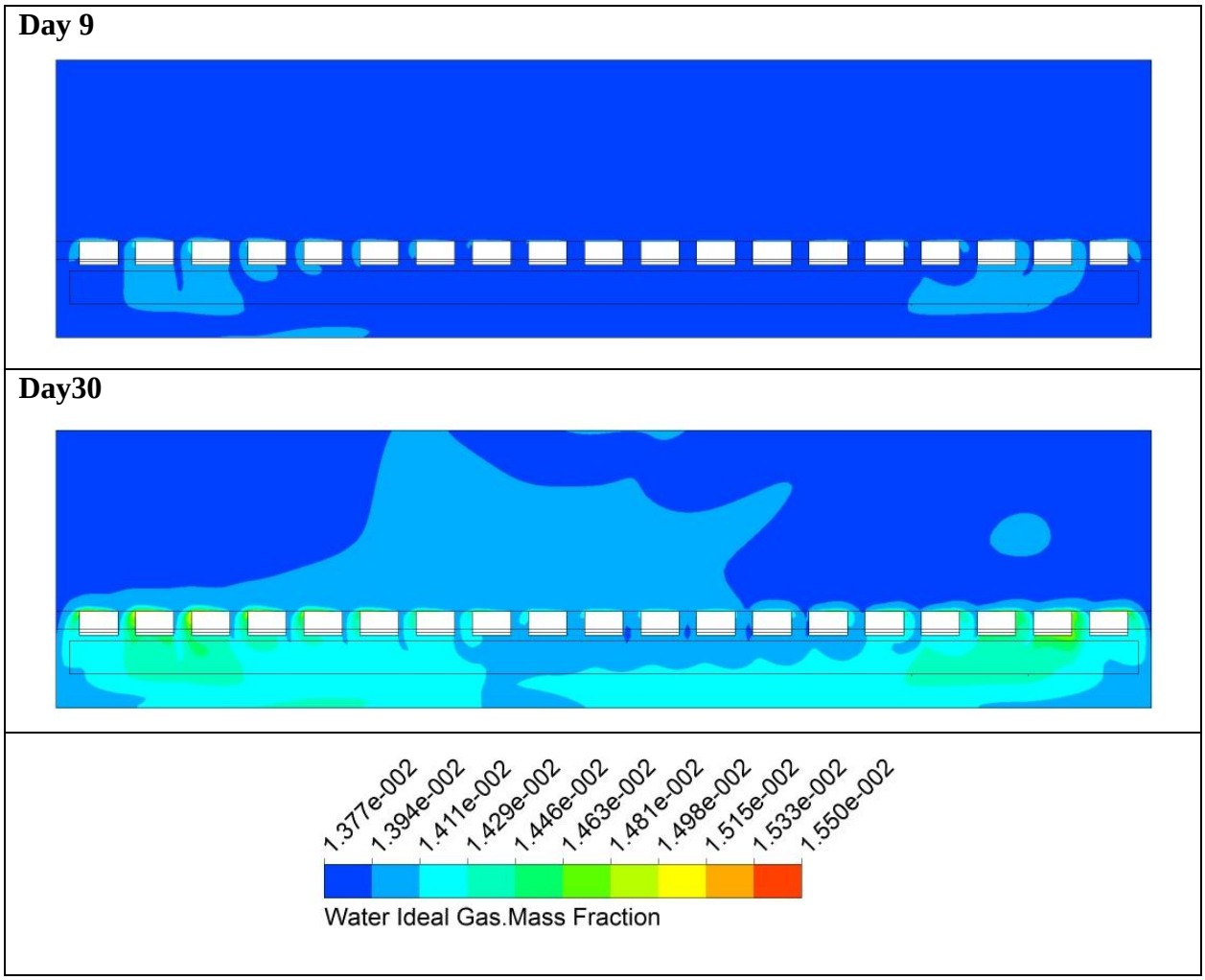

Figure 50 Longitudinal plane C: Water Vapor distribution

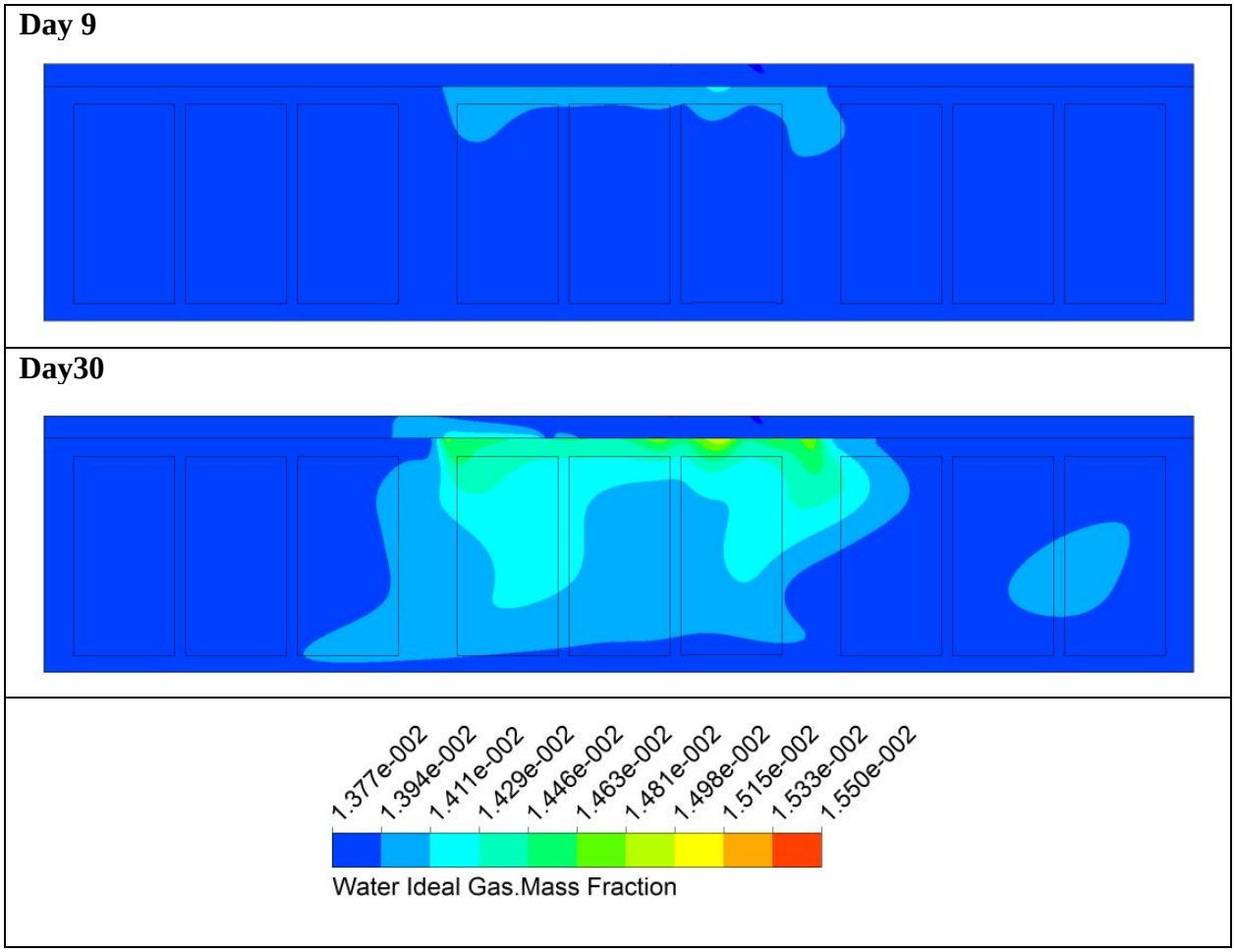

Figure 51 Transversal plane A: Water Vapor distribution

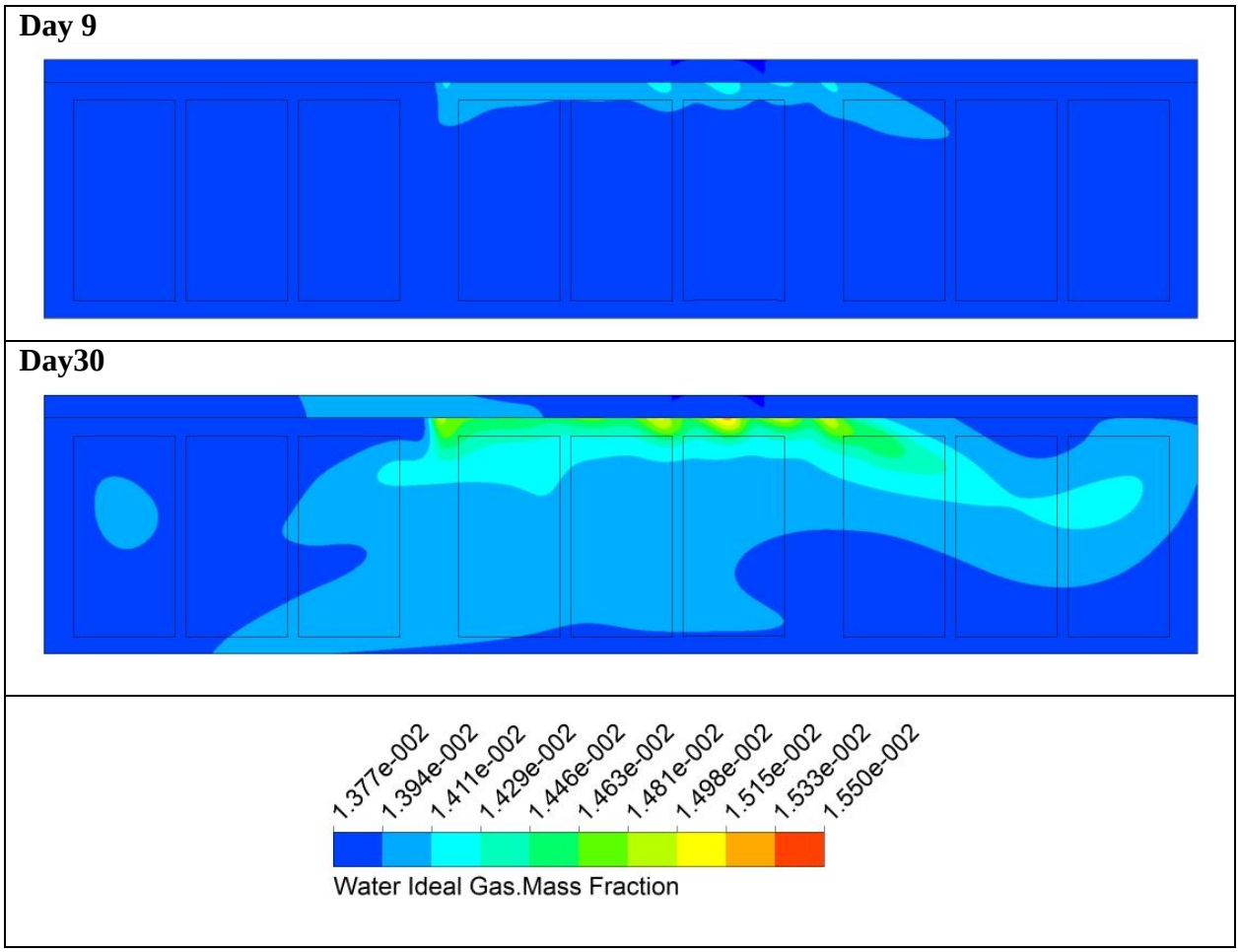

Figure 52 Transversal plane B: Water Vapor distribution

Day 9

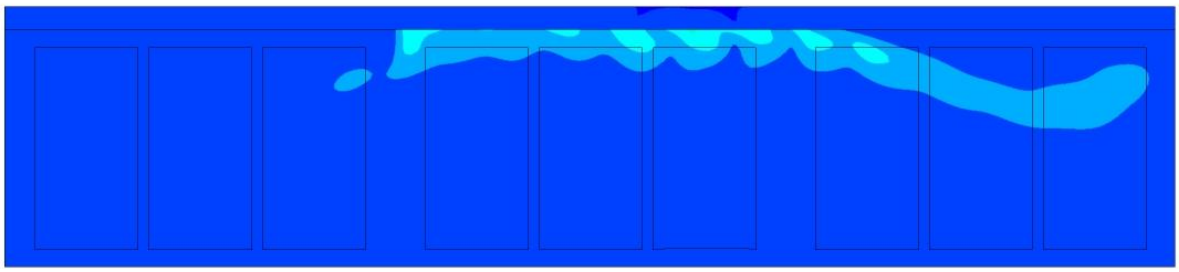

Day30

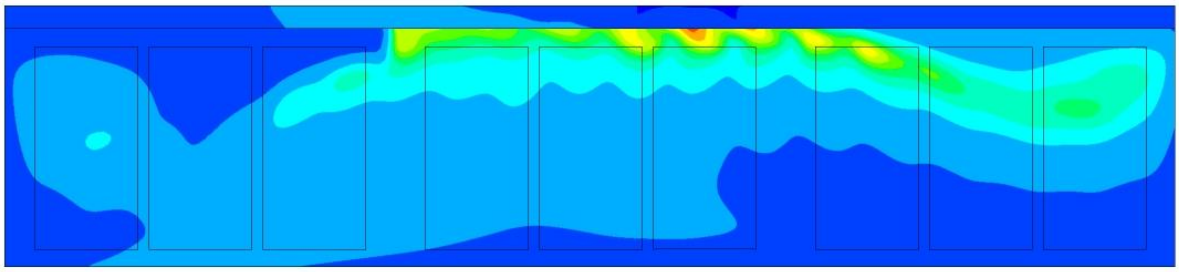

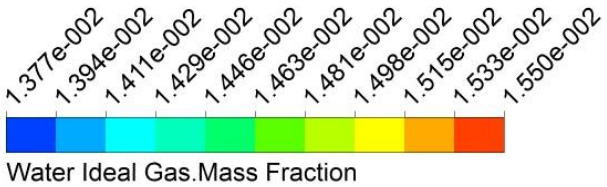

Figure 53 Transversal plane C: Water Vapor distribution

A similar but inversed behavior to that previously described for water vapor and Oxygen is observed for carbon dioxide whose mass fraction distribution is illustrated from Figure 54 to Figure 59.

According to these figures, the CO_2 distribution in the chamber is non-homogenous and the trays placed at the central position are better supplied with this primary ingredients for photosynthesis which is actually the chemical reaction that feeds plant growth.

Day 9

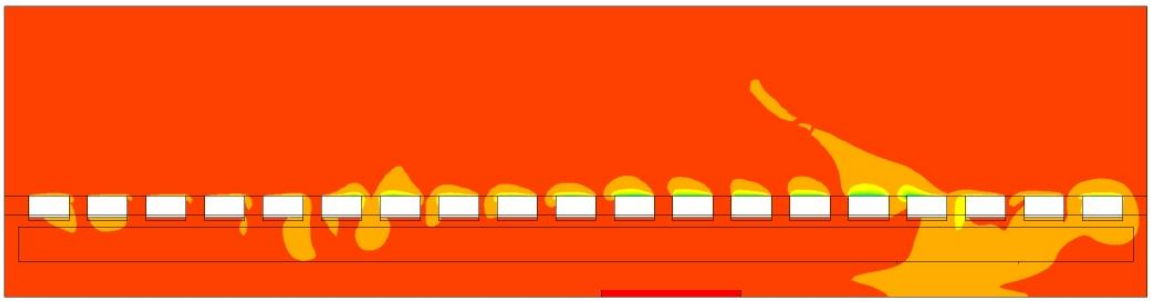

Day30

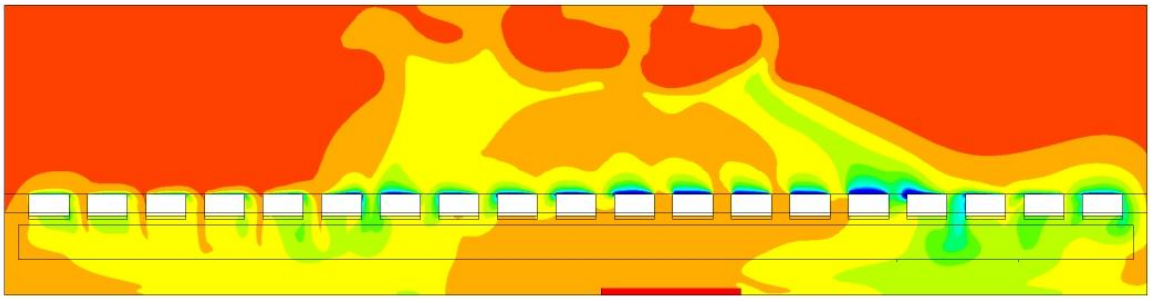

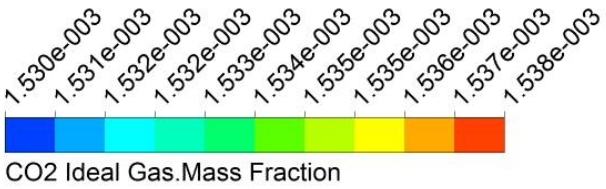

Figure 54 Longitudinal plane A: CO_2 distribution

Day 9

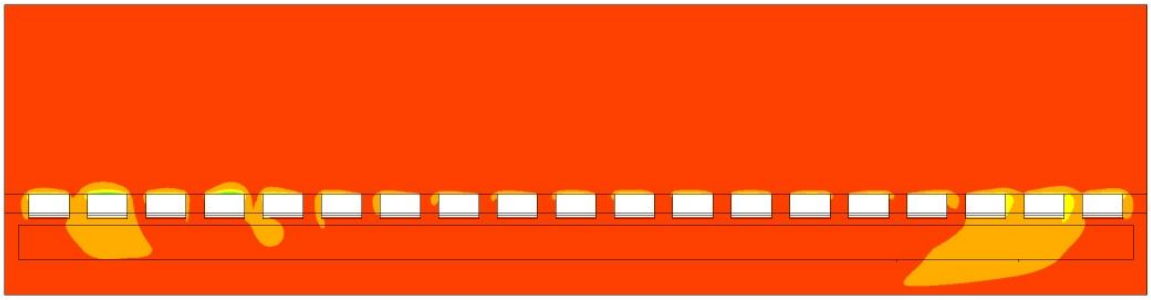

Day30

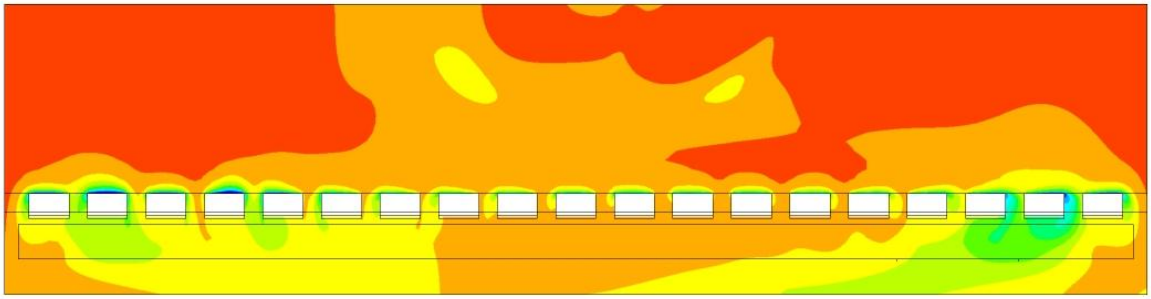

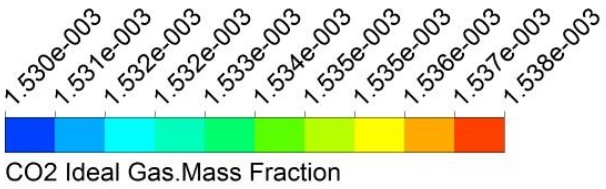

Figure 55 Longitudinal plane B: CO_2 distribution

Day 9

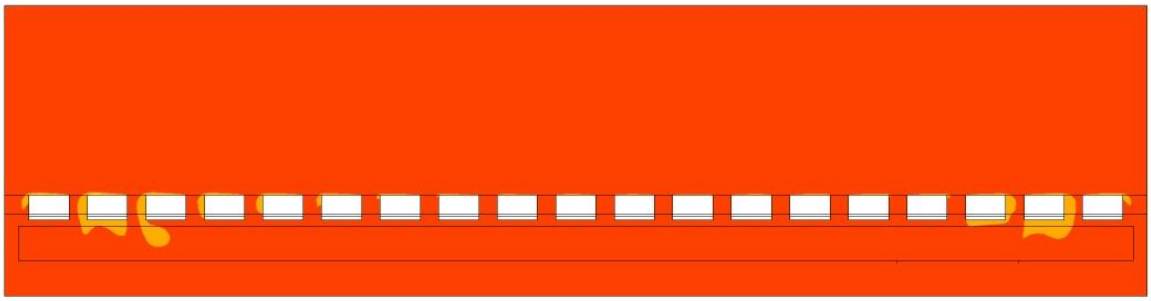

Day30

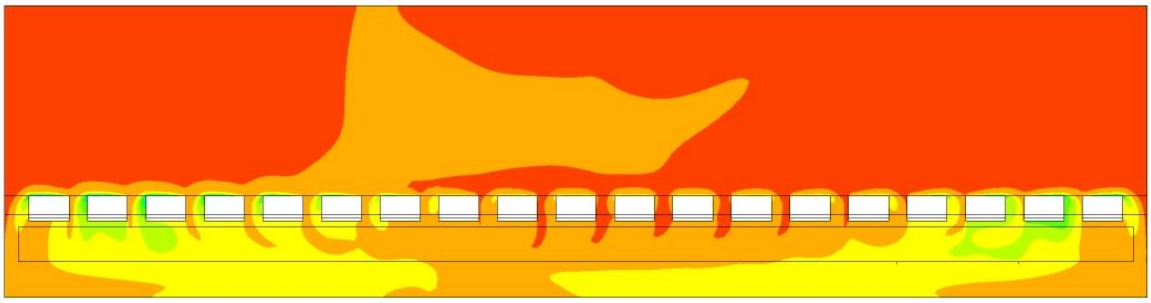

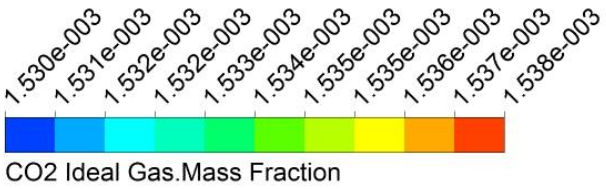

Figure 56 Longitudinal plane C: CO_2

Day 9

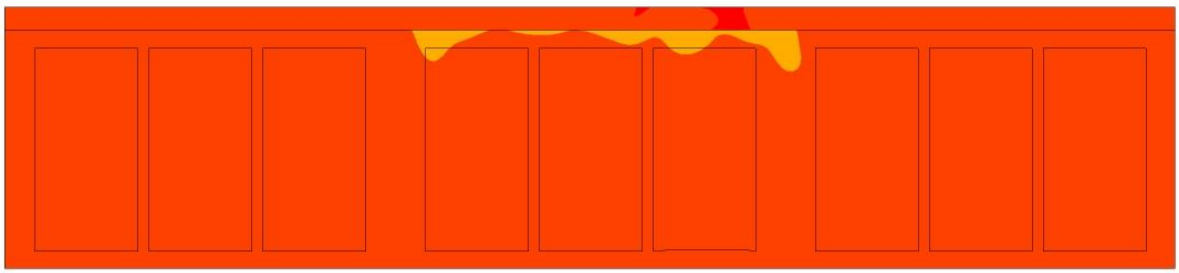

Day30

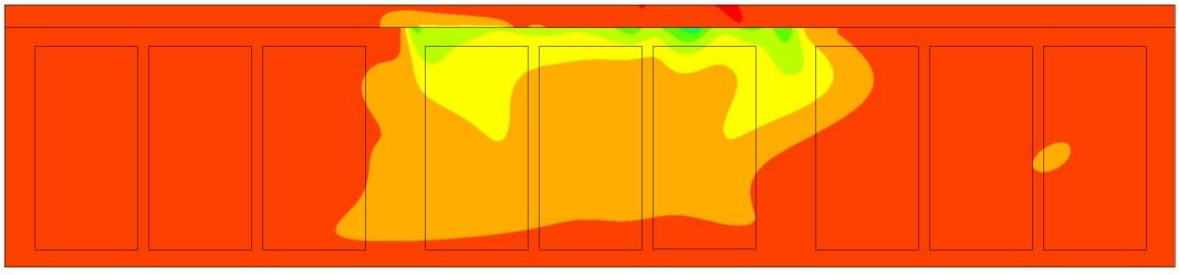

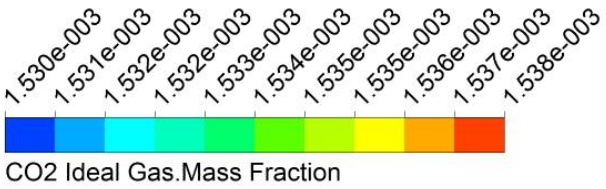

Figure 57 CO2: transversal plane A

Day 9

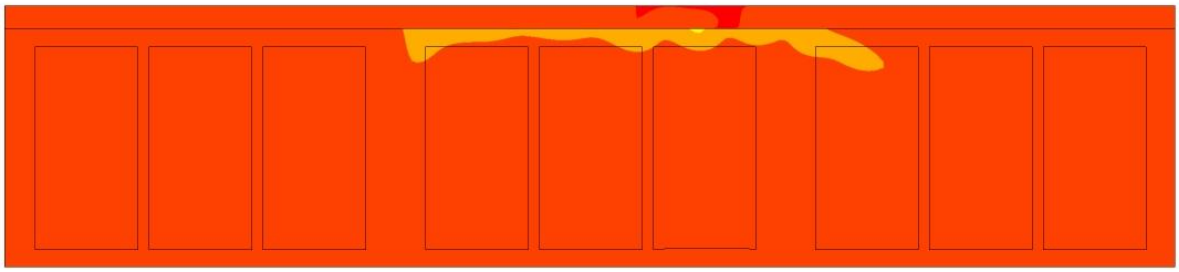

Day30

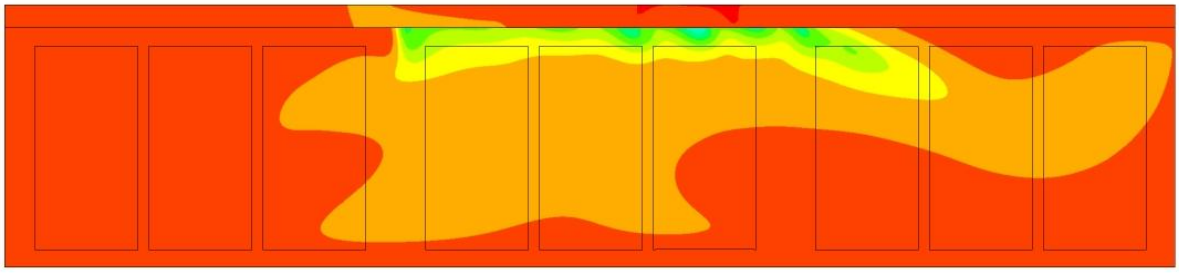

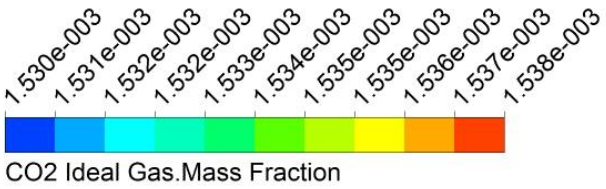

Figure 58 CO2: transversal plane B

Day 9

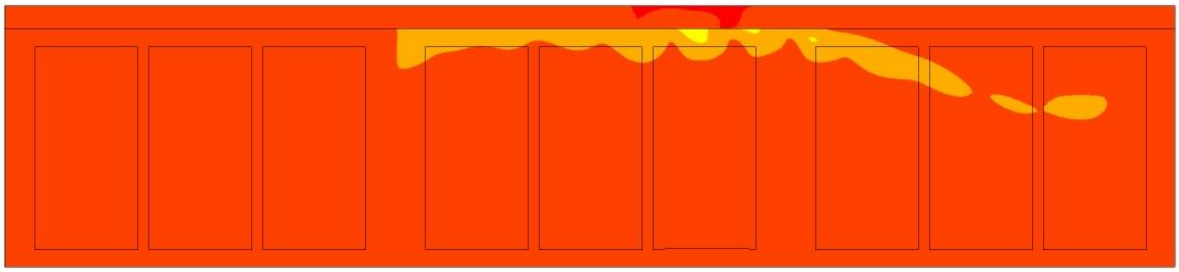

Day30

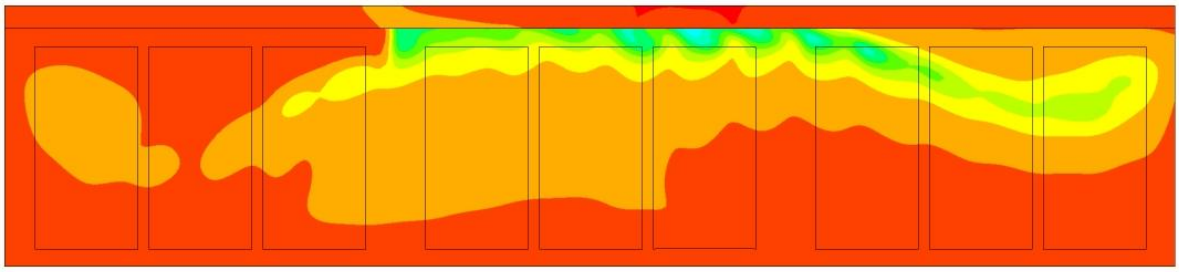

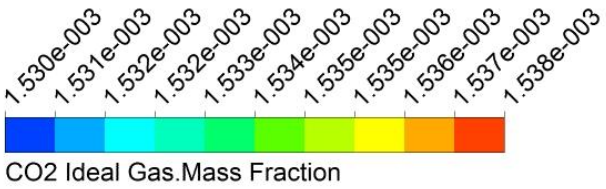

Figure 59 CO2: transversal plane C

Figure 60, Figure 61 and Figure 62 show the temperature distribution in the chamber on three transversal planes (see Figure 41 for the plane locations). These figures highlight that:

- The lower temperature values are located in proximity of the plants boundary where a latent heat sink associated with the water evaporation is present.
- The higher flow rate of water vapor at day 30 shifts the temperature to lower values in accordance with the higher latent heat of evaporation.

Day 9

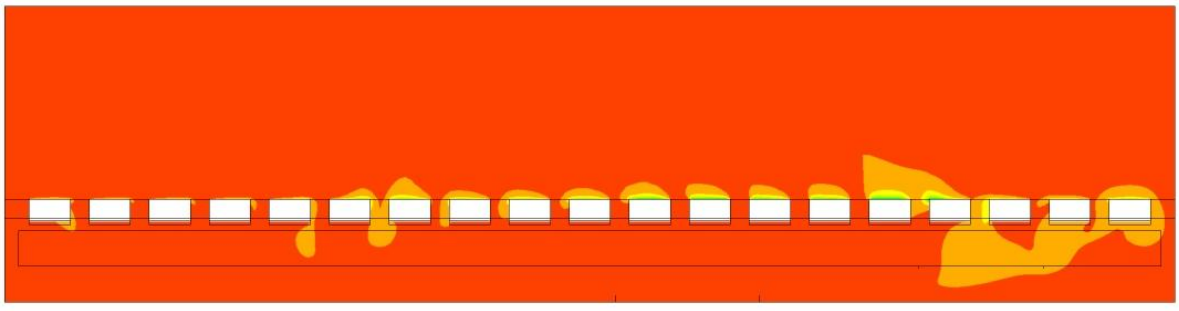

Day30

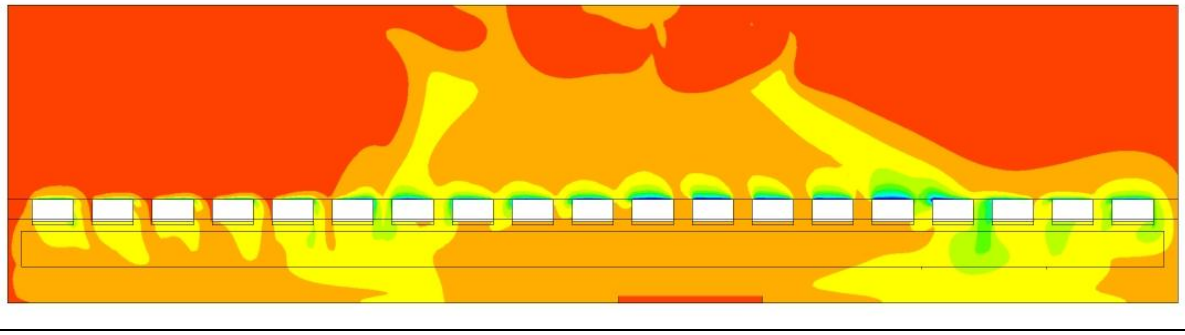

Figure 60 Temperature: longitudinal plane A

Day 9

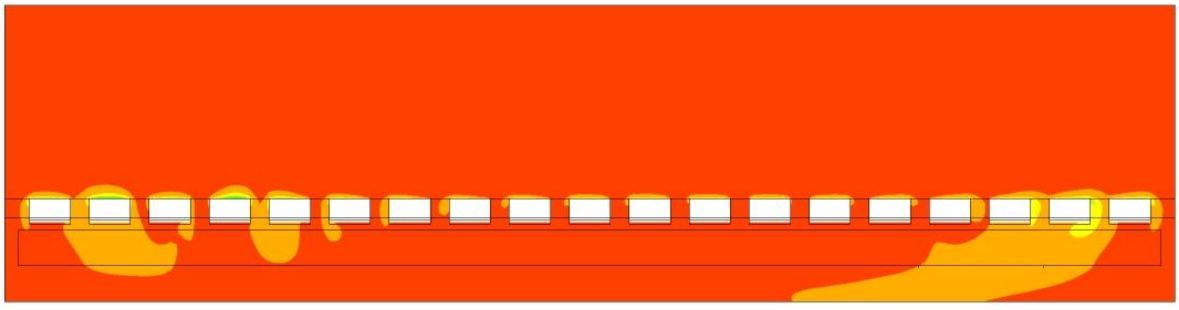

Day30

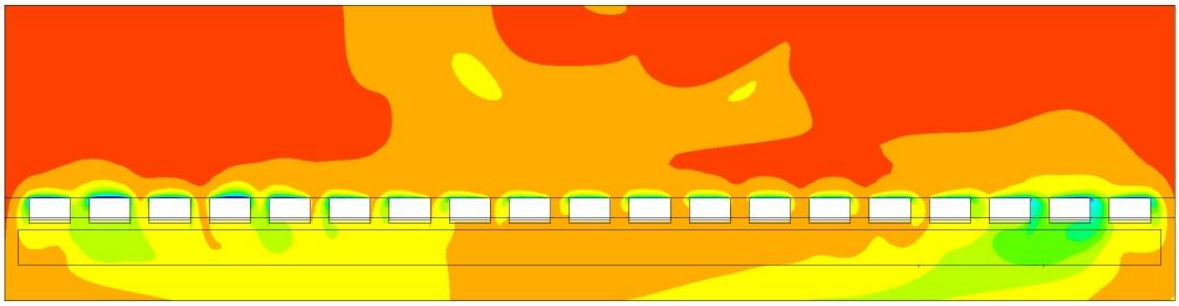

Figure 61 Temperature: longitudinal plane B

Day 9

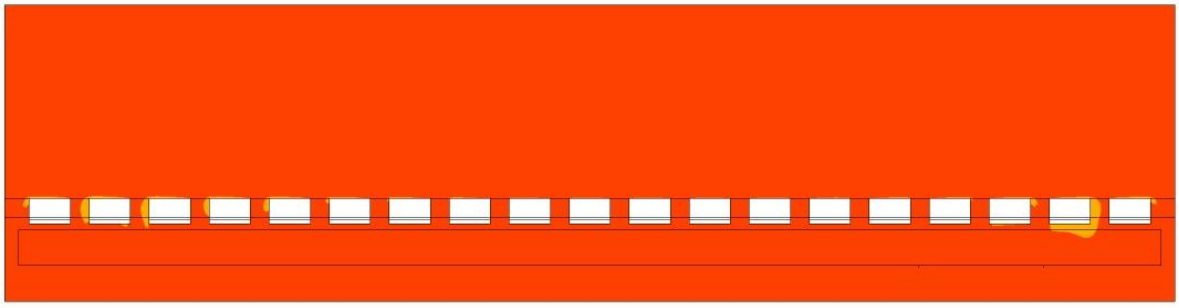

Day30

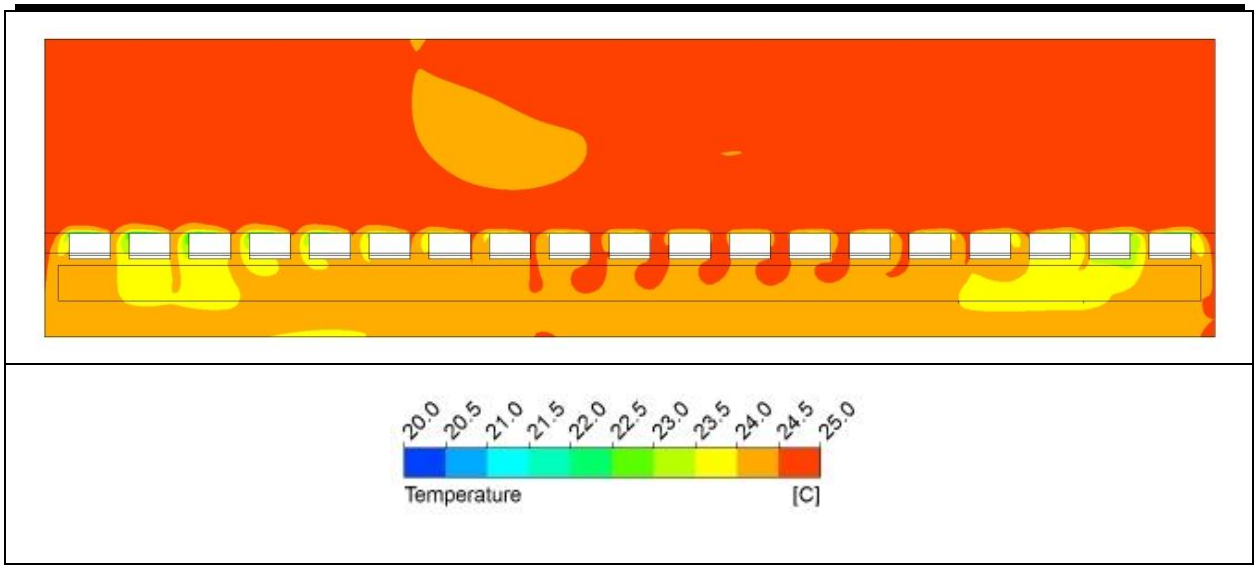

Figure 62 Temperature: longitudinal plane C

The air flow circulation patterns directly affect the distribution of the environmental factors in the chamber. However, the variation in concentration of the gas mixture introduced by the plant metabolism are very small. The convective flow is the dominant physical aspect.

This statement is supported by Figure 63, Figure 64 and Figure 65.

Figure 63 shows the velocity vectors on a cross section plane placed at the exit of grid 6 which was found to have a key role in the flow distribution (47% of the total flow rate, see Table 7). On this cross section, the main flow follows a circular path moving from the back of the chamber to the front wall and then turning back.

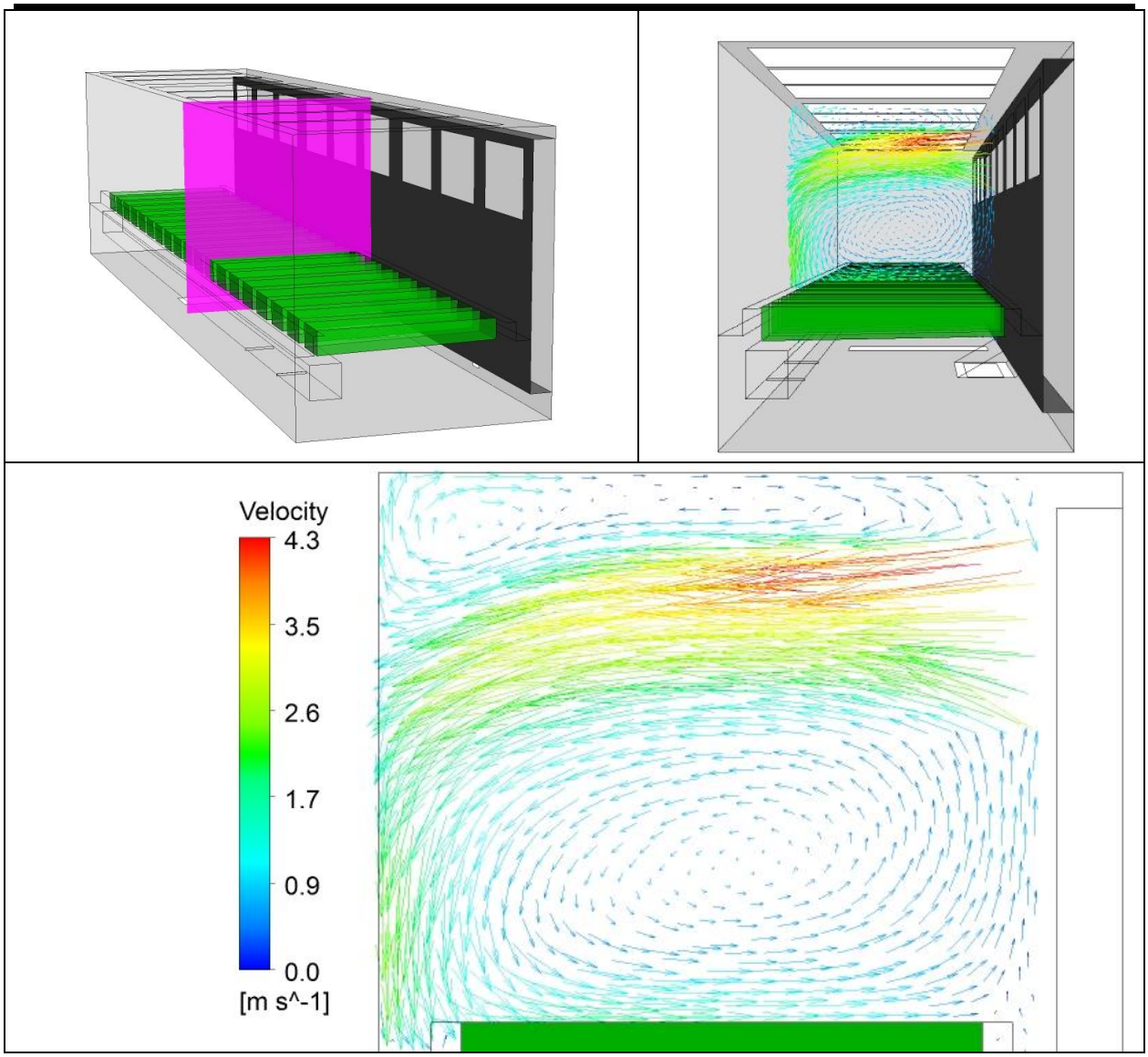

Figure 63 Characteristic flow pattern in the chamber

Figure 64 and Figure 65 display the iso-surfaces of air at the relative humidity of 78% and 85%. It's clearly visible how water vapor is carried by the air flow in the way described above leading to an uneven distribution of this environmental factor.

The same considerations made for the water vapor could be extended to Oxygen and Carbon Dioxide. Since their flow rates are two orders of magnitude lower than the one of the water vapor (see Table 14), the convective flow is still the dominant physical aspect and its action should be even more overriding.

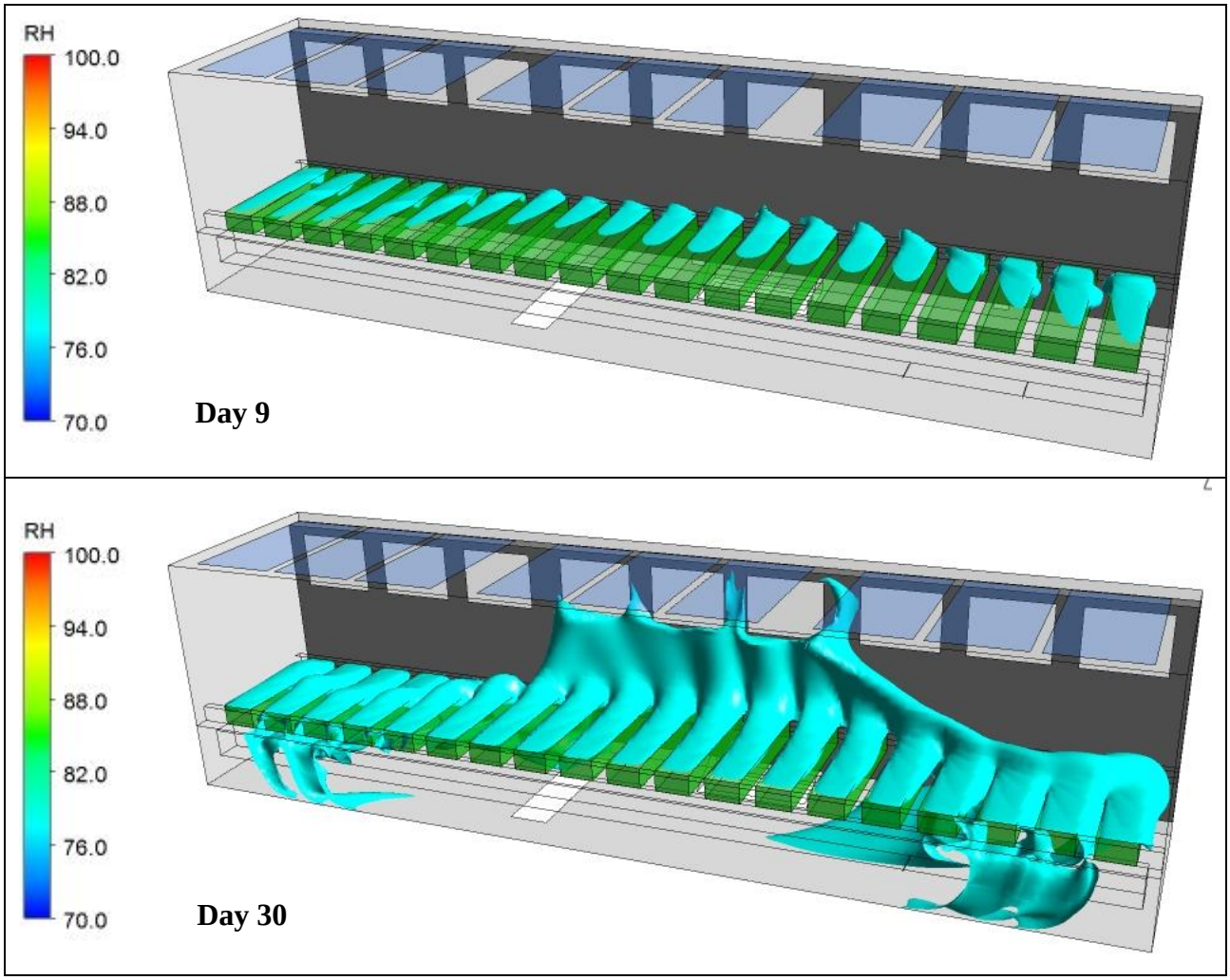

Figure 64 Isosurface: Relative Humidity 78%

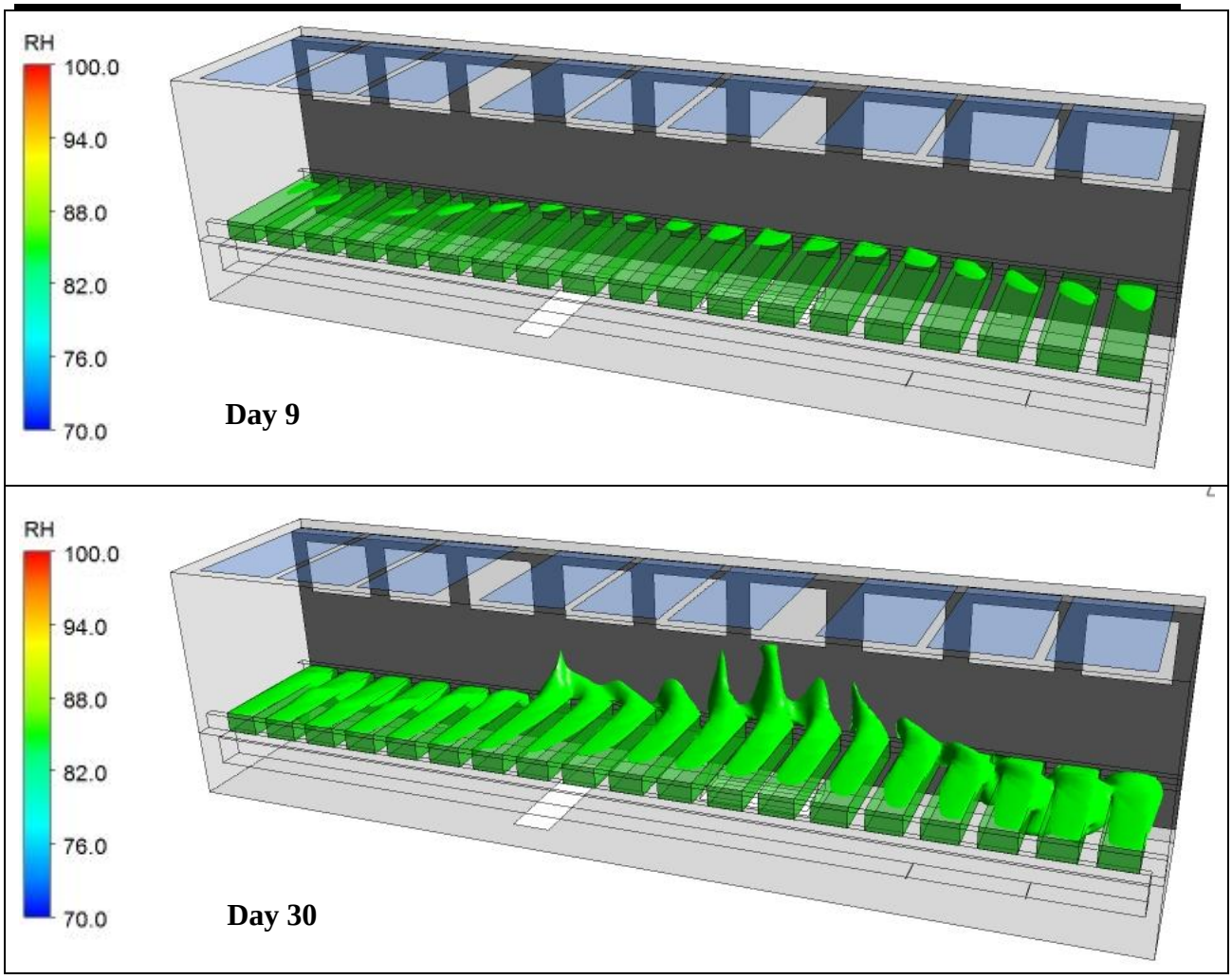

Figure 65 Isosurface: Relative Humidity 85%

2.3. Advanced Canopy Sub Model

2.3.1. Geometry and Computational Grid

The Canopy sub model is a local model of the chamber domain purpose-built to isolate the geometry of a single tray. It is generated by partitioning the chamber described in the step1. The block resulting from the partition is shown in the figure below.

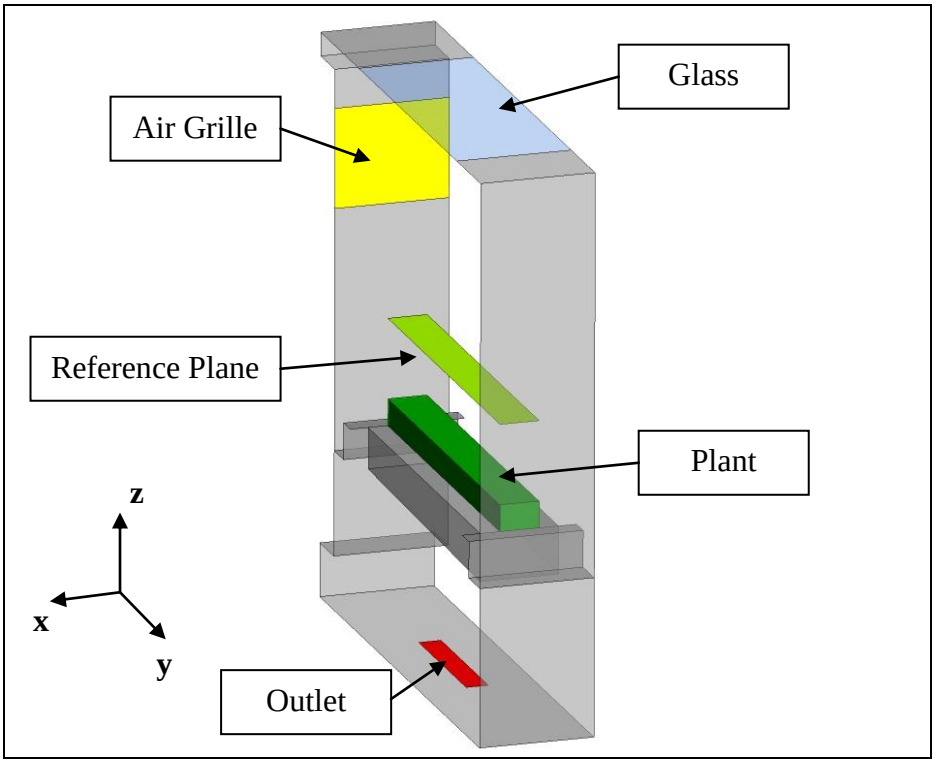

Figure 66 Sub model geometry

The block includes the geometry of an air grille and the roof glass. The balancing panel is neglected and an opening with a geometrical configuration comparable to the chamber outlet is placed at the basis of the block. Furthermore a polygonal geometry is positioned at the top of the tray to idealize the presence of a plant.

The computational domain has been divided into 311740 hexahedral elements generated with the HEXA module of the meshing code ANSYS ICEM. Figure 67 shows some details of the mesh.

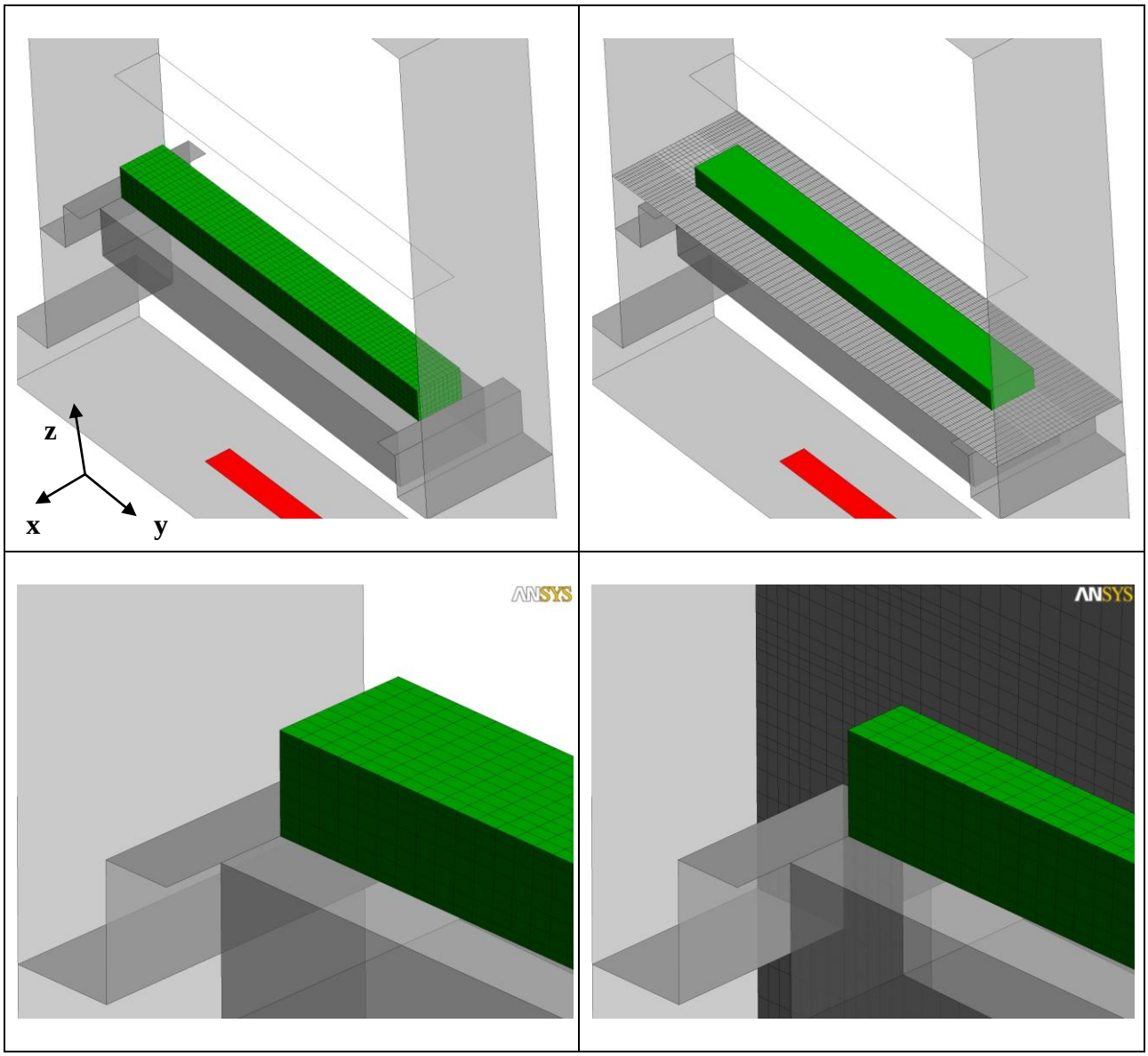

Figure 67 Sub model mesh details

2.3.2. Physical properties and boundary conditions

The flow has been considered:

- Steady
- Multiphase: a variable composition mixture is involved in the calculation. Air is treated as an ideal mixture of Oxygen, water vapor, Carbon dioxide and Nitrogen.
- Turbulent: the standard $k\,\varepsilon$ model with scalable wall functions has been used
- Buoyant: the gravity effect has been taken into account

The energy equation (thermal energy) has been taken into account, as well as the radiation following the Montecarlo model. The radiation model details can be found in paragraph 1.4.3.1.

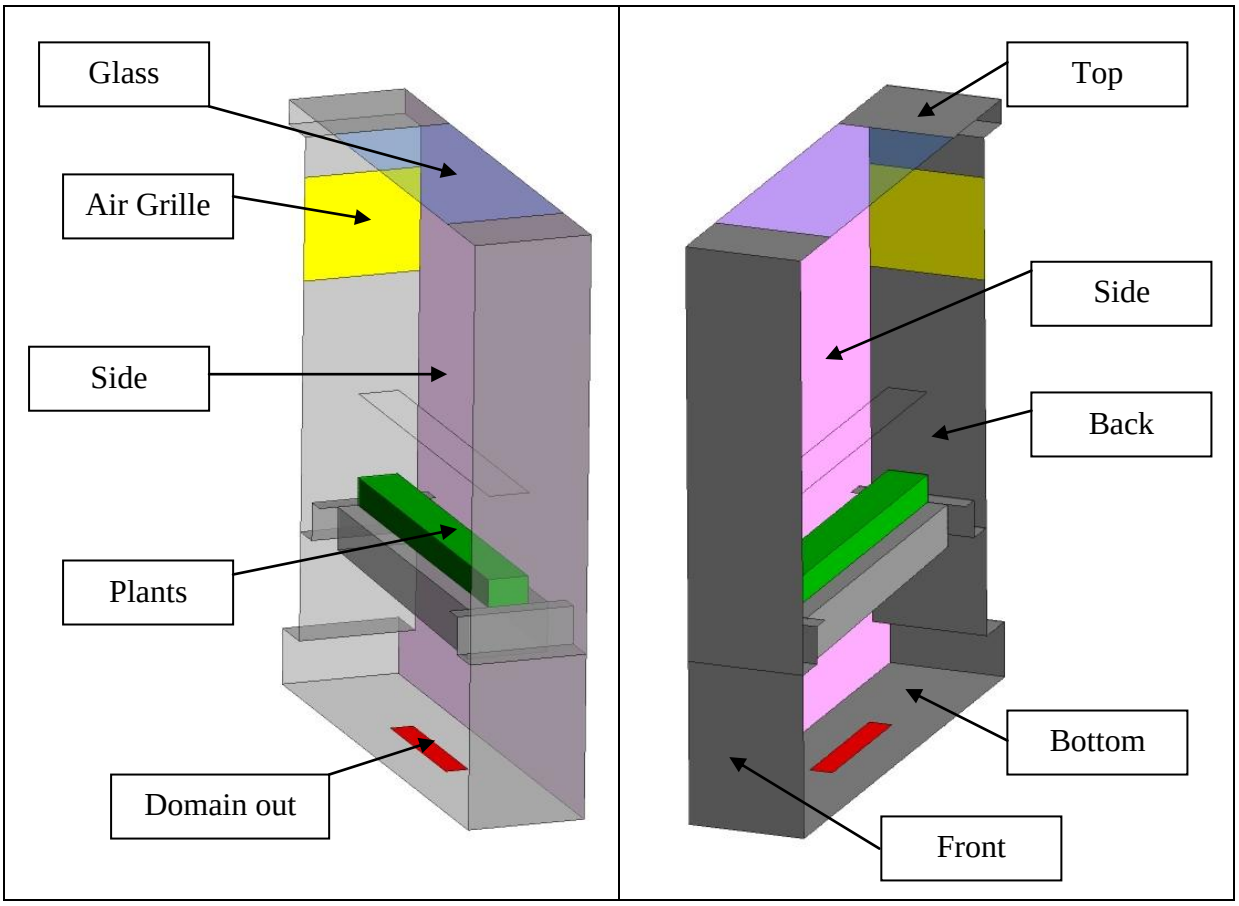

Figure 68 Sub model boundary condition locations

The physical properties of the mixture are reported in the table below:

COMPONENT	Dynamic viscosity [Kg m^{-1} s^{-1}]	Thermal conductivity [W m^{-1} K^{-1}]	Equation of state	Specific Heat Capacity	Model
O_2	1.92e-05	0.0266	Ideal	NASA format	Transport equation
CO_2	1.49e-05	0.0145	Ideal	NASA format	Transport equation
Water vapor	9.4e-06	0.0193	Ideal	NASA format	Transport equation
N_2	1.77e-05	0.0259	Ideal	NASA format	Constrain

Table 15 Physical properties

The specific heat capacity is modeled by using the Ansys CFX built in NASA format polynomials which define specific heat as a function of temperature. The coefficient are fine tuned on the basis of experimental data and a large database is available (ref Ansys Inc 2009. CFX Documentation Release 12.0).
Figure 68 shows the location of all the boundary conditions. Following the set of conditions specified:

AIR GRILLE: an inlet boundary condition has been set in correspondence with the grille. Stating that the total flow rate is supposed to be uniformly distributed to all the air grilles of the chamber, a flow rate of 0.0442 [kg s^{-1}] has been imposed normal to the boundary with a static temperature of 25[C].

DOMAIN OUT: at the base of the sub model an opening with a geometrical configuration comparable to the original opening of the chamber is located but reduced one to ninth in area.

SIDES: a symmetry/periodic boundary condition has been placed at the sides of the sub model.

TOP, BOTTOM, FRONT, BACK: a wall condition has been imposed to all these boundaries which are considered as opaque to radiation with an emissivity of 0.9 and a diffuse fraction coefficient of 0.5. The same convective heat transfer assumptions were made for the front, back and bottom walls (External heat transfer coefficient 20[W m^{-2} K^{-1}], external temperature 25[C]) while for the top wall the external temperature was calculated according to the light loft simulation results (mean loft temperature 32[C]).

PLANTS: the influence of the plants on the air flow has been taken into account by applying a localized pressure gradient to the 3D porous region which schematically represents the plant itself (isotropic pressure loss; K_{loss} 800). Likewise the evapotranspiration phenomena and the photosynthetic response are modeled with a volumetric source for water vapor and O_2 and a

sink for CO_2. The theory underlying the mathematical model which represents the interaction between the plants and the environment as well as the way the model is implemented in the CFD code will be analyzed in more detail in the next paragraph.

GLASS:

- The glass has been considered with the temperature distribution shown in the figure below.

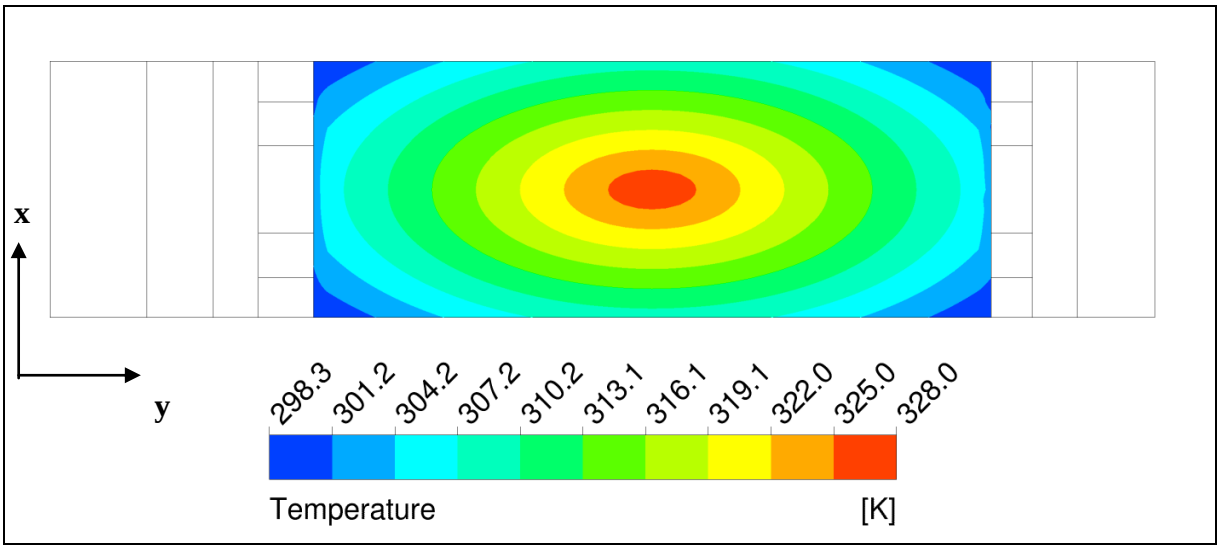

Figure 69 Temperature distribution at the glass surface

- The radiation transmitted by the glass has been modeled with an equivalent source mixing the radiative properties of the two types of lamp (HPS and MH).
  The amount of radiation is calculated as the integral of the radiation transmitted from the light loft to the chamber (4763[W] – step 1) multiplied by portion of the model accounted in the Advanced Canopy submodel (1/19). The percentage of radiative heat emitted in the visible range is 22.27%.

- The emissivity values of the glass for each spectral band in the visible range are shown in the table below:

Bands (nm)		Emissivity
From	to	
380	510	0.1922
510	650	0.7447
650	780	0.0631

Table 16 Glass emissivity in the visible spectrum

The contribution of the radiation emitted from the glass in the ultra violet (UV) and in the infrared (IR) spectrum has been included in the thermal radiation calculation with two additional bands. The UV band ranges from 100 to 380 [nm] with an emissivity value on the bulb of 0.0475 .The IR band ranges from 780 to 100000 [nm] with an emissivity of 0.9525.

2.3.3. Plant-environment interaction

The form of the Penman-Monteith equation presented below was used in the CFD simulation to predict evapotranspiration rates at specified values of net radiation, saturation vapor pressure deficit, size of the leaf, air flow speed and stomatal resistance (Dixon & GRACE, 1983).

$$\lambda E = \frac{sRn + \rho c_p [e_s(T_a) - e_a] / r_a^h}{s + \gamma (r_a^w + r_s) / r_a^h}$$

where:
λ = latent heat of vaporization ($J\ kg^{-1}$);
E = flux density of water vapor in air ($kg\ m^{-2}\ s^{-1}$);
s = slope of the saturation vapor pressure vs temperature curve for water at the mean of the leaf and air temperature ($Pa\ °C^{-1}$);
Rn = net radiation absorbed by the leaf (W m^{-2});
ρ = density of air (kg m^{-3});
c_p = specific heat of air at constant pressure (J kg^{-1} $°C^{-1}$);
$e_s(T_a)$=saturation vapor pressure of water at air temperature (Pa);
e_a = vapor pressure of water in the ambient air (Pa);
r_a^h = aerodynamic resistance for heat ($s\ m^{-1}$);
r_a^w = aerodynamic resistance for water vapor ($s\ m^{-1}$);
γ = psycrometric constant ($Pa\ °C^{-1}$);
r_s = leaf surface resistance ($s\ m^{-1}$);

The net radiation absorbed by the leaf (Rn) is directly extracted from the flow field solved via CFD simulation and its value is estimated as shown Figure 70.

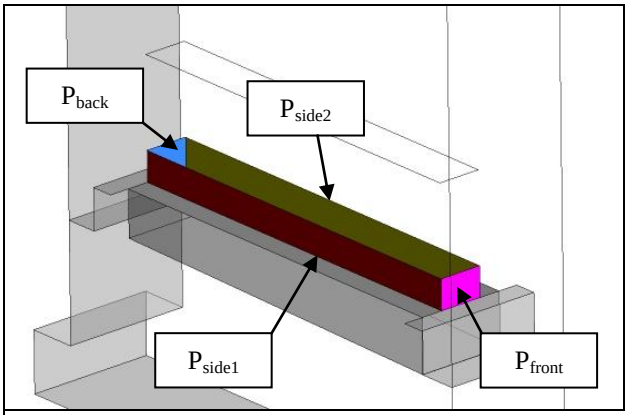

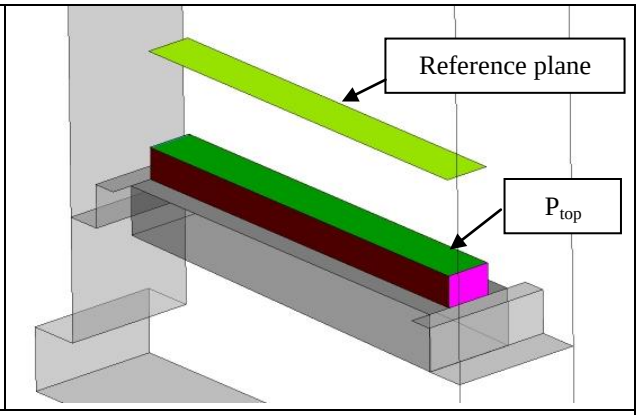

$$Rn = \int_{A_{back}} RdA + \int_{A_{front}} RdA + \int_{A_{side1}} RdA + \int_{A_{side2}} RdA + \int_{A_{top}} RdA$$

Figure 70 Net radiation absorbed (R_n)

The saturation vapor pressure ($e_s(T_a)$), the local vapor pressure (e_a) and the slope of the saturation vapor pressure (s) are indirectly numerically solved from the evaluation of the temperature and pressure field.

In order to use equation 1 in a predictive sense, the relationship between the air flow speed and the aerodynamic resistance for water was calculated using the boundary layer theory. This relationship is described by the formula:

$$r_a = \frac{d^{0.5} v^{0.17}}{0.66 D^{0.57} u^{0.5}}$$

where
d = size of the leaf (m);
v = kinematic viscosity of air ($m^2\ s^{-1}$);
D = diffusion coefficient of water vapor in air ($m^2\ s^{-1}$);
u = air flow speed ($m\ s^{-1}$) calculated as the area average of the velocities at the reference plane indicated in Figure 70.

Then to complete the data set, the value of the aerodynamic resistance for heat is required. A correlation factor of 1.08 was used to convert the aerodynamic resistance for water to the aerodynamic resistance for heat.

The rates of oxygen production and carbon dioxide absorption are assumed to be directly proportional to the flux of water vapor. The experimental data already employed in the baseline model are herein used to fine tune the proportion coefficients. The values of the coefficients are reported in the next paragraph.

2.3.4. Initial boundary conditions

Two sets of boundary conditions are considered: day 9 and day 30. The two sets of boundary conditions are shown in the following table:

	Day 9	Day 30
Plant height [cm]	6	12
Chamber Temperature [°C]	25	25
Relative Humidity [%]	70	70
Mass fraction O_2	0.2289	0.2289
Mass fraction CO_2	0.0015	0.0015
O_2 proportionality coef.	7E-04	7.3E-04
CO_2 proportionality coef.	3.4E-03	3.6E-03

Table 17 Initial conditions

For both sets of boundary conditions, the same light set up has been used. The direction of the light radiation is slightly inclined as shown in Figure 71. The vector of the emitted radiation linearly changes with the position. Its value is zero at the center of the glass and 5 degrees at the glass sides.

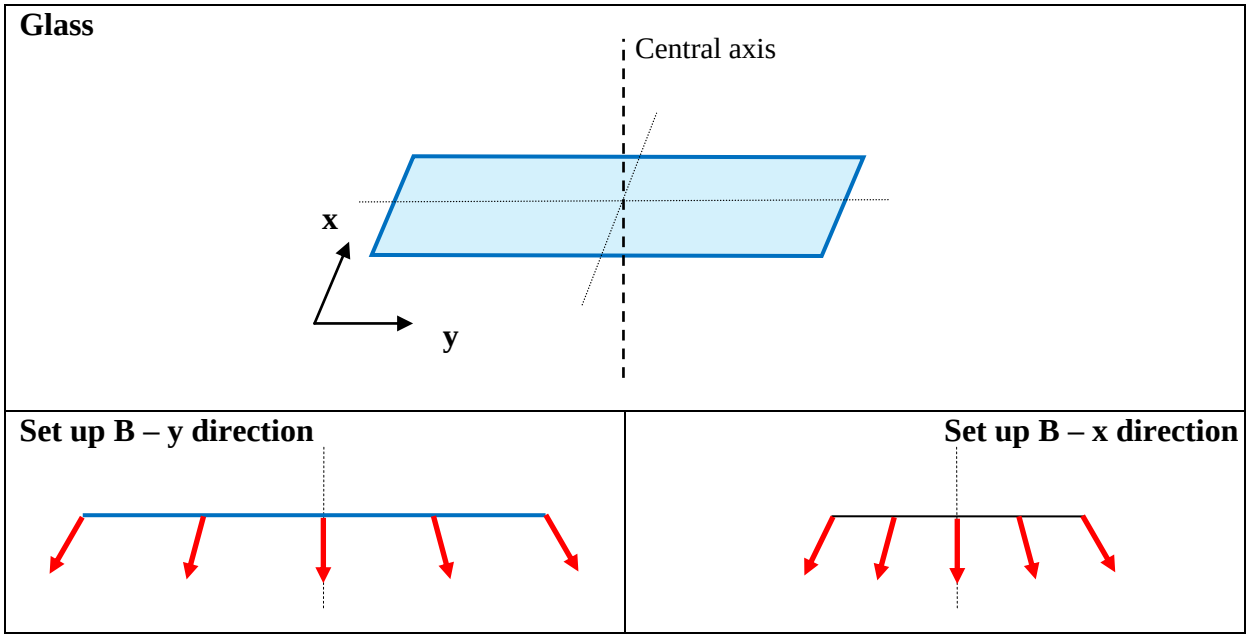

Figure 71 Lights set up

2.3.5. Numerical procedure

Both analyses have been set up following the same numerical settings:

- Analysis type
  - Steady state in double precision
- Advection Scheme
  - Specified blend factor 0.5
- Turbulence Numeric
  - First order
- Momentum, Turbulence and Mass Fraction Fluid False Timescale Control
  - Physical timescale: 0.001[s]
- Energy Fluid False Timescale Control
  - Physical timescale: 0.2[s]
- Convergence Criteria:
  - Residual target: 1.0E-12

This set up method is a good compromise between result quality and analysis speed, without interfering with its robustness.

2.3.6. Results

The fluid dynamic fields of the scenarios described in paragraph 2.3.4 are herein investigated. As shown in Figure 72, the overall flow field behavior is approximately the same for the two scenarios. The plant height is the only physical variable which locally affects the air circulation and generates perceptible differences in the flow patterns. Figure 73 shows the velocity vectors in proximity of the trays. Over the plant region velocity magnitudes are smaller and gives smoother recirculation for day 30 compared to day 9.

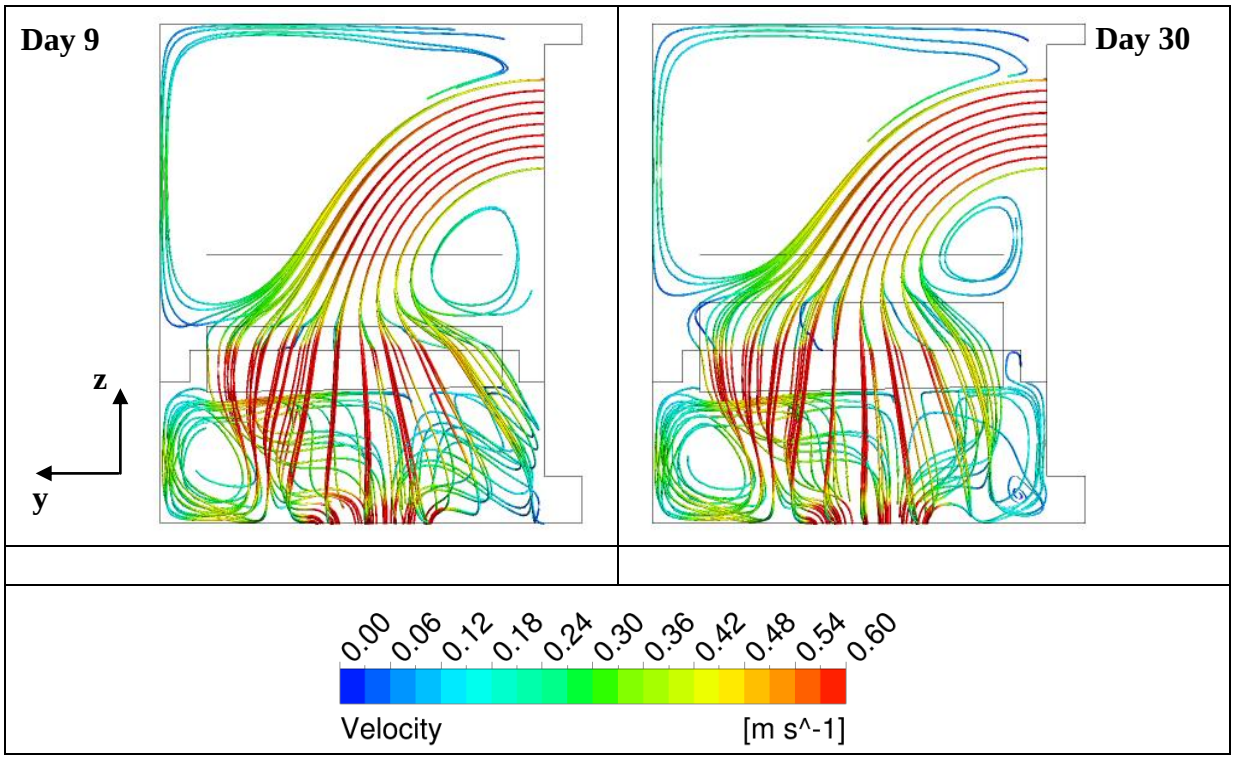

Figure 72 Streamlines colored by velocity

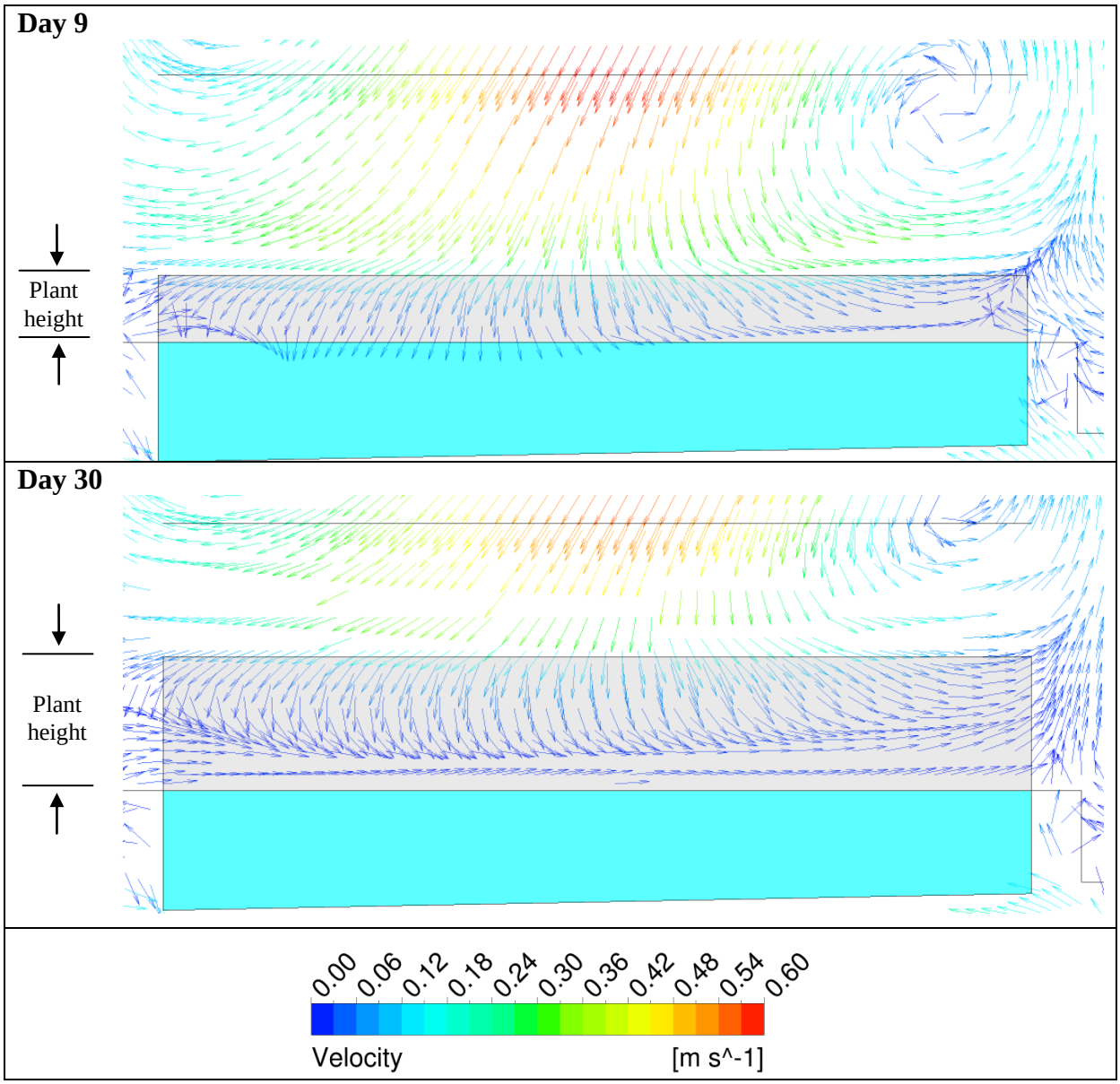

Figure 73 Velocity vectors in proximity of the trays

In the next figures the distribution of the environmental factors on a vertical transversal plane YZ placed in the midway between the sides of the sub model is shown. Results are provided for both the scenarios. The different distributions of the water vapor molar concentration at day 9 compared to day 30 prove the capability of the evapotranspiration model to interact with the environment. The water vapor production at day 30 (2.01E-05 [kg s^{-1}]) is about three times the water vapor production at day 9 (6.711E-06 [kg s^{-1}]).

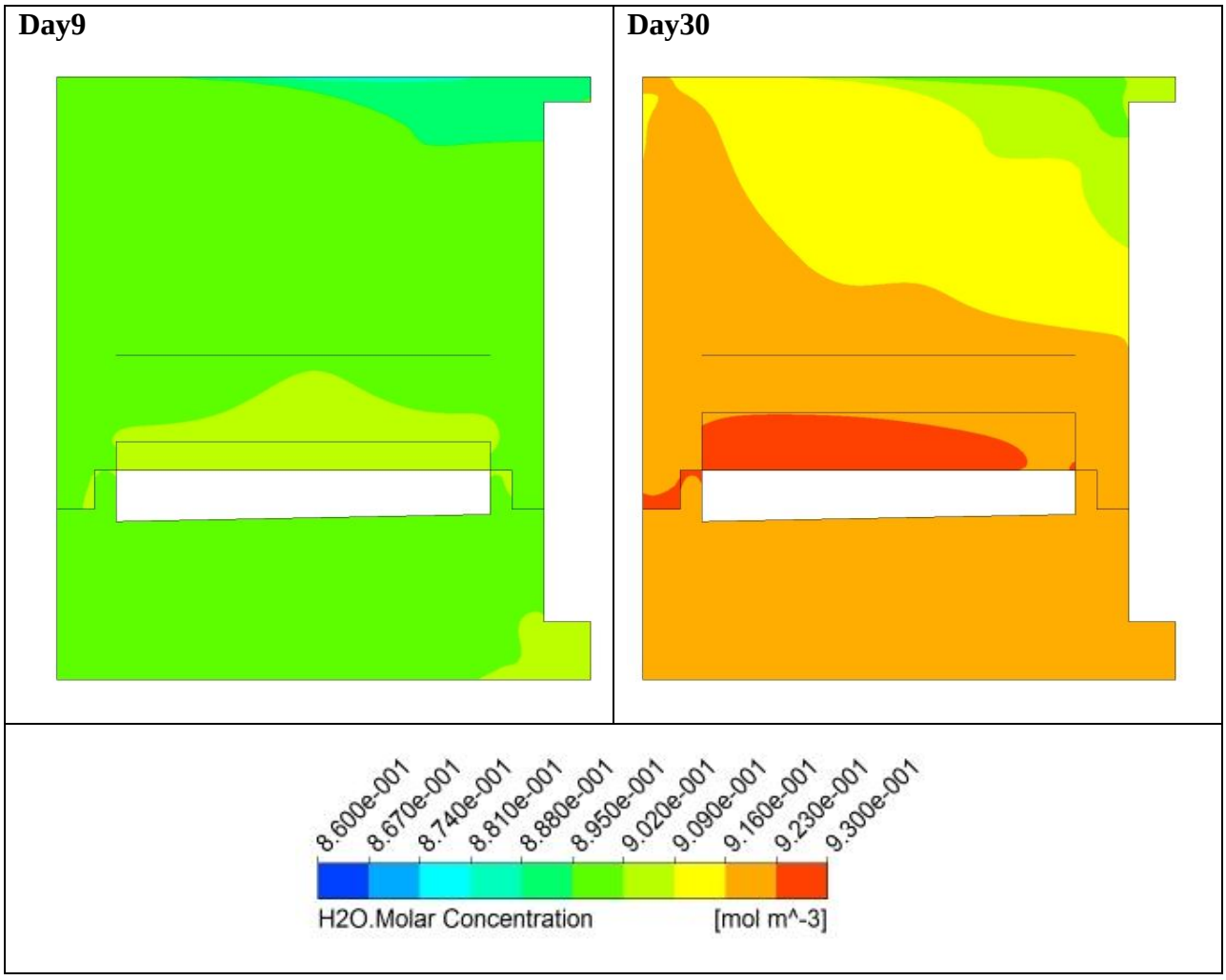

Figure 74 Water vapour distribution on plane YZ

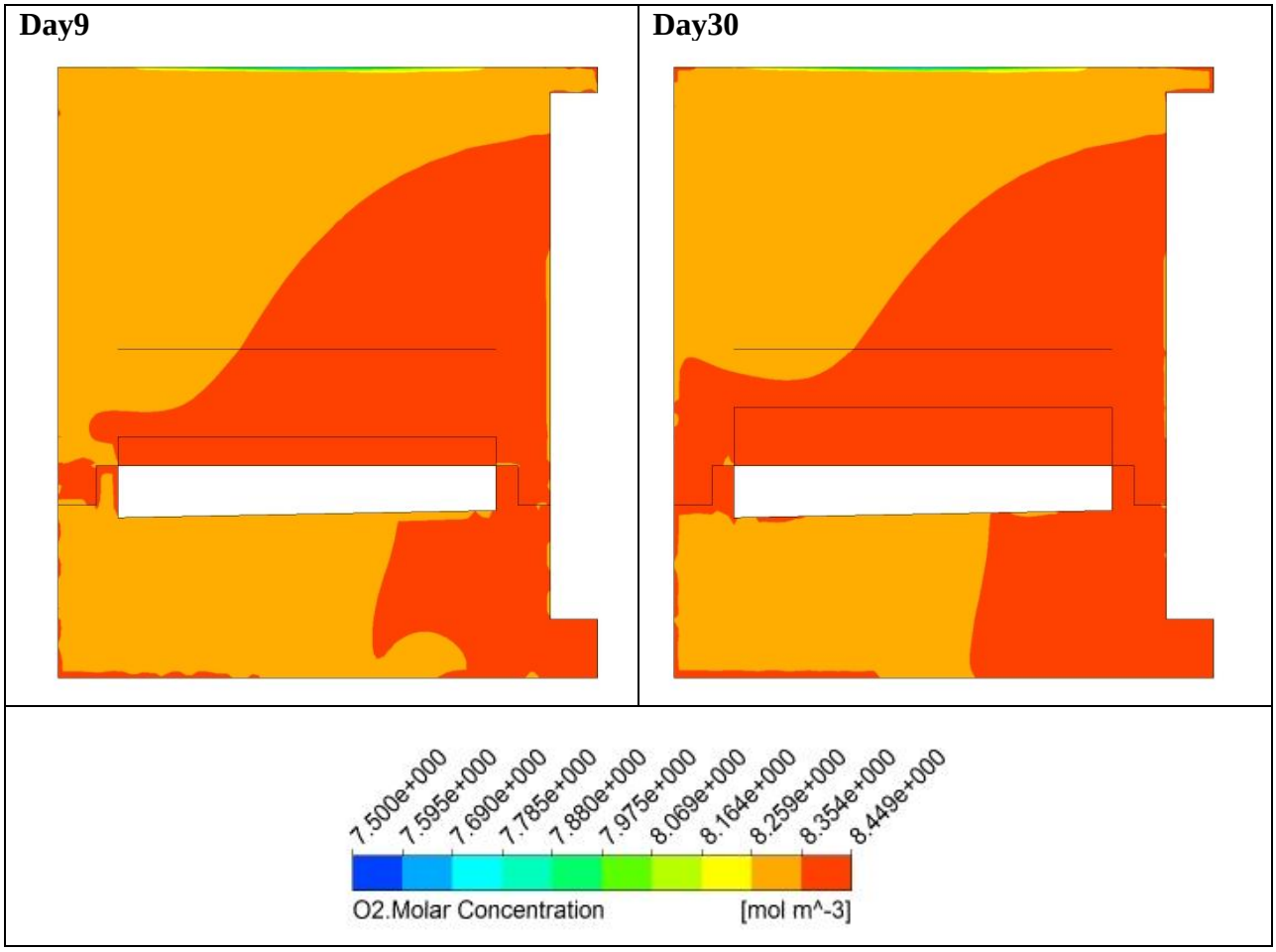

Figure 75 O2 distribution on plane YZ

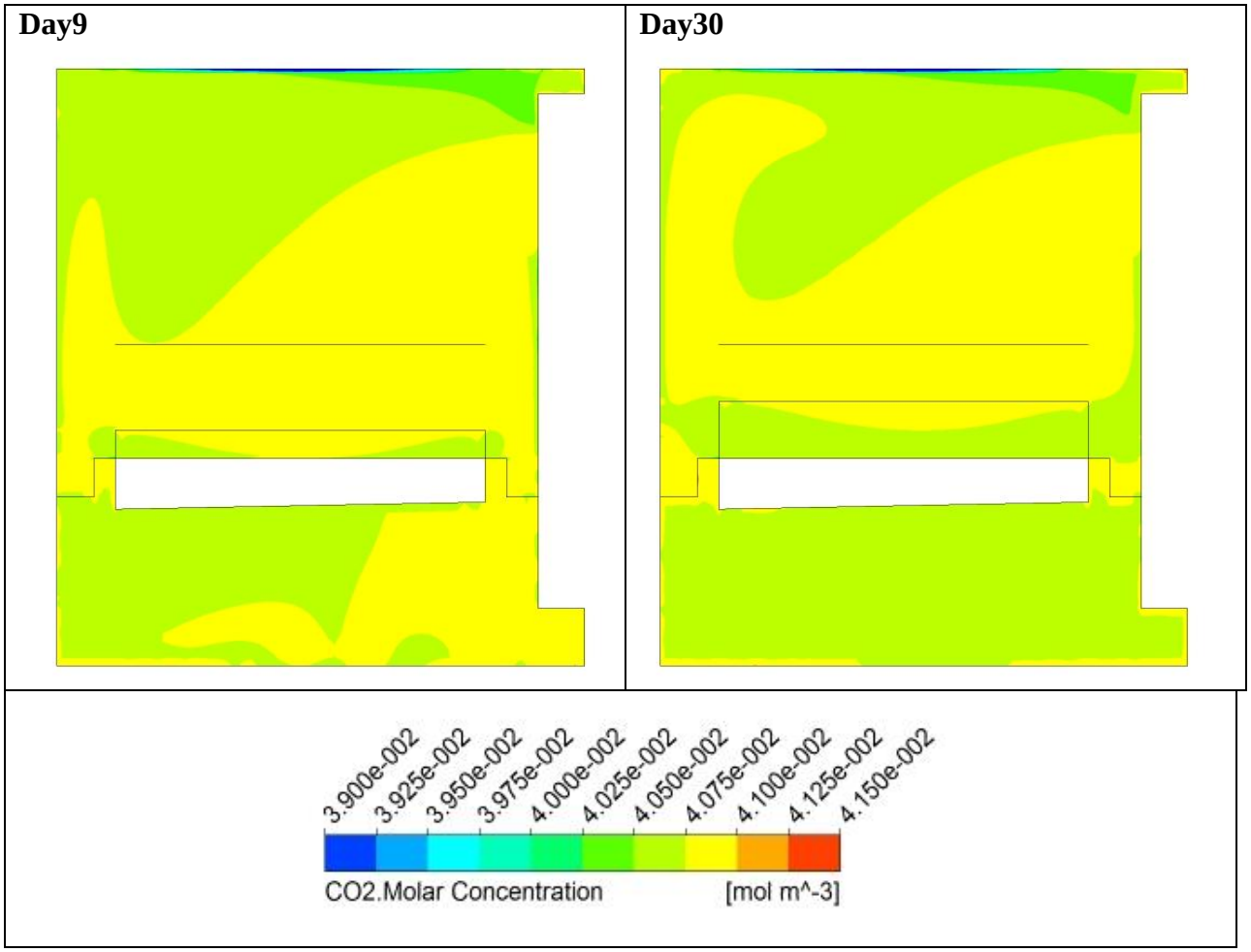

Figure 76 CO2 distribution on plane YZ

The radiative transport equation solution via the Monte Carlo model allows the characterization of the electromagnetic field in the computational domain. As shown in Figure 77 and Figure 78, the elliptical source of radiation applied at the glass leads to an uneven distribution of the incident radiation in the region above the plants and at the top of the trays (plant ground level). Indeed, lower incident radiation (1850[W m^{-2}]) are noticed at the front and at the back of the domain as well as in between the trays. Moreover, on equal terms of incoming radiation, greater plant height (day 30) results in a more attenuated radiation.

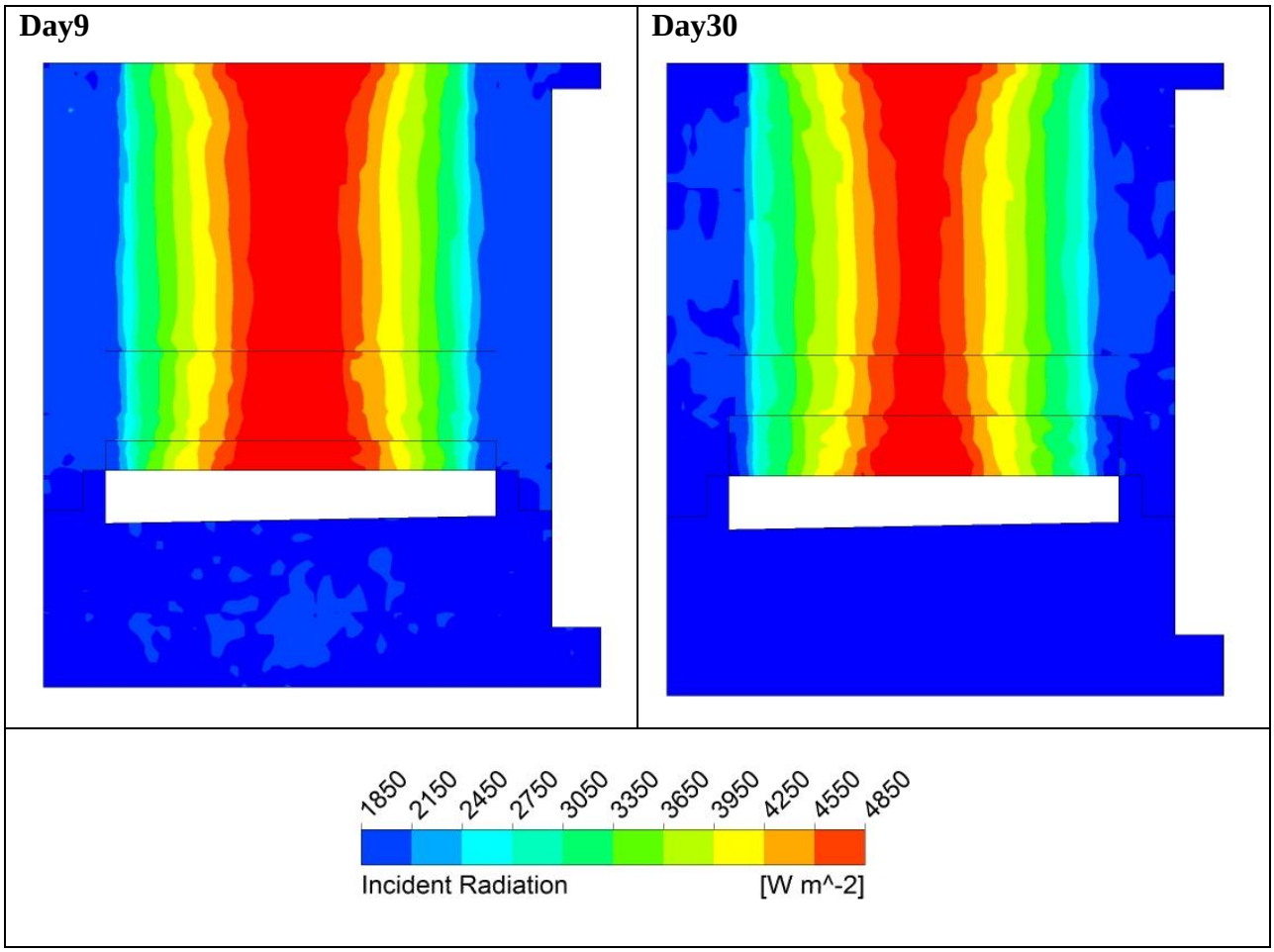

Figure 77 Incident radiation distribution on plane YZ

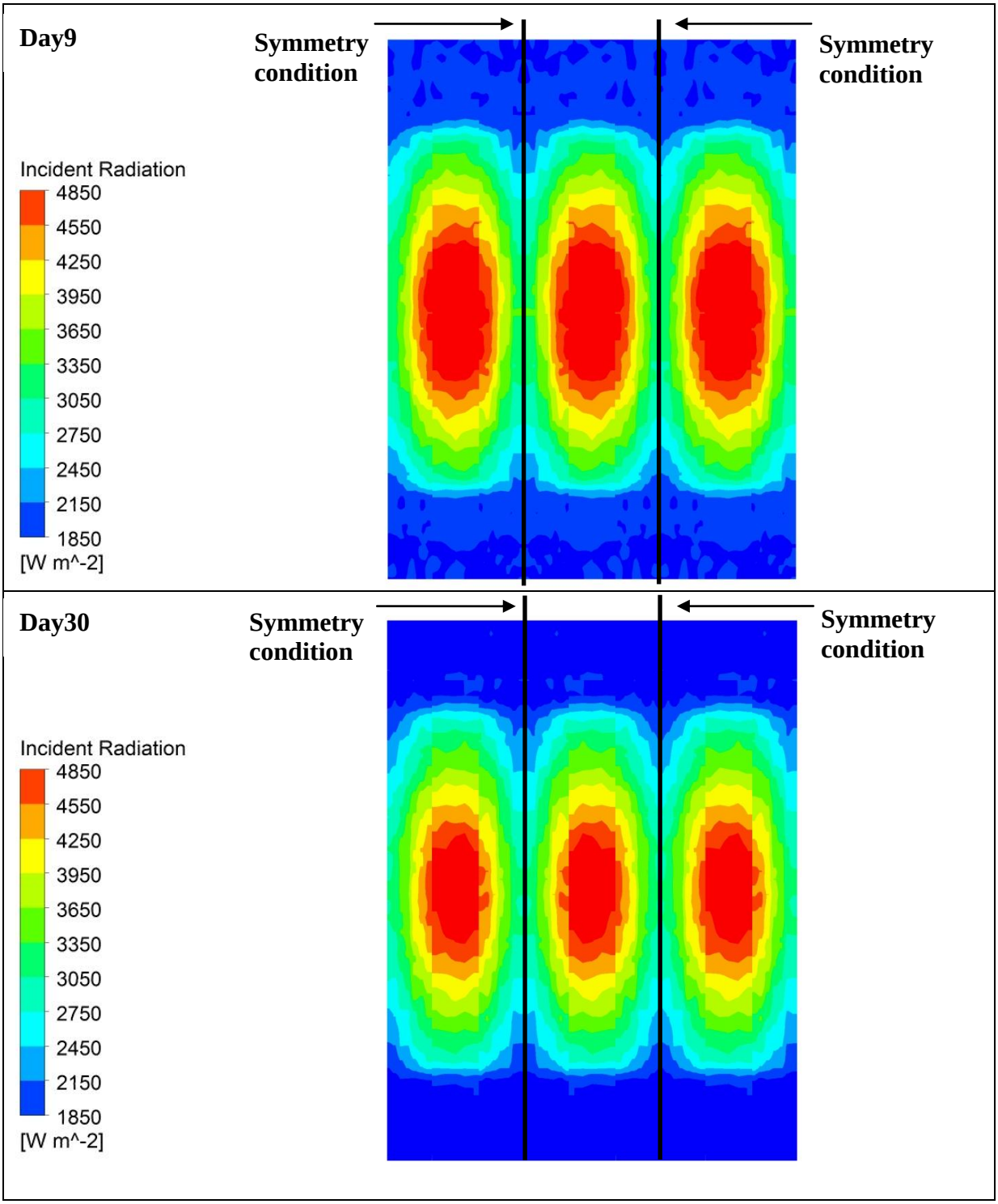

Figure 78 Distribution of the incident radiation at the top of the trays

The thermal effects induced by the radiation emitted from the glass and by the latent heat production glass are readily seen in the calculated temperature distribution.

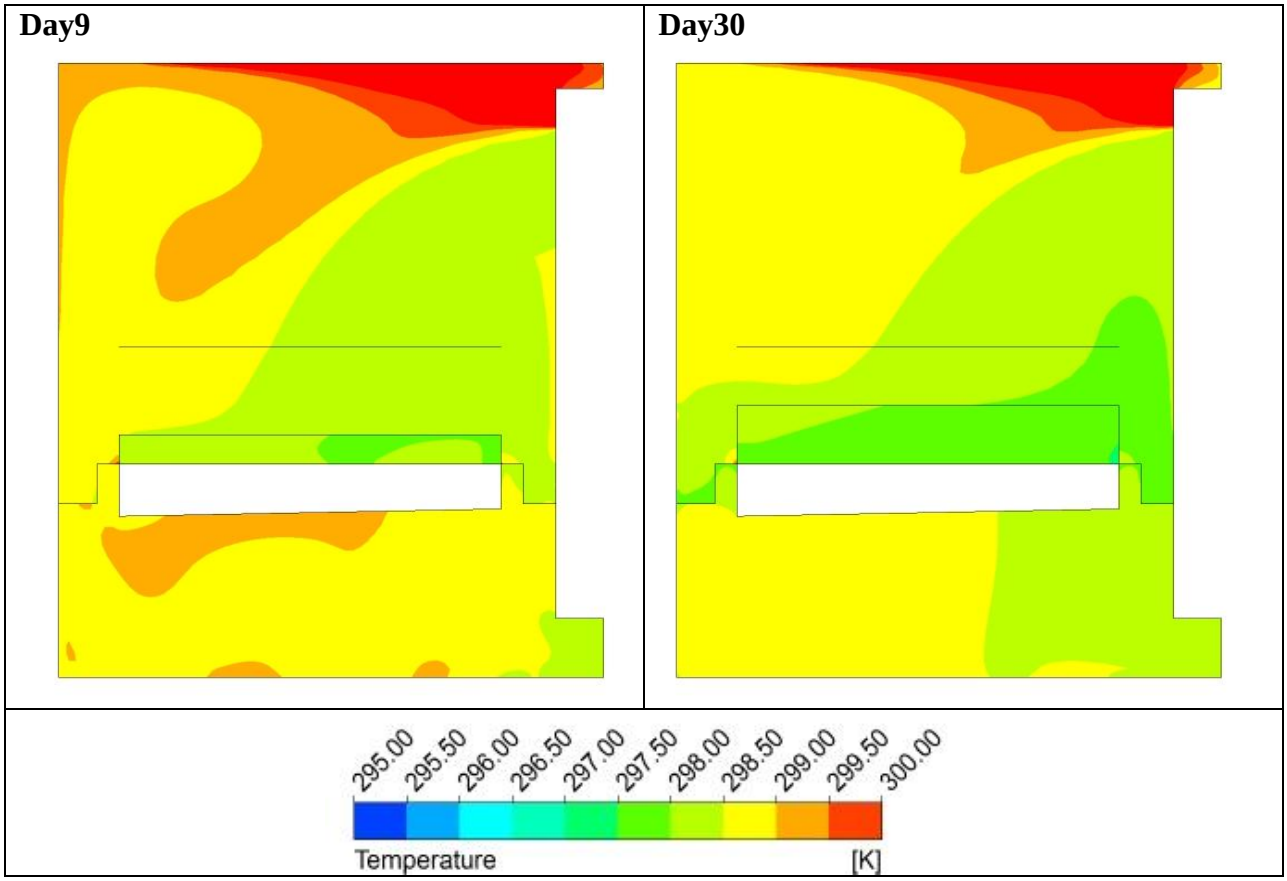

Figure 79 Temperature distribution on plane YZ

2.4. Conclusions

The CFD simulations of the chamber hardware with the inclusion of the plant evaporative load allowed the investigation of the environmental factors distribution inside the HPC.

The baseline model results show that:

- Gas exchange fluxes due to plant metabolism are very small compared the convective flux which is the dominant physical aspect inside the chamber.
- The air flow circulation patterns directly affect the distribution of the environmental factors. Indeed the unbalanced distribution of the air flow to the air grilles results in non-homogeneous maps of the environmental factors.
- The parameter heterogeneity is emphasized by the plant metabolism increment (day 30).

The Advanced canopy model results leads to the following conclusions:

- The considerations to be made on the environmental factors distribution are in agreement with the ones made for the baseline model.
- The evapotranspiration model response is sensitive to the plant size/age (height of the polygonal geometry which schematizes the plant), hence we have different sink/sources production as part of the mathematical model.

The Computational Fluid Dynamic (CFD) simulations provided important indications for the set up of the chamber control system. CFD results were used to determine the technical specifics of the probes and to identify the optimal position for the measurements.

3. Technical specifications

The full set of the dry model and wet model technical specification is provided on two DVDs. The DVDs contain:

- Geometry files (.tin)
- Computational grid files (.cfx5)
- CFD physic set up file (.cfx)
- Simulation results (.res .out)
- Excel data sheet concerning the experimental data provided (.xls)

4. References

ANSYS Inc. (2009). CFX Documentation Release 12.0 .

Dixon, M., & GRACE, J. (1983). Effect of Wind on the Transpiration of Young Trees. (53), 811-819.

European Space Agency. (2009, January). HPC1 Data Package.

Nicolau V. P, M. F. (2001). Determination of Radiative Properties of Commerical Glass. Florianópolis: PLEA.

Philips. (2007, May). *www.lighting.philips.com.* Tratto da horticulture site - GreenPower GreenVision 600/100W - OEM Design-in Guide.

University of Guelph CESRF. (2006). *TN 85.5 - Higher Plant Chamber Prototype for the MELiSSA Pilot Plant: Detailed Design and Verification.* Guelph.

University of Guelph CESRF. (2006). *TN 85.71 - Sub-Systems Technical Specifications.* Guelph